

NUMERICAL ANALYSIS OF IONIZED FIELDS ASSOCIATED WITH HVDC TRANSMISSION LINES INCLUDING EFFECT OF WIND

by

XIN LI

A Thesis

Submitted to the Faculty of Graduate Studies

in Partial Fulfillment of the Requirements

for the Degree of

DOCTOR OF PHILOSOPHY

Department of Electrical and Computer Engineering

The University of Manitoba, Winnipeg

Manitoba, Canada

©Xin Li, Dec.8, 1997



National Library
of Canada

Acquisitions and
Bibliographic Services

395 Wellington Street
Ottawa ON K1A 0N4
Canada

Bibliothèque nationale
du Canada

Acquisitions et
services bibliographiques

395, rue Wellington
Ottawa ON K1A 0N4
Canada

Your file Votre référence

Our file Notre référence

The author has granted a non-exclusive licence allowing the National Library of Canada to reproduce, loan, distribute or sell copies of this thesis in microform, paper or electronic formats.

L'auteur a accordé une licence non exclusive permettant à la Bibliothèque nationale du Canada de reproduire, prêter, distribuer ou vendre des copies de cette thèse sous la forme de microfiche/film, de reproduction sur papier ou sur format électronique.

The author retains ownership of the copyright in this thesis. Neither the thesis nor substantial extracts from it may be printed or otherwise reproduced without the author's permission.

L'auteur conserve la propriété du droit d'auteur qui protège cette thèse. Ni la thèse ni des extraits substantiels de celle-ci ne doivent être imprimés ou autrement reproduits sans son autorisation.

0-612-32001-4

Canada

THE UNIVERSITY OF MANITOBA
FACULTY OF GRADUATE STUDIES

COPYRIGHT PERMISSION PAGE

**NUMERICAL ANALYSIS OF IONIZED FIELDS ASSOCIATED WITH HVDC TRANSMISSION
LINES INCLUDING EFFECT OF WIND**

BY

XIN LI

**A Thesis/Practicum submitted to the Faculty of Graduate Studies of The University
of Manitoba in partial fulfillment of the requirements of the degree
of**

DOCTOR OF PHILOSOPHY

Xin Li ©1998

**Permission has been granted to the Library of The University of Manitoba to lend or sell
copies of this thesis/practicum, to the National Library of Canada to microfilm this thesis
and to lend or sell copies of the film, and to Dissertations Abstracts International to publish
an abstract of this thesis/practicum.**

**The author reserves other publication rights, and neither this thesis/practicum nor
extensive extracts from it may be printed or otherwise reproduced without the author's
written permission.**

CONTENTS

Abstract	i
Acknowledgments	ii
List of Figures	iii
Symbols and Notations	ix
Abbreviations	xiii
Chapter 1 Introduction	1
§1.1 Significance of Ionized Field Analysis	1
§1.2 Physical Background of DC Ionized Fields	2
§1.3 Mathematical Modelling of DC Ionized Fields	6
§1.4 A Review of Existing Solution Techniques	10
§1.5 Objective of the Thesis	16
Chapter 2 FEM Based Optimization Algorithm.	
Part I: FEM Formulation	17
§2.1 Unipolar Ionized Field Equations	17
§2.2 Finite Element Formulation of Poisson's Equation	19
§2.3 Finite Element Formulation of the Current Continuity Equation	22
§2.4 Equivalent Optimization Problem	24
§2.5 Evaluation of Matrices Involved in Equivalent Optimization Problem	26
§2.6 Scaling	28
§2.7 Calculation of Electric Field Strength on the Boundary	31
§2.8 Summary	31

Chapter 3 FEM Based Optimization Algorithm.	
Part II: Solution Techniques	33
§3.1 Introduction to Iterative Methods.....	33
§3.2 The Modified Gaussian Algorithm.....	34
§3.3 Consideration of Special Structure of Objective Function as Applied to Ionized Fields.....	36
§3.4 Schemes for Application of Boundary Conditions at Conductor Surface.....	38
§3.5 Numerical Tests on a Coaxial Cylindrical Model	40
§3.6 Numerical Tests on a Line-Plane Model in Still Air	46
§3.7 Numerical Tests on a Line-Plane Model under Wind Conditions	50
§3.8 Summary	52
Chapter 4 Upwind FVM Based Relaxation Algorithm.....	54
§4.1 Equation and Boundary Conditions	54
§4.2 Iterative Algorithm.....	55
§4.3 FEM for Poisson's Equation	59
§4.4 FEM for the Current Continuity Equation	60
§4.5 Numerical Tests on the Coaxial Cylindrical Model.....	67
§4.6 Numerical Tests on the Line-Plane Model.....	69
§4.7 Summary	79
Chapter 5 Analysis of Bipolar Ionized Fields	82
§5.1 Equations and Boundary Conditions	82
§5.2 Iterative Algorithm.....	84
§5.3 Solution of the Current Continuity Equation	87

§5.4 Numerical Examples	91
§5.5 A Simplified Model for Bipolar Ionized Field.....	94
§5.6 Summary	96
Chapter 6 Investigation of Unipolar Bundled DC Line Ionized Fields.....	98
§6.1 Introduction	98
§6.2 Effect of Conductor Bundling on Ionized Fields	99
§6.3 Comparison between 2- and 4-subconductor Bundle Unipolar Line.....	104
§6.4 Equivalent Single Conductor Model	107
§6.5 Summary	110
Chapter 7 Conclusions.....	112
References	116

ABSTRACT

Corona discharges on the conductor surface of a HVDC transmission line generate ion flow in the interelectrode space, and therefore cause power losses as well as environmental concerns. To evaluate these effects, one has to solve the ion flow field (or ionized field). However, the solution of this problem is very difficult due to its nonlinearity and the effect of wind. Although this problem has been tackled by a number of researchers over the past several decades, a review of the existing literature indicates that problems associated with strong wind or bundled lines are still not solved satisfactorily.

This thesis presents two new numerical algorithms, the FEM based optimization algorithm and the upwind FVM (node-centered FVM and triangular FVM) based relaxation algorithm, for solving unipolar ionized fields including the effect of wind. The validity and efficiency of the presented algorithms is favorably demonstrated on a coaxial cylindrical configuration and on a unipolar line model in the presence of wind. Stable and fast convergence is observed for the former algorithm under moderate wind conditions, while excellent iterative behavior is exhibited by the latter with wind velocities in the range from 0 to 45 m/s or even higher.

The FVM based relaxation algorithm is also extended to analyze the bipolar ionized field. A simplified model is suggested so that the bipolar ionized field in the absence of wind may be treated as the combination of two unipolar ionized fields for computing the field quantities at ground level.

The ionized field due to bundled unipolar DC lines is investigated in detail by using the FVM based relaxation algorithm. The geometries considered are typical of practical DC lines and the effect of wind is included. The validity of the equivalent single conductor approach is verified.

ACKNOWLEDGEMENTS

I would like to thank my advisors, Dr. M. R. Raghuveer and Dr. I. R. Cric, for their valuable advice, suggestion and encouragement throughout the Ph.D research and for their time spent on reviewing the manuscripts of the thesis and its related publications.

My sincere thanks go to Dr. Ming Yu for kindly providing his Ph.D thesis and some other technical material, which markedly assisted in my starting the Ph.D research. Also, suggestions from him are gratefully appreciated.

Thanks also go to Dr. M. M. Rashwan and Dr. S. Ormiston, the members of the examining committee of my Ph.D. program, for their suggestions and time.

It is worth remembering that Mr. J. Kendall, a kind person in charge of the High Voltage Lab., was always available for help whenever I needed it.

I would like to gratefully acknowledge the financial support from Manitoba Hydro, and the Natural Sciences and Engineering Research Council of Canada. My sincere appreciation also goes to the donors of the following three awards: the University of Manitoba Fellowship, the Gordon P. Osler Graduate Scholarship and the Donald M. Stephens Memorial Fellowship.

Finally, special thanks are due to my wife, Qi, and daughter, Jian, for their understanding and support.

LIST OF FIGURES

- Figure 1.1.** DC transmission line. (p. 9)
- Figure 2.1.** Three-noded element. (p. 26)
- Figure 3.1.** The subsets $I_{(l)}^N$ and $\tilde{I}_{(l)}^N$. (p. 37)
- Figure 3.2.** Schematic demonstration of Scheme III. (p. 39)
- Figure 3.3.** Coaxial cylindrical model. (p. 40)
- Figure 3.4.** FE mesh for the coaxial cylindrical model. (p. 41)
- Figure 3.5.** Iterative behaviour of the algorithm for different initial values — Scheme II;
 $n_p = 792$. (p. 42)
- Figure 3.6.** Normalized solutions for u and q along a radial direction — Scheme II;
 $n_p = 792$. (p. 43)
- Figure 3.7.** Percent error in u for different n_p — Scheme I. (p. 44)
- Figure 3.8.** Percent error in q for different n_p — Scheme I. (p. 44)
- Figure 3.9.** Percent error in u for different n_p — Scheme II. (p. 44)
- Figure 3.10.** Percent error in q for different n_p — Scheme II. (p. 45)
- Figure 3.11.** Percent error in the electric field strength E at the grounded conductor surface versus n_p — Schemes I and II. (p. 45)
- Figure 3.12.** Iterative behaviour of the algorithm for different n_p — Scheme II; $\tau = 0.4$.
(p. 45)
- Figure 3.13.** CPU time versus the number of nodes. (p. 46)
- Figure 3.14.** Line-plane model. (p. 46)
- Figure 3.15.** FE mesh for the line-plane model; $n_p = 1291$. (p. 47)
- Figure 3.16.** Iterative behaviour of Schemes I and II; $V_0 = 200$ kV; $R_{eq} = 4$ m. (p. 48)

Figure 3.17. Ground profiles of electric field strength for different voltage levels. (p. 49)

Figure 3.18. Ground profiles of space charge density for different voltage levels. (p. 49)

Figure 3.19. Comparison between the calculated ground profiles of electric field strength and the measured values [23] in still air ($w < 1$ m/s). (p. 49)

Figure 3.20. Ground profiles of electric field strength for different wind velocities. (p. 51)

Figure 3.21. Ground profiles of space charge density for different wind velocities. (p. 51)

Figure 3.22. Comparison between the calculated ground level profile of electric field strength and the measured values [23] under wind condition ($w = 8$ m/s). (p. 52)

Figure 4.1. Construction of the control volume around an inner node i or a boundary node i . (p. 61)

Figure 4.2. Side ∂C_{ij} associated with the centres of gravity of two triangular elements. (p. 62)

Figure 4.3. Side ∂C_{ij} shared by two cells. (p. 65)

Figure 4.4. Space charge density ρ_i of the cell C_i influenced by cells on its upwind side.
(a) ρ_i influenced by one cell; (b) ρ_i influenced by two cells. (p. 65)

Figure 4.5. Behavior of the iterative algorithm. (p. 67)

Figure 4.6. Calculated distributions of u and ρ along the radial direction. (p. 68)

Figure 4.7. Percent error in u obtained by using different algorithms. (p. 68)

Figure 4.8. Percent error in ρ obtained by using different algorithms. (p. 69)

Figure 4.9. Effect of relaxation on the iterative behaviour; $\gamma_{upw} = 1$, $w = 10$ m/s,
 $r_0 = 0.0025$ m, $H = 2$ m, $V_0/V_c = 2$. (p. 70)

Figure 4.10. Effect of the relaxation factor θ on the number of iterations required for convergence for different wind velocities; $\gamma_{upw} = 1$, $r_0 = 0.0025$ m, $H = 2$

$m, V_0/V_c = 2.$ (p. 71)

Figure 4.11. Effect of the relaxation factor θ on the number of iterations required for convergence for different values of $V_0/V_c; \gamma_{upw} = 1, w = 0 \text{ m/s}, r_0 = 0.0025 \text{ m}, H = 2 \text{ m.}$ (p. 72)

Figure 4.12. Effect of the relaxation factor θ on the number of iterations required for convergence for different values of $H/r_0; \gamma_{upw} = 1, H = 2 \text{ m}, w = 0 \text{ m/s}, V_0/V_c = 2.$ (p. 72)

Figure 4.13. Effect of the relaxation factor θ on the number of iterations required for convergence for different values of $H; \gamma_{upw} = 1, H/r_0 = 800, w = 0 \text{ m/s}, V_0/V_c = 2, n_p = 1291.$ (p. 73)

Figure 4.14. Effect of using the upwind algorithm on the iterative behaviour; $w = 9 \text{ m/s}, \theta = 0.5, r_0 = 0.0025 \text{ m}, H = 2 \text{ m}, V_0/V_c = 2.$ (p. 73)

Figure 4.15. Effect of wind velocity on the $n_{iter}—\theta$ curve when $\gamma_{upw} = 0; r_0 = 0.0025 \text{ m}, H = 2 \text{ m}, V_0/V_c = 2.$ (p. 74)

Figure 4.16. Effect of the upwind parameter γ_{upw} on the number of iterations required for convergence for different wind velocities; $r_0 = 0.0025 \text{ m}, H = 2 \text{ m}, V_0/V_c = 2.$ (p. 74)

Figure 4.17. Calculated ground profiles of electric field strength in the absence of wind considering the effect of $\gamma_{upw}; r_0 = 0.0025 \text{ m}, H = 2 \text{ m}, V_0/V_c = 2.$ (p. 75)

Figure 4.18. Calculated ground profiles of space charge density in the absence of wind considering the effect of γ_{upw} ; $r_0 = 0.0025$ m, $H = 2$ m, $V_0/V_c = 2$. (p. 75)

Figure 4.19. Comparison of the ground profiles of electric field strength obtained by different algorithms in the absence of wind; $r_0 = 0.0025$ m, $H = 2$ m. (p. 76)

Figure 4.20. Comparison of the ground profiles of space charge density obtained by different algorithms in the absence of wind; $r_0 = 0.0025$ m, $H = 2$ m. (p. 76)

Figure 4.21. Comparison of the ground profiles of electric field strength obtained by the present algorithm with results in [46] and measured values in [23] ($w < 1$ m/s); $r_0 = 0.0025$ m, $H = 2$ m. (p. 77)

Figure 4.22. Comparison of the ground profiles of electric field strength obtained by different algorithms for a wind velocity $w = 8$ m/s; $r_0 = 0.0025$ m, $H = 2$ m, $V_0 = 300$ kV. (p. 78)

Figure 4.23. Comparison of the ground profiles of space charge density obtained by different algorithms for a wind velocity $w = 8$ m/s; $r_0 = 0.0025$ m, $H = 2$ m, $V_0 = 300$ kV. (p. 78)

Figure 4.24. Ground profiles of electric field strength generated by the FVM based relaxation algorithm under strong wind conditions; $r_0 = 0.0025$ m, $H = 2$ m, $V_0 = 200$ kV. (p. 79)

Figure 4.25. Ground profiles of space charge density generated by the FVM based relaxation algorithm under strong wind conditions; $r_0 = 0.0025$ m, $H = 2$ m, $V_0 = 200$ kV. (p. 79)

Figure 5.1. Bipolar DC line model. (p. 91)

Figure 5.2. FE mesh for the bipolar DC line model. (p. 92)

Figure 5.3. Calculated ground profiles of electric field strength. (p. 93)

Figure 5.4. Calculate ground profiles of space charge density, ($\rho^+ + \rho^-$). (p. 93)

Figure 5.5. Effect of recombination on the ground profile of electric field strength;

$$V_0 = 200 \text{ kV. (p. 94)}$$

Figure 5.6. Effect of recombination on the ground profile of space charge density;

$$V_0 = 200 \text{ kV. (p. 94)}$$

Figure 5.7. Ground profiles of electric field strength obtained by use of the simplified model at different voltage levels in the absence of wind. (p. 96)

Figure 5.8. Ground profiles of space charge density, ($\rho^+ + \rho^-$), obtained by use of the simplified model at different voltage levels in the absence of wind. (p. 96)

Figure 6.1. Two-bundle unipolar DC line. (p. 99)

Figure 6.2. Finite element mesh for the 2-bundle line model with $r_0 = 0.01905 \text{ m}$,

$$H = 15.24 \text{ m}, H/s = 32, n_p = 1769, n_e = 3412. \text{ (p. 100)}$$

Figure 6.3. Local finite element mesh near the bundled conductor. (a) Local mesh near the 2-bundle. (b) Local mesh near each subconductor. (p. 100)

Figure 6.4. Ground profiles of electric field strength of the 2-bundle line for different ratio H/s ; $H/r_0 = 1600 \text{ m}$, $H = 15.24 \text{ m}$, $V_0 = 314 \text{ kV. (p. 102)}$

Figure 6.5. Ground profiles of space charge density of the 2-bundle line for different ratio H/s ; $H/r_0 = 1600 \text{ m}$, $H = 15.24 \text{ m}$, $V_0 = 314 \text{ kV. (p. 102)}$

Figure 6.6. Ground profiles of electric field strength of the 2-bundle line for different ratio H/s ; $H/r_0 = 800 \text{ m}$, $H = 15.24 \text{ m}$, $V_0 = 538 \text{ kV. (p. 102)}$

Figure 6.7. Ground profiles of space charge density of the 2-bundle line for different ratio H/s ; $H/r_0 = 800 \text{ m}$, $H = 15.24 \text{ m}$, $V_0 = 538 \text{ kV. (p. 103)}$

Figure 6.8. Ground profiles of electric field strength of the 2-bundle line for different ratio H/s ; $H/r_0 = 400$ m, $H = 15.24$ m, $V_0 = 926$ kV. (p. 103)

Figure 6.9. Ground profiles of space charge density of the 2-bundle line for different ratio H/s ; $H/r_0 = 400$ m, $H = 15.24$ m, $V_0 = 926$ kV. (p. 103)

Figure 6.10. Effect of the ratio s/H on the corona current; $H = 15.24$ m. (p. 104)

Figure 6.11. Four-subconductor bundled line. (p. 105)

Figure 6.12. Local mesh near the bundled conductor. (p. 105)

Figure 6.13. Ground profiles of electric field strength of the 2- and 4-bundle lines at different wind velocities. (p. 106)

Figure 6.14. Ground profiles of space charge density of the 2- and 4-bundle lines at different wind velocities. (p. 106)

Figure 6.15. Ground profiles of electric field strength of the single conductor line equivalent to the 2-bundle line. (p. 108)

Figure 6.16. Ground profiles of space charge density of the single conductor line equivalent to the 2-bundle line. (p. 109)

Figure 6.17. Ground profiles of electric field strength of the single conductor line equivalent to the 4-bundle line. (p. 109)

Figure 6.18. Ground profiles of space charge density of the single conductor line equivalent to the 4-bundle line. (p. 109)

Figure 6.19. Corona currents of the equivalent single conductor lines as influenced by wind. (p. 110)

SYMBOLS AND NOTATIONS

- + superscript indicating a quantity corresponding to the positive polarity or the positive conductor.
- superscript indicating a quantity corresponding to the negative polarity or the negative conductor.
- \wedge symbol indicating an interpolation function.
- T superscript indicating the transpose of a matrix or a vector.
- $\{\bullet\}$ indicates a vector of nodal values of a scalar quantity.
- $[\bullet]$ indicates a matrix.
- $\{0\}$ zero vector.
- $[I]$ unit matrix.
- max indicates the maximum value of a quantity.
- min indicates the minimum value of a quantity.
- E electric field intensity.
- j corona current density.
- w wind velocity.
- v drift velocity of space charge density.
- I_c corona current per unit length of the DC line.
- k^+ mobility of the positive space charge (1.4×10^{-4} m²/V.s).
- k^- mobility of the negative space charge (1.8×10^{-4} m²/V.s).
- ϵ_0 permittivity of free space (8.854×10^{-12} F/m).

- Φ electric potential of the charge free field.
- φ electric potential due to space charge only.
- u total electric potential.
- ρ space charge density.
- R_{ion} coefficient of recombination ($2.2 \times 10^{-12} \text{ m}^3/\text{s}$).
- e absolute value of an electron charge ($1.6 \times 10^{-19} \text{ C}$), or any element in a finite element mesh.
- D coefficient of ion diffusion.
- q $q = \rho/\epsilon_0$.
- ξ velocity potential representing the wind distribution.
- V_0 operating voltage of a transmission line.
- E_c corona onset field strength, defined by Peek's law.
- V_c corona onset voltage.
- ρ_c space charge density at the conductor surface.
- q_c value of q at the conductor surface.
- H conductor height.
- r_0 radius of the energized conductor.
- s spacing of two poles of a bipolar DC line or the spacing of subconductors of a unipolar bundled unipolar line.
- Ω the solution domain, not including the boundary.
- Γ boundary of the solution domain.

Ω	solution domain including the boundary, i.e. $\bar{\Omega} = \Omega \cup \Gamma$.
Γ_c	boundary corresponding to the conductor surface.
Γ_g	boundary corresponding to the grounded plane.
Γ_a	artificial boundary.
Γ_{up}	a portion of the boundary Γ_a or $\Gamma_a \cup \Gamma_g$, through which the space charge flowing into the solution domain is neglected.
n_p	number of nodes in a finite element mesh.
n_e	number of elements in a finite element mesh.
$I(\bullet)$	set of nodal points contained in (\bullet) .
Ω_e	subdomain covered by the e th element.
$\hat{\Omega}_l$	subdomain consisting of the elements associated with the node l .
$I_{(i)}^N$	set of nodal points associated with the node i .
$\tilde{I}_{(i)}^N$	set of nodal points associated with the node i , including the node i itself.
β_l	number of nodal points on $\hat{\Omega}_l$.
$\bar{\beta}$	average number of β_l .
C_i	i th control volume or cell.
∂C_i	boundary of C_i .
∂C_{ij}	common side of C_i and C_j .
n_{cell}	number of control volumes.

$I_{(i)}^C$ set of cells associated with the cell C_i .

$I_{(i)}^{C_{upw}}$ set of cells associated with the cell C_i on its upwind side.

γ_{upw} upwind parameter in the FVM.

θ relaxation factor in the FVM based relaxation algorithm.

n_{iter} number of iterations required for convergence.

ABBREVIATIONS

AC	Alternating Current.
BEM	Boundary Element Method.
BC	Boundary Condition.
CSM	Charge Simulation Method.
DC	Direct Current.
FE	Finite Element.
FEM	Finite Element Method.
FV	Finite Volume.
FVM	Finite Volume Method
HV	High Voltage.
PDE	Partial Differential Equation.

CHAPTER 1

INTRODUCTION

This chapter introduces the significance, physical background and mathematical modelling of the DC ionized field problem. Existing solution techniques are reviewed. Finally, the objective of the thesis is delineated.

§1.1 Significance of Ionized Field Analysis

High-voltage (HV) direct current (DC) transmission offers advantages over HV alternating current (AC) transmission for long distant bulk power transfer. In recent years, progress in DC technology and increasing demand for electrical energy have stimulated fast development of HVDC transmission lines. DC transmission lines with an operating voltage of 500 kV or above have been put into service in various parts of the world. At the same time, however, some associated problems have arisen, one of which is the environmental problem under a HVDC transmission line.

Since DC transmission lines are usually operated above their corona onset voltage, ions or space charges are generated close to the energized conductor. Under the action of the electric field, the space charge migrates in a certain manner and fills the whole interelectrode space, thus causing some environmental effects in addition to power losses. For example, the resulting corona currents charge the objects at ground such as a human body. Experimental investigations [38] have shown that the space charge concentration can be

detected half a mile away from a HVDC line. Also, the appearance of the space charge breaks the natural balance between the positive and negative ions in air, and as a result some possible biological effects may be induced. All this necessitates the quantitative analysis of the ionized field, i.e. the electric field in the presence of corona. In the case of HVAC transmission lines, due to the periodic reversal of the polarity of the voltage, the space charge is confined within a certain region near the energized conductor.

Research on the DC ionized field problem also has practical importance in other engineering areas such as the design of electrostatic precipitators.

The analysis of ionized fields started with Townsend's work [8] at the beginning of this century. Early research was concentrated on experiments and analytical analyses. Numerical techniques became popular with the introduction of modern computers in the 1960's. Since then many efforts have been made to develop a practical method for solving the ionized field problem.

§1.2 Physical Background of DC Ionized Fields

1.2.1 Corona and Ionized Fields

As mentioned above, the ionized field is related to the corona phenomenon. According to The *IEEE Standard Dictionary of Electrical and Electric Terms*, corona is “a luminous discharge due to ionization of the air surrounding a conductor caused by a voltage gradient exceeding a certain critical value”. This critical voltage gradient (or field strength) and the corresponding voltage are referred to as the corona onset gradient (or field strength) and the corona onset voltage, respectively. Extensive research on corona began some 60 years ago. A detailed review of corona discharges was given by Leob [1] in his book. Experi-

mental investigations of coronas associated with HV transmission lines were reported in [12,13].

Corona discharge is possible only in the case of non-uniform electric fields. In a HV transmission system, the conductor's dimension is very small compared to its height, and the electric field is highly enhanced near the conductor surface. From Townsend's ionization theory, electrons present near the conductor may gain sufficient kinetic energy from the electric field and ionize the air molecules by collision. This gives rise to avalanches which include a large number of electrons and positive ions. Corona discharge starts when the avalanches become self-sustained. Since the electric field strength decreases drastically with distance from the conductor surface, the discharge is confined to a thin layer around the conductor which is commonly known as the ionization layer.

Coronas are classified as positive or negative coronas depending upon the polarity of the stressed conductor. Positive corona in a line-plane configuration (positive unipolar configuration) develops in the form of burst and streamer pulses which occur randomly. As the applied voltage is raised, the pulses become more frequent, and finally the discharge becomes a pulseless glow close to the conductor. The electrons generated in the ionization layer are attracted to the conductor; the positive ions migrate towards the grounded plane. When the conductor has a negative polarity (negative unipolar configuration), regularly spaced discharge pulses are generated, which are named Trichel pulses [1] since they were first discovered by Trichel. The pulse frequency increases with the applied voltage. Eventually, a steady glow discharge is formed at a much higher voltage level. The electrons from the ionization layer rapidly enter the surrounding air and form negative ions by attachment to neutral air molecules and particles. The negative ions drift towards the

grounded plane, while the positive ions created by ionization move towards the conductor where they are neutralized.

It is clear that when corona occurs in a unipolar DC transmission line, the ionization layer around the conductor serves as the source of space charge which has the same polarity as the conductor in corona. The generated space charge migrates towards ground. Thus the whole interelectrode space is filled with the space charge. The drift velocity of the positive (or negative) space charge due to the electric field strength is kE (or $-kE$), where k is the ionic mobility and E the electric field strength. The corona current density due to the electric field is $j = k|\rho|E$, where ρ is the space charge density.

In the case of a bipolar DC transmission line, there are two conductors with opposite polarity, positive and negative, aligned in parallel above ground. Positive and negative space charges are generated near the two conductors, respectively. The space charges produced by each conductor drift towards the other conductor and ground. Since the space charges of both polarities mix in the interelectrode space, recombination occurs.

The electric field in the presence of corona is called ionized field or ion flow field. Depending on whether space charges of only one polarity or both polarities exist, the ionized field is referred to as unipolar or bipolar ionized field. Obviously, the quantities which characterize the ionized field include the electric field strength and the space charge density.

1.2.2 Factors Affecting Ionized Fields

The charge-free electric field of a HVDC transmission line is determined by its operating voltage and geometry. However, the ionized field is affected not only by these factors, but

also by the prevailing atmospheric and weather conditions [7]. Fog, rain and snow, for example, all tend to increase the corona activity on the conductor and hence increase the corona current density near the conductor. It is difficult to study the ionized field by taking into consideration these factors in detail, since they do not remain constant but change in random fashion. Fortunately, as confirmed by observation [7], foul weather conditions, like heavy rain, do not present a big problem for HVDC transmission lines in terms of corona losses.

Wind has a more significant effect on the movement of the space charge and hence the ionized field distribution. As mentioned above, the space charge is generated near the conductor surface in corona where the electric field strength is above the corona onset gradient. In a typical HVDC transmission line, the corona onset gradient is about 21 kV/cm , the positive ionic mobility is of the order of $1.4 \text{ cm}^2/\text{V.s}$ and the initial ion drift velocity is as high as 290 m/s . This velocity is higher than the normal wind velocity by about two orders of magnitude and, therefore, the effect of wind on the ionization layer is negligible. However, since the electric field strength attenuates rapidly with distance from the conductor, the space charge drift velocity is of the order of 3 m/s near ground or at a location far from the conductor. This velocity is comparable with typical wind velocities and the space charge movement will therefore be affected by wind.

Ionic mobility is an important parameter in the ionized field problem. Theoretically speaking, the ionic mobility is a variable which depends upon the electric field strength and ion life time. As discussed in [10], the dependence on the electric field strength needs to be taken into account only if the fields are very high, i.e. near the coronating conductor. The variation of the ionic mobility in the interelectrode space is due to the “aging” of ions.

An ion, on its way to ground or to a conductor with opposite polarity, may become a heavier ion with a lower mobility upon adhesion to a molecule or a particle. This means that the ionic mobility is a function of the ion life time. Studies [10] show that the effect of variation in ionic mobility is not significant in practice, and an average constant mobility may therefore be employed instead. The mobilities of the positive and negative ions are different because of the different generation mechanisms [10]. Under normal atmospheric conditions, they are 1.4×10^{-4} and 1.8×10^{-4} m²/V.s, respectively.

Since the space charge is not uniformly distributed, ion diffusion is unavoidable. The drift velocity of the positive space charge due to ion diffusion is $v_d = -D\nabla\rho$, where D is the diffusion coefficient. Studies [10] show that v_d is negligibly small compared to the drift velocity of the space charge due to the electric field strength.

The magnetic field produced by the current in the conductor will affect the moving space charge, but the effect is neglected in practice.

§1.3 Mathematical Modelling of DC Ionized Fields

1.3.1 Simplifying Assumptions

Since the ionized field problem involves complicated physical processes, appropriate simplifying assumptions are necessary to build a mathematical model which can be solved.

The following assumptions are generally accepted in ionized field analyses:

- (1) The ionized field is time-independent.
- (2) The thickness of the ionization layer around the conductor is negligible and the space charge is generated at the coronating conductor surface.

- (3) Ion diffusion is negligible.
- (4) Ionic mobility is constant.
- (5) The ionized field does not vary along the direction of the transmission line, i.e. the field is two-dimensional.
- (6) Air flow is incompressible and curl-free.

1.3.2 Equations of Ionized Fields

As discussed previously, the space charge generated due to the corona discharge drifts in a manner determined by the electric field and wind; at the same time, the field itself is modified by the space charge. This mutual interaction leads to a state of self-consistence. Under the above assumptions, a bipolar ionized field is described by the following equations:

$$\nabla \cdot \mathbf{E} = (\rho^+ + \rho^-) / \epsilon_0 \quad (1.1)$$

$$\mathbf{j}^+ = k^+ \rho^+ \mathbf{E} + \rho^+ \mathbf{w} \quad (1.2)$$

$$\mathbf{j}^- = -k^- \rho^- \mathbf{E} + \rho^- \mathbf{w} \quad (1.3)$$

$$\nabla \cdot \mathbf{j}^+ = (R_{ion}/e) \rho^+ \rho^- \quad (1.4)$$

$$\nabla \cdot \mathbf{j}^- = -(R_{ion}/e) \rho^+ \rho^- \quad (1.5)$$

$$\mathbf{E} = -\nabla u \quad (1.6)$$

where \mathbf{E} is the electric field strength, \mathbf{j} the corona current density, ρ the space charge density, k the ionic mobility, ϵ_0 the permittivity of free space, \mathbf{w} the wind velocity, R_{ion} the coefficient of recombination of ions, e the absolute value of an electron charge, and u the electric potential. Superscripts "+" and "-" indicate quantities associated with positive and

negative polarities, respectively. It should be noted that $\rho^+ > 0$ for positive space charge and $\rho^- < 0$ for negative space charge. Combining Eqs. (1.1)-(1.6), we have

$$\nabla^2 u = -(\rho^+ + \rho^-)/\epsilon_0 \quad (1.7)$$

$$\nabla \cdot (k^+ \rho^+ \nabla u - \rho^+ w) + (R_{ion}/e) \rho^+ \rho^- = 0 \quad (1.8)$$

$$\nabla \cdot (k^- \rho^- \nabla u + \rho^- w) + (R_{ion}/e) \rho^+ \rho^- = 0 \quad (1.9)$$

Equation (1.7) is Poisson's equation and Eqs. (1.8) and (1.9) are the current continuity equations.

In the case of unipolar ionized fields, all the space charge has the same polarity. Therefore a special case of the above set of equations when either ρ^+ or ρ^- is zero serves as the equations of the unipolar ionized field.

The objective of the ionized analysis is to find the unknown variables u , ρ^+ and ρ^- by solving Eqs. (1.7)-(1.9) subject to the specified boundary conditions.

1.3.3 Boundary Conditions

It is seen that a bipolar ionized field can be represented by the electric potential u and the space charge densities (ρ^+, ρ^-) , which are governed by Poisson's equation and the current continuity equation. These equations are defined on an unbounded two-dimensional domain formed by the conductors above ground, as shown in Fig. 1.1. Since the domain is filled with the unknown space charge, it is not possible to solve the equations over the whole domain. Truncation of the domain is necessary. Since the electric field strength and the space charge density attenuate in magnitude with distance from the conductor, it is

sufficient to truncate the domain with an artificial boundary sufficiently far from the conductor.

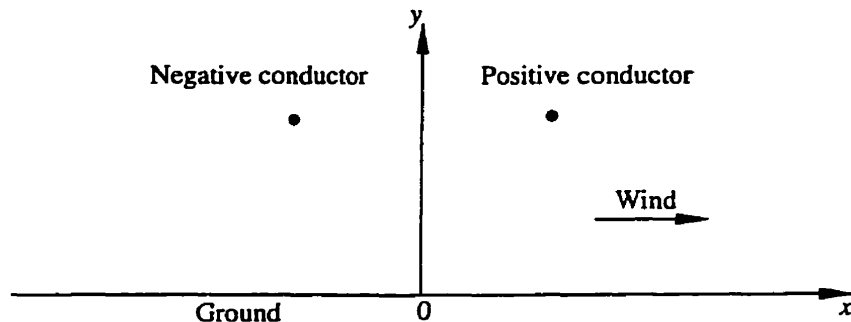


Figure 1.1. DC transmission line.

In order to solve the ionized field in the solution domain, appropriate boundary conditions have to be specified. The potential at the boundary is always taken as a boundary condition. The potentials at the conductor surface and ground are exactly given for a HVDC transmission line; while the potential at the artificial boundary is usually approximated by the corresponding charge-free electric potential. If the space charge density is known over the solution domain, a unique solution for the electric potential can be determined only from Poisson's equation under this boundary condition. In the case of ionized fields, however, besides the electric potential u , the space charge densities (ρ^+, ρ^-) are also to be determined. One additional boundary condition, therefore, must be specified. Conventionally, this additional boundary condition is chosen from the following two conditions:

- (1) The electric field strength at the conductor surface in corona.
- (2) The space charge density at the conductor surface in corona.

Mathematically, these conditions may be expressed respectively as

$$\frac{\partial u}{\partial n} = E_c^+ \text{ for } (x, y) \in \Gamma_c^+, \frac{\partial u}{\partial n} = E_c^- \text{ for } (x, y) \in \Gamma_c^- \quad (1.10)$$

and

$$\rho^+ = \rho_c^+ \text{ for } (x, y) \in \Gamma_c^+, \rho^- = \rho_c^- \text{ for } (x, y) \in \Gamma_c^- \quad (1.11)$$

where Γ_c is the conductor surface, E_c the specified electric field strength on the conductor surface, and ρ_c the specified space charge density on the conductor surface.

The first condition is the most frequently used since it is easily specified using Kaptzov's assumption which states that the electric field strength at the coronating conductor remains at its corona onset level. Studies [15] show that for large corona currents, the electric field strength at the conductor surface decreases for positive polarity and increases for negative polarity; the change is negligible for the range of corona currents encountered in practice. The second condition is difficult to specify directly; instead it is determined from the measured corona current or the given electric field at the conductor surface. Additional assumptions are usually required, e.g., the space charge density is assumed to be uniform at the conductor surface.

The above coupled partial differential equations (PDEs) (1.7)-(1.9) with the specified boundary conditions constitute the boundary value problem of the ionized field.

§1.4 A Review of Existing Solution Techniques

The boundary value problem of the ionized field is a nonlinear problem and difficult to solve. Over the past several decades, considerable efforts have been made to solve the problem, both analytically and numerically.

1.4.1 Analytical Analyses

An analytical solution is possible only for the coaxial cylindrical geometry, the analytical solution for which was first arrived at by Townsend [8] at the beginning of this century. Deutsch [9] attempted an analytical solution for the line-plane configuration based on the following simplifying assumptions:

- (a) The space charge density is constant along any field line.
- (b) The field strength in the presence of the space charge differs from that of the corresponding charge-free field only in magnitude but not in direction.
- (c) The electric field strength of the ionized field at ground is equal to that of the corresponding charge-free field.

Assumptions (a) and (c) are unrealistic in practice since they are valid only when the corona current is vanishingly small [10]. Assumption (b) is “Deutsch’s assumption”. It is the basis of both the approximate analytical solution and the numerical analysis of unipolar DC ionized fields before the 1970’s.

Based on Townsend and Deutsch’s work, Popkov [10] made an approximate analytical analysis of the ionized field on the line-plane geometry. The obtained voltage-current characteristic (Popkov’s formula) takes a similar form as that of the coaxial cylindrical geometry with an empirical constant P being introduced to take into account the nonuniform current distribution at the ground level.

Simpson [11] made a comparison investigation between the measured corona currents and the values predicted by Popkov’s formula. He suggested that a reasonable agreement could be obtained by increasing the empirical constant P (suggested by Popkov) by a fac-

tor of about 3.

Sarma *et al.* [15] compared the numerical results of the voltage-current characteristic with the values obtained from Popkov's formula and concluded that Popkov's formula gives reasonably accurate results for smooth conductors, but the empirical constant P is a function of the line parameters. Unfortunately, there is no theoretical guideline available for evaluating the empirical constant P for general unipolar DC lines.

Based on similar simplifying assumptions, Ceric and Kuffel [25] derived a rigorous expression for the voltage-current relation of the line-plane configuration by using the bipolar coordinate system. Unlike Popkov's formula, all the constants in Ceric-Kuffel's formula can be analytically evaluated for any ratio of the conductor height to the conductor radius.

1.4.2 Numerical Methods Based on Deutsch's Assumption

The above mentioned analytical methods can only be used to obtain the voltage-current characteristic of the ionized field in still air. With the advance of modern computer techniques, the numerical solution of more complicated ionized field problems became a reality.

Sarma *et al.* [15,16,24] were the first to develop a numerical method for solving the ionized fields associated with both unipolar and bipolar HVDC lines. Deutsch's assumption is crucial in their method, since it reduces the ionized field to an one-dimensional problem along the field lines of the corresponding charge-free field. This method was also applied by other researchers [29] to solve the ionized field in the presence of wind.

Deutsch's assumption and the corresponding methods have been criticized by many

researchers. Studies [30,47] show that the field lines of the ionized field in a line-plane configuration in still air do deviate significantly from the field lines of the corresponding charge-free field. It is obvious that Deutsch's assumption is not valid when wind is present.

1.4.3 Numerical Methods Not Based on Deutsch's Assumption

Since 1970, attempts have been made to waive Deutsch's assumption. The work was pioneered by Khalifa *et al.* [17,39]. Their method [17] does not employ Deutsch's assumption, but resorts to another assumption, i.e. the charge density at the point θ on the conductor surface is assumed to be proportional to the average space charge density inside the head of the avalanche developed at the same point θ where θ is the angle measured from the axis of symmetry. Their method is more physical than mathematical, and can only be used to find the voltage-current characteristic.

Janischewskyj and Gela [19] proposed a finite element method (FEM) based approach for solving the unipolar ionized field. The basic idea of their approach is as follows:

- (1) Assume an initial distribution of the space charge density.
- (2) Obtain two solutions u_a and u_b by solving Poisson's equation and the current continuity equation, respectively, using FEM with the assumed charge density.
- (3) Update the charge density by a correction formula

$$\rho_{new} = \rho_{old} + \delta (u_a - u_b) \quad (1.12)$$

and repeat the above steps until convergence is obtained.

They applied this method to solve the ionized field in a coaxial cylindrical configuration represented as an one-dimensional problem. Later, this idea was extended by Abdel-Salam *et al.* [27] to the ionized field of a line-plane geometry in still air. The correction formula for updating the space charge density was taken to be

$$\rho_{new} = \rho_{old} [1 + 0.5f(u_a - u_b) / (u_a + u_b)] \quad (1.13)$$

where the coefficient $f = 0.5$.

The technique in [19] or [27] has not been widely applied since it is hard to construct an efficient correction formula for general practical cases, especially when wind is present.

Takuma *et al.* [22] presented an upwind finite element algorithm for solving the ionized fields including the effects of wind. The iterative procedure may be summarized as follows:

- (1) Assume an initial distribution of the space charge density.
- (2) Solve Poisson's equation using a hybrid FEM-Charge-Simulation-Method (CSM) for the electric potential.
- (3) Solve the current continuity equation by an upwind approach for the charge density based on the calculated electric potential.
- (4) Modify the charge density obtained in step (3) according to the boundary condition at the conductor surface.
- (5) Repeat the above steps until convergence is obtained.

They applied the method to solve the ionized field associated with practical unipolar and bipolar lines in the presence of wind. The space charge density at the conductor surface

was specified as a boundary condition, which was determined by the measured corona current on the full scale transmission line. They latter improved the method by solving for the electric potential from an integral form of the current continuity equation rather than from Poisson's equation [31].

In recent years, a similar iterative procedure as in Takuma's method has been widely utilized by many researchers [32,36,37,40,42,46-50], but different techniques have been employed for solving Poisson's equation and the current continuity equation. For example, Poisson's equation has been solved by CSM [36], the boundary element method (BEM) [32,40,46,47] and FEM [37], with the charge density being updated by solving the current continuity equation (or its equivalent form) using the weighted residual method [36,46] or the upwind finite volume method (FVM) [44]. Alternatively, the current continuity equation has been reduced to an ordinary differential equation along field lines [32,40] or characteristic lines [37,47]. Very recently, the methods for solving the current continuity equation based on a finite element mesh which fits the flux tubes of the field have been suggested [49,50].

Ghione *et al.* [43] suggested a different approach in which the discretization of Poisson's equation is performed by FEM while the current continuity equation discretization is carried out using the finite-box discretization scheme. They considered the nodal charge density and potential values simultaneously as unknowns, and used Newton's method to solve the system of nonlinear equations. The numerical tests were carried out on a line-plane geometry in still air with the ratio of spacing to line radius being 10, which is much smaller than that in typical HVDC transmission systems. Levin *et al.* [44] applied this iter-

ative technique to solve the ionized field in a wire-duct precipitator in still air. They used an approximate solution determined iteratively as the initial value for Newton's method since a very good initial guess for the unknowns is required for its successful application. In the electrostatic precipitator problem, McDonald *et al.* [18] and Lawless *et al.* [20] applied the two-dimensional finite difference method to calculate the ionized fields. The discretized coupled PDEs were solved alternatively using a relaxation technique, respectively. The finite difference method is not popular in ionized field analysis since it is hard to generate a finite difference mesh which fits the problem geometry.

§1.5 Objective of the Thesis

Although the solution algorithms developed in recent years do not resort to Deutsch's assumption, very few numerical results have been presented to show their stability and convergence rate. Secondly, in all the existing solution techniques except for those in [46] which have been tested up to a wind velocity of 12 m/s, the wind velocity considered does not exceed 8 m/s. Moreover, none of them has been tested in the case of a bundled DC line. Thus, the main objective of the thesis is to come up with a stable and efficient algorithm for the evaluation of DC line ionized fields without the above mentioned drawbacks.

CHAPTER 2

FEM BASED OPTIMIZATION ALGORITHM. PART I: FEM FORMULATION

In this chapter, a FEM based algorithm for solving the unipolar ionized fields is developed using a novel solution philosophy [54]. Employing the finite element method, the solution problem of an ionized field has been formulated as an optimization problem, i.e. as a problem of minimizing an objective function whose minimum gives the solution. The effect of wind is taken into account by introducing a scalar potential of its velocity. A method for accurately evaluating the normal component of electric field strength on the boundary is suggested, which will be utilized throughout the thesis.

§2.1 Unipolar Ionized Field Equations

Let the two-dimensional bounded domain be denoted by Ω which consists of two parts: the interior Ω and the boundary $\Gamma = \Gamma_c \cup \Gamma_g \cup \Gamma_a$, where Γ_c is the conductor contour, and Γ_g , Γ_a are the boundary sections defined by ground and the artificial boundary, respectively.

Without loss of generality, it may be assumed that the conductor is positively energized. The electric field in this case can be described by the following coupled equations:

$$\nabla^2 u = -\rho/\epsilon_0 \quad (2.1)$$

$$\nabla \cdot (k\rho \nabla u - \rho w) = 0 \quad (2.2)$$

where u is the electric potential, ρ the charge density, w the wind velocity, k the ionic mobility, and ϵ_0 the permittivity of free space.

Under the assumptions $\nabla \times w = 0$ and $\nabla \cdot w = 0$, w can be expressed in terms of a scalar quantity ξ as

$$w = -k_{max} \nabla \xi \quad (2.3)$$

with

$$\nabla^2 \xi = 0 \quad (2.4)$$

where k_{max} is the maximum value of the ionic mobility in the domain Ω . Eliminating the vector w from the above equations yields

$$\nabla \cdot (k\rho \nabla u + \rho k_{max} \nabla \xi) = 0 \quad (2.5)$$

Denoting

$$k_0 \equiv k/k_{max} \quad (2.6)$$

and

$$q \equiv \rho/\epsilon_0 \quad (2.7)$$

Eqs. (2.1) and (2.5) become

$$\nabla^2 u = -q \quad (2.8)$$

$$\nabla \cdot (k_0 q \nabla u + q \nabla \xi) = 0 \quad (2.9)$$

Equation (2.8) is Poisson's equation and Eq. (2.9) is the current continuity equation including the effect of wind. In these two equations, both u and q are unknown functions of position.

In the case when the ionic mobility k is constant, $k_0 = 1$. Usually, the wind velocity is assumed to be constant and w has only an x -component. Thus ξ is given by

$$\xi(x, y) = -\frac{w}{k_{max}}x \quad (2.10)$$

The boundary conditions for the ionized field are

$$u = \begin{cases} V_0, & (x, y) \in \Gamma_c \\ 0, & (x, y) \in \Gamma_g \\ \Phi(x, y), & (x, y) \in \Gamma_a \end{cases} \quad (2.11)$$

and one of the following two additional boundary conditions:

$$\partial u / \partial n = E_c, \quad (x, y) \in \Gamma_c \quad (2.12)$$

$$q = q_c, \quad (x, y) \in \Gamma_c \quad (2.13)$$

In (2.11), the potential distribution $\Phi(x, y)$ at Γ_a is taken to be the corresponding charge-free potential. The condition (2.12) expresses Kaptzov's assumption, i.e. the electric field strength at the conductor surface in corona remains at the corona onset value E_c .

The quantity q_c in the condition (2.13) can be determined from the corona current measured in a full-scale test [22] or indirectly determined from Kaptzov's assumption. For convenience, we denote the boundary condition (2.11) by BC1 and the boundary conditions (2.12) and (2.13) by BC2(a) and BC2(b), respectively.

§2.2 Finite Element Formulation of Poisson's Equation

The Galerkin finite element method is employed [5]. Assume that the domain Ω is approximated by a finite element mesh which consists of a collection of n_e elements and

n_p nodes. Let $I(\bar{\Omega})$, $I(\Omega)$, $I(\Gamma)$, $I(\Gamma_c)$, $I(\Gamma_g \cup \Gamma_a)$ denote the sets of nodes on $\bar{\Omega}$, Ω , Γ , Γ_c , and $\Gamma_g \cup \Gamma_a$, respectively.

Based on the finite element mesh, the unknown functions $u(x, y)$ and $q(x, y)$ can be approximated respectively by

$$\hat{u} = \{N\} \{u\} \quad \text{in } \bar{\Omega} \quad (2.14)$$

$$\hat{q} = \{N\} \{q\} \quad \text{in } \bar{\Omega} \quad (2.15)$$

where $\{u\} = \{u_1, u_2, \dots, u_{n_p}\}^T$ and $\{q\} = \{q_1, q_2, \dots, q_{n_p}\}^T$ are the vectors of nodal values of $u(x, y)$ and $q(x, y)$, respectively, and $\{N\} = \{N_1, N_2, \dots, N_{n_p}\}$ is the vector representing the global shape functions.

The weighted residual statement for Poisson's equation is

$$\int_{\Omega} N_l (\nabla^2 \hat{u} + \hat{q}) dx dy - \int_{\Gamma} N_l (\partial \hat{u} / \partial n - g) ds = 0, \quad l = 1, 2, \dots, n_p \quad (2.16)$$

where $g = \partial u / \partial n$. The corresponding weak form of the weighted residual statement can be expressed as

$$\int_{\Omega} \nabla N_l \cdot \nabla \hat{u} dx dy - \int_{\Omega} N_l \hat{q} dx dy - \int_{\Gamma} N_l g ds = 0, \quad l = 1, 2, \dots, n_p \quad (2.17)$$

or

$$\int_{\Omega} \nabla N_l \cdot \nabla \hat{u} dx dy - \int_{\Omega} N_l \hat{q} dx dy - \int_{\hat{\Omega}_l \cap \Gamma} N_l g ds = 0, \quad l = 1, 2, \dots, n_p \quad (2.18)$$

where $\hat{\Omega}_l$ is the sub-domain covering the elements adjacent to the node l .

In Eq. (2.18), the quantity g on $\hat{\Omega}_l \cap \Gamma$ may be approximated by a constant which is denoted by g_l , i.e.

$$g \approx g_l, \text{ on } \hat{\Omega}_l \cap \Gamma \quad (2.19)$$

Substitution of the expansions of \hat{u} and \hat{q} in Eq. (2.18) leads to the following system of linear equations:

$$[K] \{u\} - [P] \{q\} - [Z] \{g\} = \{0\} \quad (2.20)$$

where the vector $\{g\}$ is defined such that its element $g_i = \partial u / \partial n|_i$ if $i \in I(\Gamma)$ and $g_i = 0$ if $i \notin I(\Gamma)$, and the matrices $[K]$, $[P]$ and $[Z]$ are defined as

$$[K] = \int_{\Omega} \left(\frac{\partial}{\partial x} \{N\}^T \frac{\tau \partial}{\partial x} \{N\} + \frac{\partial}{\partial y} \{N\}^T \frac{\tau \partial}{\partial y} \{N\} \right) dx dy \quad (2.21)$$

$$[P] = \int_{\Omega} \{N\}^T \{N\} dx dy \quad (2.22)$$

$$[Z] = \text{diag} \{Z_1, Z_2, \dots, Z_{n_p}\} \quad (2.23)$$

with

$$Z_l = \int_{\hat{\Omega}_l \cap \Gamma} N_l ds \quad (2.24)$$

They can be constructed from the individual element contributions

$$[K]_e = \int_{\Omega_e} \left(\frac{\partial}{\partial x} \{N\}_e^T \frac{\tau \partial}{\partial x} \{N\}_e + \frac{\partial}{\partial y} \{N\}_e^T \frac{\tau \partial}{\partial y} \{N\}_e \right) dx dy \quad (2.25)$$

$$[P]_e = \int_{\Omega_e} \{N\}_e^T \{N\}_e dx dy \quad (2.26)$$

$$Z_r^e = \int_{\Omega_e \cap \Gamma} N_r^e ds \quad (2.27)$$

where Ω_e represents the e th element, and $\{N\}_e = \{N_r^e\}$ denotes the vector representing the local shape functions defined over each element Ω_e .

The matrix $[K]$ is a sparse and symmetric matrix of $n_p \times n_p$, and $[P]$ is also sparse and symmetric with $[P]$ having the same structure as $[K]$.

§2.3 Finite Element Formulation of the Current Continuity Equation

By using the relation

$$\nabla \cdot (q \nabla u) = \nabla q \cdot \nabla u + q \nabla^2 u \quad (2.28)$$

we rewrite the current continuity equation as

$$\nabla (k_0 q) \cdot \nabla u + k_0 q \nabla^2 u + \nabla q \cdot \nabla \xi + q \nabla^2 \xi = 0 \quad (2.29)$$

By noting that $\nabla^2 \xi = 0$ and $\nabla^2 u = -q$, we have

$$\nabla (k_0 q) \cdot \nabla u + \nabla q \cdot \nabla \xi - k_0 q^2 = 0 \quad (2.30)$$

The weighted residual statement for Eq. (2.30) is

$$\int_{\Omega} N_l [\nabla (k_0 \hat{q}) \cdot \nabla \hat{u} + \nabla \hat{q} \cdot \nabla \xi - k_0 \hat{q}^2] dx dy = 0, \quad l = 1, 2, \dots, n_p \quad (2.31)$$

Now let

$$\xi = \hat{\xi} = \{N\} \{\xi\} \quad (2.32)$$

where $\{\xi\} = \{\xi_1, \xi_2, \dots, \xi_{n_p}\}^T$ denotes the vector of nodal values of $\xi(x, y)$. Inserting the expansions of \hat{u} , \hat{q} and $\hat{\xi}$ in Eq. (2.31), we obtain the following system of nonlinear equations:

$$\{q\}^T [A]_l \{u\} + \{q\}^T [\tilde{A}]_l \{\xi\} - \{q\}^T [B]_l \{q\} = 0, \quad l = 1, 2, \dots, n_p \quad (2.33)$$

where

$$[A]_l = \int_{\Omega} N_l \left[\frac{\partial}{\partial x} (k_0 \{N\}^T) \frac{\partial}{\partial x} \{N\} + \frac{\partial}{\partial y} (k_0 \{N\}^T) \frac{\partial}{\partial y} \{N\} \right] dx dy \quad (2.34)$$

$$[\tilde{A}]_l = \int_{\Omega} N_l \left(\frac{\partial}{\partial x} \{N\}^T \frac{\partial}{\partial x} \{N\} + \frac{\partial}{\partial y} \{N\}^T \frac{\partial}{\partial y} \{N\} \right) dx dy \quad (2.35)$$

$$[B]_l = \int_{\Omega} k_0 N_l \{N\}^T \{N\} dx dy \quad (2.36)$$

These matrices can be constructed from the individual element contributions

$$[A]_l^e = k_{0e} \int_{\Omega_e} N_l^e \left(\frac{\partial}{\partial x} \{N\}_e^T \frac{\partial}{\partial x} \{N\}_e + \frac{\partial}{\partial y} \{N\}_e^T \frac{\partial}{\partial y} \{N\}_e \right) dx dy \quad (2.37)$$

$$[\tilde{A}]_l^e = k_{0e}^{-1} [A]_l^e \quad (2.38)$$

$$[B]_l^e = k_{0e} \int_{\Omega_e} N_l^e \{N\}_e^T \{N\}_e dx dy \quad (2.39)$$

where Ω_e is an element associated with node l , and k_{0e} represents the ionic mobility on Ω_e . It should be noted that k_{0e} is treated as a constant over each element Ω_e .

It is observed that $[A]_l$, $[\tilde{A}]_l$ and $[B]_l$ are all sparse and symmetric. The element $A_{rs}^{(l)}$ in $[A]_l$ is non-zero only if nodes r, s share the same element with the node l . If the number of nodes associated with the node l is $\beta_l - 1$, the number of non-zero elements in the matrix $[A]_l$ is less than β_l^2 . The same thing holds for the matrices $[\tilde{A}]_l$ and $[B]_l$.

When the ionic mobility in Ω is assumed to be a constant, $k_0 = 1$. In this case, $[\tilde{A}]_l$ is equal to $[A]_l$, and Eq. (2.33) becomes

$$\{q\}^T [A]_l (\{u\} + \{\xi\}) - \{q\}^T [B]_l \{q\} = 0, \quad l = 1, 2, \dots, n_p \quad (2.40)$$

§2.4 Equivalent Optimization Problem

Based on the FEM, Poisson's equation and the current continuity equation have been discretized into a group of linear and nonlinear equations, respectively, with $\{u\}$ and $\{q\}$ being the unknowns. Denote Eqs. (2.20) and (2.33), respectively, by

$$\{\phi\} = \{0\} \quad (2.41)$$

$$\Psi_l = 0, \quad l = 1, 2, \dots, n_p \quad (2.42)$$

with

$$\{\phi\} \equiv \{\phi_1, \phi_2, \dots, \phi_{n_p}\}^T = [K] \{u\} - [P] \{q\} - [Z] \{g\} \quad (2.43)$$

$$\Psi_l \equiv \{q\}^T [A]_l \{u\} + \{q\}^T [\tilde{A}]_l \{\xi\} - \{q\}^T [B]_l \{q\} \quad (2.44)$$

Now regroup Eq. (2.41) as

$$\phi_l(\{u\}, \{q\}) = 0 \quad \text{for all } l \in I(\Omega) \quad (2.45)$$

$$\phi_l(\{u\}, \{q\}, \{g\}_2) = 0 \quad \text{for all } l \in I(\Gamma_c) \quad (2.46)$$

$$\phi_l(\{u\}, \{q\}, \{g\}_3) = 0 \quad \text{for all } l \in I(\Gamma_g \cup \Gamma_a) \quad (2.47)$$

where $\{g\}_2$ and $\{g\}_3$ are the vectors of nodal values of $g = \partial u / \partial n$ at Γ_c and $\Gamma_g \cup \Gamma_a$, respectively.

Equation (2.45) corresponds to the interior nodes and reflects the influence of the charge density on the potential distribution. Once the charge density in Ω is given, the potential distribution is determined uniquely by Eq. (2.45) with the boundary nodal potentials being specified. Equations (2.46) and (2.47) reflect the constrained relationship between the potential gradient at the boundary Γ and the distributions of the potential and

charge density in the domain Ω . They can be used to impose the second kind of boundary conditions, but in the case of ionized fields, only Eq. (2.46) is used.

Therefore, under the boundary conditions BC1 and BC2(a), the numerical solution for the unipolar ionized field can be found by solving the following nonlinear system of equations:

$$\begin{aligned}\phi_l(\{u\}, \{q\}) &= 0 && \text{for all } l \in I(\Omega) \\ \psi_l(\{u\}, \{q\}) &= 0 && \text{for all } l \in I(\bar{\Omega}) \\ u_l - u_l^* &= 0 && \text{for all } l \in I(\Gamma) \\ \phi_l(\{u\}, \{q\}, \{g^*\}_2) &= 0 && \text{for all } l \in I(\Gamma_c)\end{aligned}\tag{2.48}$$

where “*” indicates the specified values at the boundary, while under the boundary conditions BC1 and BC2(b), equation $\phi_l(\{u\}, \{q\}, \{g^*\}_2) = 0$ in the above system of equations should be replaced by $q_l - q_l^* = 0$.

The above system of equations is over-determined, which means that the number of equations in the system is larger than that of the unknowns. In this case, the solution can be sought by minimizing a nonnegative function F which is constructed such that its minimum gives the solution to the nonlinear system. A straightforward choice for F is

$$F = \frac{1}{2} \left(\sum_{l \in I(\bar{\Omega})} \psi_l^2 + \sum_{l \in I(\Omega)} \phi_l^2 + \sum_{l \in I(\Gamma)} (u_l - u_l^*)^2 + \sum_{l \in I(\Gamma_c)} \tilde{\phi}_l^2 \right) \tag{2.49}$$

where the term $\sum_{l \in I(\Gamma)} (u_l - u_l^*)^2$ corresponds to the boundary condition BC1 and the

term $\sum_{l \in I(\Gamma_c)} \tilde{\phi}_l^2$ corresponds to the additional boundary condition BC2(a) or BC2(b), in

which $\tilde{\phi}_l$ is defined as

$$\bar{\Phi}_l = \begin{cases} \Phi_l([u], [q], [g^*]_2) & \text{for boundary condition BC2(a)} \\ (q_l - q_l^*) & \text{for boundary condition BC2(b)} \end{cases} \quad (2.50)$$

This problem is a nonlinear least-squares problem, which is a special type of optimization problem, with the objective function F . Obviously, F converges to zero when the variables converge to the solution of the system of equations (2.48).

§2.5 Evaluation of Matrices Involved in Equivalent Optimization Problem

Here we only consider the case of 3-node elements. The shape functions of a 3-noded element as shown in Fig. 2.1(a) are

$$N_r(x, y) = \frac{1}{2A_e} (a_r x + b_r y + c_r), \quad r = i, j, l \quad (2.51)$$

with

$$a_i = y_j - y_l, \quad a_j = y_l - y_i, \quad a_l = y_i - y_j \quad (2.52)$$

$$b_i = x_l - x_j, \quad b_j = x_i - x_l, \quad b_l = x_j - x_i \quad (2.53)$$

$$A_e = (a_i b_j - a_j b_i) / 2 \quad (2.54)$$

where x_i, y_j are the coordinates of the node i and A_e is the area of the element e .

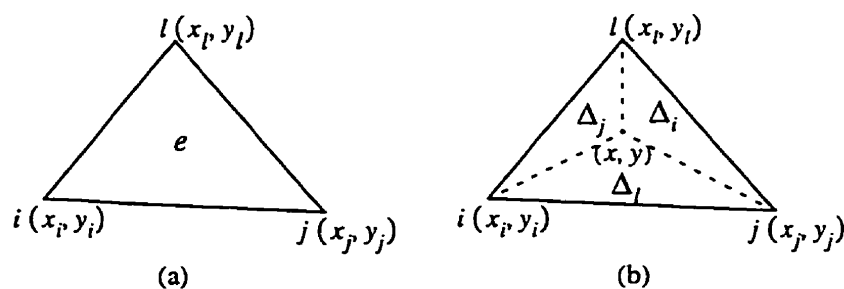


Figure 2.1. Three-noded element.

The derivatives of the shape functions are

$$\frac{\partial N_r}{\partial x} = \frac{1}{2A_e} a_r, \quad r = i, j, l \quad (2.55)$$

$$\frac{\partial N_r}{\partial y} = \frac{1}{2A_e} b_r, \quad r = i, j, l \quad (2.56)$$

Now let us define the area coordinates as

$$\lambda_r = \Delta_r / A_e, \quad r = i, j, l \quad (2.57)$$

where $\Delta_r, r = i, j, l$ are the areas of the triangles corresponding to the point (x, y) , as shown in Fig. 2.1(b). It can be shown that there exist the following relations between the area coordinates and the shape functions:

$$N_r^e = \lambda_r, \quad r = i, j, l \quad (2.58)$$

Also, we have the following two formulas

$$\int_{\Omega_e} \lambda_i^p \lambda_j^m \lambda_l^t dx dy = 2A_e \frac{p! m! t!}{(p+m+t+2)!} \quad (2.59)$$

$$\int_{\Omega_e \cap \Gamma} \lambda_j^m \lambda_l^t ds = L_e \frac{m! t!}{(m+t+1)!} \quad (2.60)$$

where L_e is the length of the boundary element $\Omega_e \cap \Gamma$, ds is the differential length, and p, m, t are non-negative integers.

From Eqs. (2.55)-(2.60), we have

$$K_{rs}^e = \frac{1}{4A_e} (a_r a_s + b_r b_s), \quad r, s = i, j, l \quad (2.61)$$

$$P_{rs}^e = \begin{cases} A_e/6, & \text{if } r = s \\ A_e/12, & \text{otherwise} \end{cases} \quad (2.62)$$

$$Z_e = L_e/2 \quad (2.63)$$

$$A_{rs}^{(l)e} = \frac{1}{12A_e} (a_r a_s + b_r b_s), \quad r, s = i, j, l \quad (2.64)$$

$$B_{rs}^{(l)e} = \begin{cases} A_e/10, & \text{if } r = s = l \\ A_e/60, & \text{if } r \neq s, r \neq l, \text{ and } s \neq l \\ A_e/30, & \text{otherwise} \end{cases} \quad (2.65)$$

where K_{rs}^e , P_{rs}^e , $A_{rs}^{(l)e}$ and $B_{rs}^{(l)e}$ ($r, s = i, j, l$) are the elements of the matrices $[K]_e$, $[P]_e$, $[A]_l$ and $[B]_l$, respectively. The matrices $[K]$, $[P]$, $[Z]$, $[A]_l$ and $[B]_l$ can be obtained by assembling all the element contributions.

It is observed that the nonzero elements of the matrix $[K]$ and the nonzero elements of the matrix $[A]_l$ have the same order in magnitude. The similar thing is true for the matrices $[P]$ and $[B]_l$.

§2.6 Scaling

The variables in the above problem may differ by several orders of magnitude in numerical values, which will affect the efficiency and rate of convergence of the iterative methods.

This problem is overcome by rescaling the variables. Let

$$u_{max} = \max \{u_1, u_2, \dots, u_{n_p}\} \quad (2.66)$$

$$q_{max} = \max \{q_1, q_2, \dots, q_{n_p}\} \quad (2.67)$$

$$d_{max} = \max \{\sqrt{K_{11}}, \sqrt{K_{22}}, \dots, \sqrt{K_{n_p n_p}}\} \quad (2.68)$$

$$[D] = \text{diag} \{ \sqrt{1/K_{11}}, \sqrt{1/K_{22}}, \dots, \sqrt{1/K_{n_p n_p}} \} \quad (2.69)$$

Equation (2.20) is rewritten as

$$\begin{aligned} & ([D] [K] [D]) \left(\frac{1}{u_{\max} d_{\max}} [D]^{-1} \{u\} \right) - \left(\frac{q_{\max}}{u_{\max}} [D] [P] [D] \right) \left(\frac{1}{q_{\max} d_{\max}} [D]^{-1} \{q\} \right) \\ & - \left(\frac{1}{u_{\max} d_{\max}} [D] [Z] [D] \right) ([D]^{-1} \{g\}) = \{0\} \end{aligned} \quad (2.70)$$

and Eq. (2.33) as

$$\begin{aligned} & \left(\frac{1}{q_{\max} d_{\max}} [D]^{-1} \{q\} \right)^T ([D] [A]_l [D]) \left(\frac{1}{u_{\max} d_{\max}} [D]^{-1} \{u\} \right) \\ & + \left(\frac{1}{q_{\max} d_{\max}} [D]^{-1} \{q\} \right)^T ([D] [\tilde{A}]_l [D]) \left(\frac{1}{u_{\max} d_{\max}} [D]^{-1} \{\xi\} \right) \\ & - \left(\frac{1}{q_{\max} d_{\max}} [D]^{-1} \{q\} \right)^T \left(\frac{q_{\max}}{u_{\max}} [D] [B]_l [D] \right) \left(\frac{1}{q_{\max} d_{\max}} [D]^{-1} \{q\} \right) = 0, \\ l &= 1, 2, \dots, n_p \end{aligned} \quad (2.71)$$

Therefore the vectors and the matrices in the above equations are rescaled as follows:

$$\{u\} \Leftarrow \frac{1}{u_{\max} d_{\max}} [D]^{-1} \{u\} \quad (2.72)$$

$$\{q\} \Leftarrow \frac{1}{q_{\max} d_{\max}} [D]^{-1} \{q\} \quad (2.73)$$

$$\{g\} \Leftarrow [D]^{-1} \{g\} \quad (2.74)$$

$$\{\xi\} \Leftarrow \frac{1}{u_{\max} d_{\max}} [D]^{-1} \{\xi\} \quad (2.75)$$

$$[K] \Leftarrow [D] [K] [D] \quad (2.76)$$

$$[P] \Leftarrow \frac{q_{\max}}{u_{\max}} [D] [P] [D] \quad (2.77)$$

$$[Z] \Leftarrow \frac{1}{u_{max} d_{max}} [D] [Z] [D] \quad (2.78)$$

$$[A]_l \Leftarrow [D] [A]_l [D] \quad (2.79)$$

$$[\tilde{A}]_l \Leftarrow [D] [\tilde{A}]_l [D] \quad (2.80)$$

$$[B]_l \Leftarrow \frac{q_{max}}{u_{max}} [D] [B]_l [D] \quad (2.81)$$

After scaling, the symmetric and sparse properties of the matrices remain unchanged, but the values of the elements in the vectors $\{u\}$ and $\{q\}$ will be approximately between 0 and 1. The principal diagonal elements in the matrix $[K]$ are 1. In the case of 3-noded elements, the maximum element in each of the matrices $[A]_l$ and $[\tilde{A}]_l$, $l = 1, 2, \dots, n_p$, are of order 1, and the principal diagonal element of the l th column in the matrix $[P]$ has the same order of magnitude as the maximum element in the matrix $[B]_l$. As confirmed by numerical investigation, these features ensure that ϕ_l and ψ_l , $l = 1, 2, \dots, n_p$, are of the same order of magnitude and similar changes in the variables lead to similar changes in the objective function. This is what a “well-scaled” problem requires.

For a line-plane unipolar DC system, q_{max} can be determined by using an equivalent coaxial cylindrical geometry. The equivalent coaxial cylindrical geometry is that in which the maximum value of E , which occurs at the inner conductor surface, is equal to the average value of E at the line conductor surface in the line-plane system, with the same radius and voltage for these two conductors. From experience, the outer conductor radius R_{eq} of this equivalent coaxial cylindrical geometry is about $1.5H$ to $2H$, where H is the conductor height.

§2.7 Calculation of Electric Field Strength on the Boundary

Accurate calculation of the electric field strength on the conductor surface Γ_c and ground Γ_g is important in the ionized field analysis. Since the electric field on $\Gamma_c \cup \Gamma_g$ has no tangential component, it can be calculated using the discretized Poisson's equation (2.20) after $\{u\}$ and $\{q\}$ have been obtained.

From Eq. (2.20), the elements of the vector $\{g\}$ can be easily calculated as

$$g_i = \begin{cases} \frac{1}{Z_i} \left(\sum_j K_{ij} u_j - \sum_j P_{ij} q_j \right), & \text{if } i \in I(\Gamma) \\ 0, & \text{otherwise} \end{cases} \quad (2.82)$$

The electric field strength on the conductor surface and ground is then obtained by

$$E|_{\text{at node } i} = g_i, \text{ for } i \in I(\Gamma_c) \text{ or } i \in I(\Gamma_g) \quad (2.83)$$

noting that the direction of electric field on the boundary $\Gamma_c \cup \Gamma_g$ is assumed to be opposite to n , where n is the outward normal to the boundary.

Studies [5,41] show that the accuracy of the electric field strength on the boundary obtained by using this method is better than that obtained by using the derivatives of the piecewise interpolation function \hat{u} .

It should be mentioned that the above method is used to calculate the electric field strength on the conductor surface and ground not only in the algorithm under consideration but also in other algorithms in the thesis.

§2.8 Summary

A new solution method is presented for solving the ionized field of unipolar HVDC transmission lines. The main characteristics of the method are summarized as follows.

Based on the finite element method, the boundary value problem is transformed into a least-squares problem, which is a special type of optimization problem. The iterative methods available for solving this problem are well established on a firm mathematical basis.

The proposed method is generally applicable for solving unipolar ionized fields. The formulation of this method does not depend on the problem geometry and therefore it can be used to solve the practical ionized field without much simplification in the actual geometry.

The treatment of the boundary conditions BC2(a) and BC2(b) does not require that E_c and q_0 be constant on the conductor surface if they can be quantitatively determined.

Wind is taken into account in the ionized field equations by introducing a scalar quantity ξ . The wind velocity is not necessarily required to be uniform if the scalar quantity ξ can be determined by measurement or calculation. Also, the ionic mobility may be allowed to be variable over the solution domain.

The electric field strength at ground level is calculated from the finite element equation. The accuracy of the field strength obtained in this manner is better than that obtained from the derivatives of the approximation function \hat{u} .

Chapter 3 of the thesis discusses solution techniques and presents the results obtained when applied to a test example of a coaxial cylindrical geometry and to a practical unipolar configuration both in the presence and absence of wind. It is shown that the presented method yields satisfactory results and is highly efficient in terms of the rate of convergence and required CPU time.

CHAPTER 3

FEM BASED OPTIMIZATION ALGORITHM. PART II: SOLUTION TECHNIQUES

In Chapter 2, the solution of a unipolar ionized field has been formulated as a nonlinear optimization problem including the effect of wind based on the FEM. This chapter presents the modified Gaussian algorithm [55] for solving this optimization problem. Specific techniques of incorporating the special structure of the optimization problem in the algorithm have been developed to economize the requirements for the computer memory and CPU time. Numerical tests are carried out on a coaxial cylindrical geometry and on a line-plane geometry both in the absence and in the presence of wind. The symbols already defined in Chapter 2 will not be re-explained.

§3.1 Introduction to Iterative Methods

The available iterative methods [2-4] for solving nonlinear optimization problems can be grouped into two classes: direct search methods and descent techniques. The former methods are in general less efficient than the latter ones, especially for large scale optimization problems, i.e. problems with a large number of unknowns. The latter methods have a firm mathematical basis and are also well established.

If we denote the objective function of an optimization problem by $F(\{v\})$ where $\{v\}$ is a vector of n unknowns, each iteration of the descent technique involves

(1) Finding a direction of correction $\{z\}^{(k)}$.

(2) Determining a steplength $\lambda^{(k)}$ which satisfies

$$F(\{\nu\}^{(k)} + \lambda^{(k)} \{z\}^{(k)}) = \min_{\lambda} F(\{\nu\}^{(k)} + \lambda \{z\}^{(k)}) \quad (3.1)$$

(3) Performing the correction step

$$\{\nu\}^{(k+1)} = \{\nu\}^{(k)} + \lambda^{(k)} \{z\}^{(k)} \quad (3.2)$$

where the superscripts (k) and $(k+1)$ represent the iteration number. The steplength $\lambda^{(k)}$ is a scalar which is a measure of the distance along the direction of correction $\{z\}^{(k)}$ between two successive iteration points $\{\nu\}^{(k)}$ and $\{\nu\}^{(k+1)}$, and can be sought using the golden section method.

The descent techniques differ from each other only in the type of the direction of correction $\{z\}^{(k)}$. Among the techniques available for defining this direction, the modified Gaussian algorithm is a widely accepted choice for the nonlinear least-squares problem, i.e. its objective function has the form of a sum of least-squares.

§3.2 The Modified Gaussian Algorithm

Consider the objective function

$$F(\{\nu\}) = \frac{1}{2} \sum_{l=1}^m f_l^2(\{\nu\}) \quad (3.3)$$

where $\{\nu\}$ is a vector of n unknowns and the minimum value of F is zero.

In the modified Gaussian algorithm, the direction of correction $\{z\}^{(k)}$ is determined from the equation

$$[T]^{(k)} \{z\}^{(k)} = -\nabla F^{(k)} \quad (3.4)$$

where the matrix $[T]$ is defined as

$$[T] = \left[\sum_l \frac{\partial f_l}{\partial v_i} \frac{\partial f_l}{\partial v_j} \right]_{n \times n} \quad (3.5)$$

and the vector ∇F is the gradient of the objective function F , which is defined as

$$\nabla F = \left\{ \frac{\partial F}{\partial v_1}, \frac{\partial F}{\partial v_2}, \dots, \frac{\partial F}{\partial v_n} \right\}^T \quad (3.6)$$

noting that the superscript (k) has been dropped for simplicity.

The matrix $[T]$ in this algorithm may have a large condition number and hence the direction generated may not be very favourable. To overcome this problem, some modifications are necessary. One popular choice is to regularize the solution of (3.4) by replacing the matrix $[T]$ by $([T] + \gamma[I])$, where the regularization parameter γ is a positive number. The matrix $([T] + \gamma[I])$ is a positive definite matrix and the generated direction of correction is always downhill so that the modified Gaussian algorithm is, in theory, convergent. The efficiency of the method is significantly affected by the value of the parameter γ , but the choice of γ on a mathematical basis is difficult. It is recommended, in practice, that γ be updated based on computational progress. For the ionized field problems of the models presented in this chapter, satisfactory results are obtained by assigning γ a small value, i.e. $\gamma = 10^{-8}$.

In this algorithm, the computer memory and CPU time is mostly determined by forming and solving Eq. (3.4) in each iteration. If the $n \times n$ matrix $[T]$ is not sparse, $O(n^2)$ words of computer memory and $O(n^3)$ arithmetic operations are required if a factoriza-

tion method is employed. Therefore the application of this method in the solution of large scale nonlinear problems is preferable only if the matrix $[T]$ is a banded matrix.

§3.3 Consideration of Special Structure of Objective Function as Applied to Ionized Fields

As explained in Chapter 2, the matrices involved in the objective function are derived from the FEM and therefore are highly sparse, i.e. relatively few of the elements in the matrices are nonzero. Taking advantage of the sparsity structure is crucial in order to apply the modified Gaussian algorithm.

The objective function in Eq. (3.3), in the context of positive unipolar ionized fields, is

$$F(\{v\}) = \frac{1}{2} \left(\sum_{l \in I(\Omega)} \Psi_l^2 + \sum_{l \in I(\Omega)} \Phi_l^2 + \sum_{l \in I(\Gamma)} (u_l - u_l^*)^2 + \sum_{l \in I(\Gamma_c)} \bar{\Phi}_l^2 \right) \quad (3.7)$$

where

$$\{v\} = \{v_1, v_2, \dots, v_n\}^T = \{u_1, q_1, u_2, q_2, \dots, u_{n_p}, q_{n_p}\}^T \quad (3.8)$$

$$\bar{\Phi}_l = \begin{cases} \phi_l(\{u\}, \{q\}, \{g^*\}_2), & \text{for boundary condition BC2(a)} \\ (q_l - q_l^*), & \text{for boundary condition BC2(b)} \end{cases} \quad (3.9)$$

with $n = 2n_p$, noting that the superscript “+” is dropped for simplicity.

With the variables (nodal values of u and of q) arranged in the manner as in Eq. (3.8), the matrix $[T]$ is a banded matrix if the matrix $[K]$ is a banded matrix. Actually, the matrix $[K]$ can always be ensured to be a banded matrix by an appropriate node numbering sequence. In the case of BC2(a), with the ionic mobility being constant over the solution domain, from Eqs. (3.5), (3.7)-(3.9), it is seen that the elements of $[T]$ are

$$T_{2r-1, 2s-1} = \sum_{l \in I(\Omega)} \frac{\partial \Psi_l}{\partial u_r} \frac{\partial \Psi_l}{\partial u_s} + \sum_{l \in I(\Omega) \cup I(\Gamma_c)} \frac{\partial \Phi_l}{\partial u_r} \frac{\partial \Phi_l}{\partial u_s} + \delta_{rs} \quad (3.10)$$

$$T_{2r-1,2s} = T_{2s,2r-1} = \sum_{l \in I(\Omega)} \frac{\partial \psi_l}{\partial u_r} \frac{\partial \psi_l}{\partial q_s} + \sum_{l \in I(\Omega) \cup I(\Gamma_c)} \frac{\partial \phi_l}{\partial u_r} \frac{\partial \phi_l}{\partial q_s} \quad (3.11)$$

$$T_{2r,2s} = \sum_{l \in I(\Omega)} \frac{\partial \psi_l}{\partial q_r} \frac{\partial \psi_l}{\partial q_s} + \sum_{l \in I(\Omega) \cup (I(\Gamma_c))} \frac{\partial \phi_l}{\partial q_r} \frac{\partial \phi_l}{\partial q_s} \quad (3.12)$$

where

$$\delta_{rs} = \begin{cases} 1, & \text{if } r = s \in I(\Gamma) \\ 0, & \text{otherwise} \end{cases} \quad (3.13)$$

$$\frac{\partial \psi_l}{\partial u_r} = \begin{cases} \sum_{s \in \tilde{I}_{(l)}^N} A_{rs}^{(l)} q_s, & \text{if } r \in \tilde{I}_{(l)}^N \\ 0, & \text{otherwise} \end{cases} \quad (3.14)$$

$$\frac{\partial \phi_l}{\partial u_r} = \begin{cases} K_{lr}, & \text{if } r \in \tilde{I}_{(l)}^N \\ 0, & \text{otherwise} \end{cases} \quad (3.15)$$

$$\frac{\partial \psi_l}{\partial q_r} = \begin{cases} \sum_{s \in \tilde{I}_{(l)}^N} A_{rs}^{(l)} (u_s + \xi_s) - 2 \sum_{s \in \tilde{I}_{(l)}^N} B_{rs}^{(l)} q_s, & \text{if } r \in \tilde{I}_{(l)}^N \\ 0, & \text{otherwise} \end{cases} \quad (3.16)$$

$$\frac{\partial \phi_l}{\partial q_r} = \begin{cases} -P_{lr}, & \text{if } r \in \tilde{I}_{(l)}^N \\ 0, & \text{otherwise} \end{cases} \quad (3.17)$$

where $\tilde{I}_{(l)}^N = I_{(l)}^N \cup \{l\}$ with $I_{(l)}^N$ being the subset of nodes associated with the node l ,

as shown in Fig. 3.1. Since $\partial \psi_l / \partial u_r = \partial \psi_l / \partial q_r = 0$ and $\partial \phi_l / \partial u_r = \partial \phi_l / \partial q_r = 0$ for

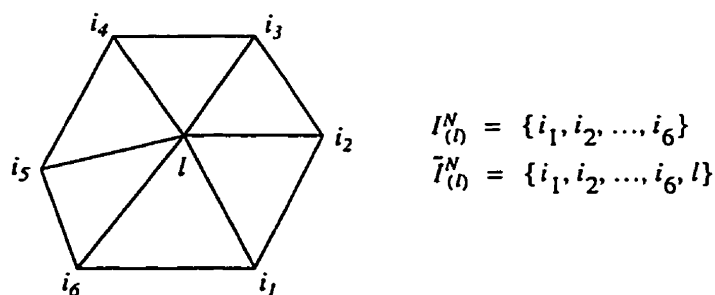


Figure 3.1. The subsets $I_{(l)}^N$ and $\tilde{I}_{(l)}^N$.

$r \notin \tilde{I}_{(l)}^N$, the elements $T_{2r-1,2s-1} \neq 0$, $T_{2r-1,2s} = T_{2s,2r-1} \neq 0$ and $T_{2r,2s} \neq 0$ only if there exists at least one nodal point l_0 at which $r, s \in \tilde{I}_{(l_0)}^N$. This illustrates the sparsity of matrix $[T]$. It can be shown that if the average bandwidth of the matrix $[K]$ is m_K , then that of $[T]$ is $m_T = 4m_K$. Thus, if the LU factorization scheme is employed, the computer memory required for $[T]$ is $m_T(2n_p)$ words and the number of arithmetic operations for solving Eq. (3.4) is of order $O(m_T^2 n_p)$ or $O(16m_K^2 n_p)$. Usually m_K and hence m_T are much smaller than $2n_p$ and, therefore, the saving in computer storage and computational work is significant compared to that in the case when $[T]$ is a full matrix.

Noting the sparsity and symmetry characteristics, the memory required for storing all other matrices such as $[K]$, $[P]$, $[A]_l$, $[B]_l$, etc. is of order $O(\bar{\beta}^2 n_p)$, where $\bar{\beta}$ denotes the average number of nodes in the subset $\tilde{I}_{(l)}^N$, and the number of arithmetic operations for evaluating all ψ_l and ϕ_l as well as their partial derivatives is also of order $O(\bar{\beta}^2 n_p)$. The evaluation of F and ∇F requires only $O(n_p)$ arithmetic operations and that of $[T]$ requires $O(2m_T n_p)$ operations. Since $\bar{\beta}$ is a fixed number and $\bar{\beta} \ll m_T$ (e.g., for the 3-noded mesh, $\bar{\beta}=7$), the computer memory and computational work required for the iterative program is mainly due to the solution of Eq. (3.4).

§3.4 Schemes for Application of Boundary Conditions at Conductor Surface

There are several alternative ways to apply the boundary conditions at the conductor surface for the unipolar ionized field problem, which are described as follows.

Scheme I: Apply the modified Gaussian algorithm to solve the optimization problem corresponding to the boundary conditions BC1 and BC2(a).

Scheme II: Apply the modified Gaussian algorithm to solve the optimization problem corresponding to the boundary conditions BC1 and BC2(b).

Scheme III: This scheme is an alternative way to apply the boundary condition BC2(a) by using Scheme II instead of Scheme I. In Scheme III it is required to assume that the charge density at the conductor surface is uniform. From three different chosen values q_{c1} , q_{c2} and q_{c3} of q at Γ_c , Scheme II is applied to obtain three average values E_{c1} , E_{c2} and E_{c3} of the electric field strength E at Γ_c and then the interpolation method is used to determine q_c . This is schematically shown in Fig. 3.2. Based on q_c thus obtained, Scheme II is applied. If the resultant average value of E is sufficiently close to E_c , the solution is

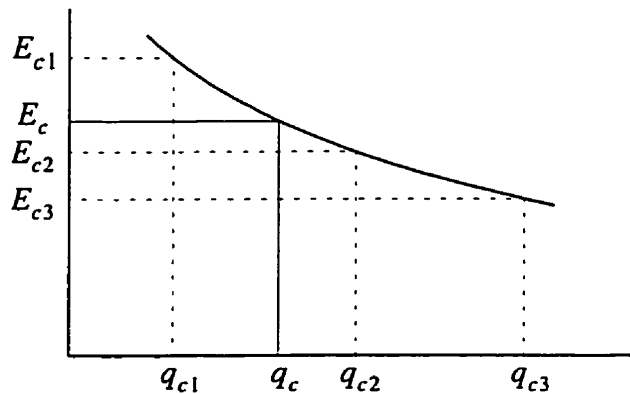


Figure 3.2. Schematic demonstration of Scheme III.

obtained by using this value; otherwise one of the three values (q_{c1} , q_{c2} and q_{c3}), whose corresponding E at Γ_c is the most different from E_c , is replaced by q_c and the above procedure repeated.

Scheme IV: This scheme is used for determining the quantity q_c in the boundary condition BC2(b) according to the measured corona current I_c . The charge density at the conductor surface is assumed to be constant as in Scheme III. Three different values q_{c1} , q_{c2} and q_{c3} of q are chosen at Γ_c , and Scheme II is applied to obtain three corresponding values I_{c1} , I_{c2} and I_{c3} . The quantity q_c is then determined by following a procedure similar to that in Scheme III.

Since the measured data are not available for the corona current I_c , numerical results using Scheme IV can not be generated.

§3.5 Numerical Tests on a Coaxial Cylindrical Model

A coaxial cylindrical model, as shown in Fig. 3.3, was used to test the performance of the

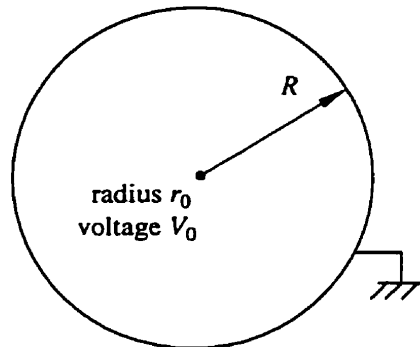


Figure 3.3. Coaxial cylindrical model.

presented algorithm since the analytical solution of the ionized field in this geometry is available. The inner and outer conductor radii are $r_0 = 0.0025$ m and $R = 4$ m, respectively. The applied voltage is $V_0 = 300$ kV with the outer conductor being grounded, and

the onset field, as determined by Peek's law, is $E_c = 48.06$ kV/cm. The problem is solved using only Schemes I and II since the performance of the other two schemes is reflected by Scheme II.

Figure 3.4 shows the finite element mesh which is formed in the following manner. The solution domain is first subdivided with a number of annuli and then each annulus is further subdivided with the same number of triangular elements.

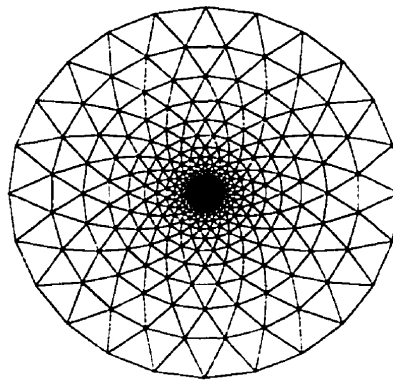


Figure 3.4. FE mesh for the coaxial cylindrical model.

The initial values $\{q\}^{(0)} = \{q_1^{(0)}, q_2^{(0)}, \dots, q_{n_p}^{(0)}\}^T$ are chosen as

$$q_i^{(0)} = \begin{cases} 1, & \text{if } i \in I(\Gamma_c) \\ \tau, & \text{otherwise} \end{cases} \quad (3.18)$$

where τ is a constant and its value can be chosen between 0 and 1 or larger. The initial values $\{u\}^{(0)} = \{u_1^{(0)}, u_2^{(0)}, \dots, u_{n_p}^{(0)}\}^T$ are determined from $\{q\}^{(0)}$ by solving Poisson's equation.

Scheme II is applied to solve the ionized field under the boundary conditions BC1 and BC2(b) with different initial values. The performance of the iterative algorithm is shown in Fig. 3.5, in which the flat part of the curve indicates that the convergence has been

obtained. It is obvious, from Fig. 3.5, that the iterative process converges fast and the rate of convergence is not sensitive to the choice of the initial values. Actually, the number of

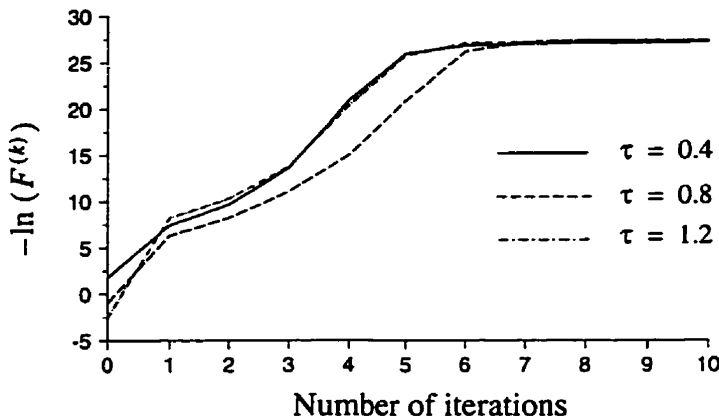


Figure 3.5. Iterative behaviour of the algorithm for different initial values — Scheme II; $n_p = 792$.

iterations for convergence is less than 10 for different voltage levels and geometric parameters. When Scheme I is applied to solve the problem (boundary conditions BC1 and BC2(a)), similar conclusions are reached. It is worth mentioning that as soon as the objective function F converges to its minimum value (near zero) the variables converge to the same set of values (the solution of the problem) although the iteration starts from different initial values.

Figure 3.6 shows the comparison between the analytical solutions and the numerical values for u and q along a radius in the case when Scheme II is employed with $n_p = 792$.

The errors in u and q along a radial direction, obtained by using Scheme I for different numbers of nodes are shown in Figs. 3.7 and 3.8. Figures 3.9 and 3.10 show the errors in u and q along a radius, obtained by using Scheme II as the number of nodes is varied. Figure 3.11 shows the dependence of the errors in electric field strength E at the outer conductor surface on the number of nodes n_p . Examination of the above figures shows that the accu-

racy of the solution for the electric potential is higher than that of the charge density (by about one order of magnitude), while the accuracy of the solution for the electric field at

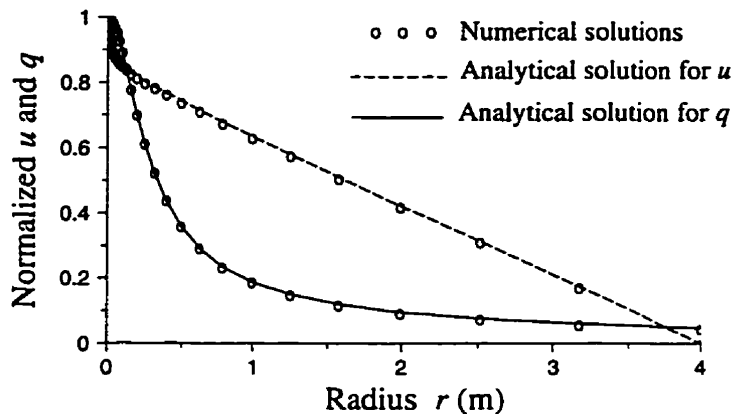


Figure 3.6. Normalized solutions for u and q along a radial direction — Scheme II; $n_p = 792$.

the outer conductor (grounded conductor) lies in between. The accuracy of the charge density solution near the inner conductor, obtained using Scheme I, is relatively poor, but a better accuracy is obtained near the grounded conductor. This is a desirable result because interest is focused on the field at the ground level in practical ionized field analysis. With increasing the number of nodes in the finite element mesh, the accuracy of the numerical solution improves, but the number of iterations required for convergence is not significantly affected. This is seen from Figs. 3.7-3.12.

The dependence of the CPU time in seconds per iteration on the number of nodes (on a SPARCstation 5, with Fortran 77 coding) is shown in Fig. 3.13. The CPU time increases almost linearly with the number of nodes. A noteworthy feature of the method is that the total CPU time required is of the order of minutes even when a mesh with a large number of nodes is employed. For example, when $n_p = 792$, each iteration requires 8 seconds; only 6 iterations are required for convergence and the total CPU time is 48 seconds.

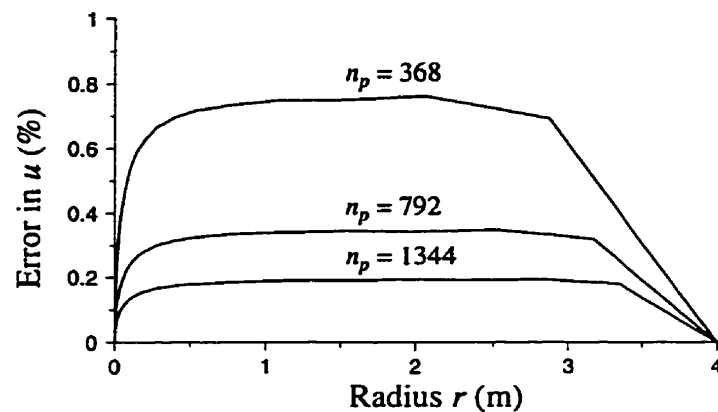


Figure 3.7. Percent error in u for different n_p — Scheme I.

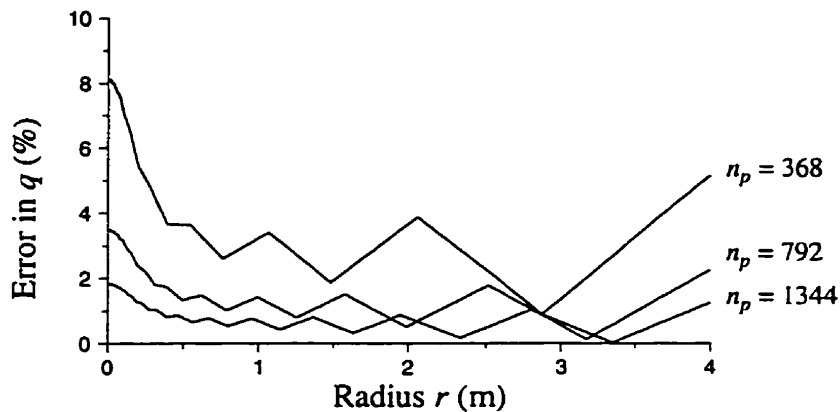


Figure 3.8. Percent error in q for different n_p — Scheme I.

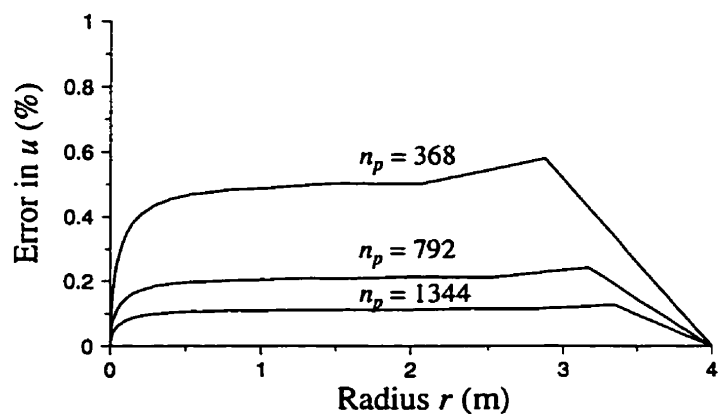


Figure 3.9. Percent error in u for different n_p — Scheme II.

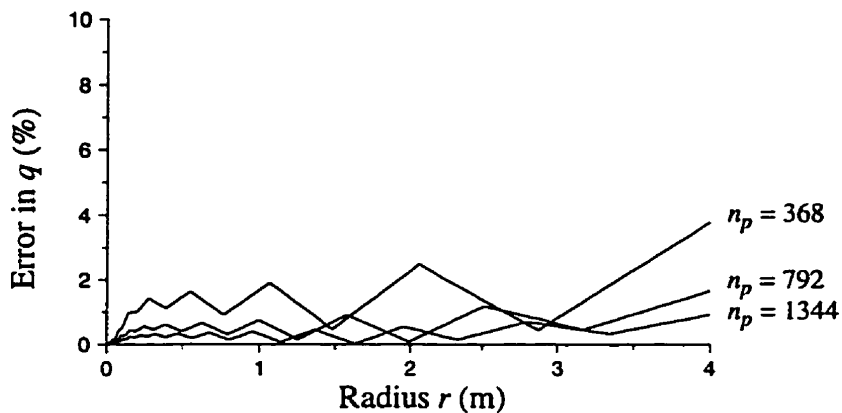


Figure 3.10. Percent error in q for different n_p — Scheme II.

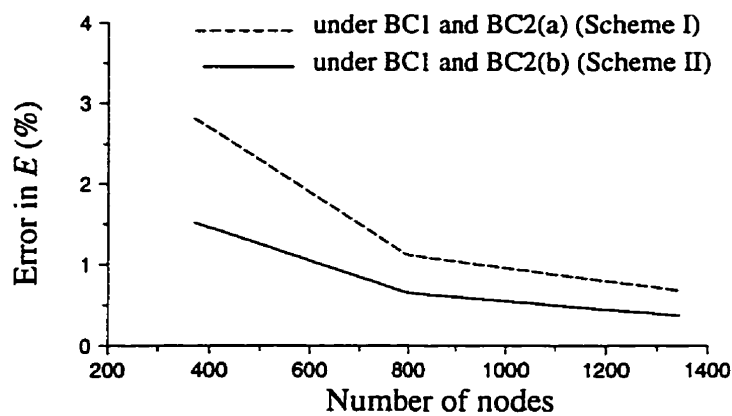


Figure 3.11. Percent error in the electric field strength E at the grounded conductor surface versus n_p — Schemes I and II.

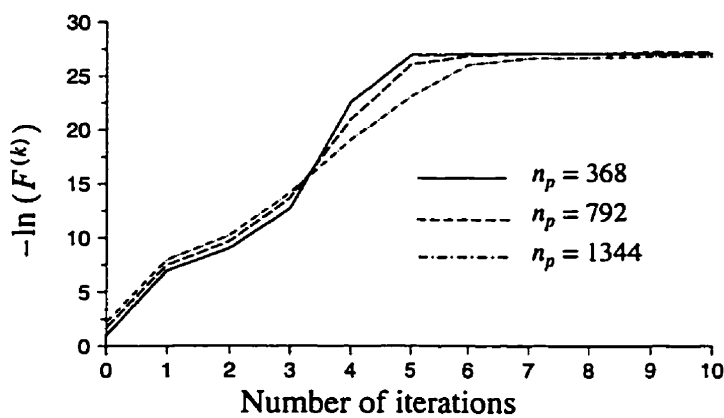


Figure 3.12. Iterative behaviour of the algorithm for different n_p — Scheme II; $\tau = 0.4$.

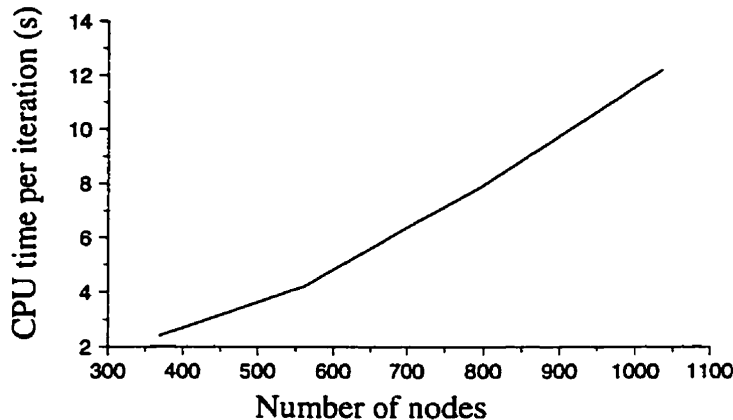


Figure 3.13. CPU time versus the number of nodes.

§3.6 Numerical Tests on a Line-Plane Model in Still Air

The line-plane model is shown in Fig. 3.14. The artificial boundary (dashed line) is located at a distance $5H$ above and $7H$ laterally away from the conductor, where H is the conductor height above the ground level. The conductor radius is $r_0 = 0.0025$ m and the

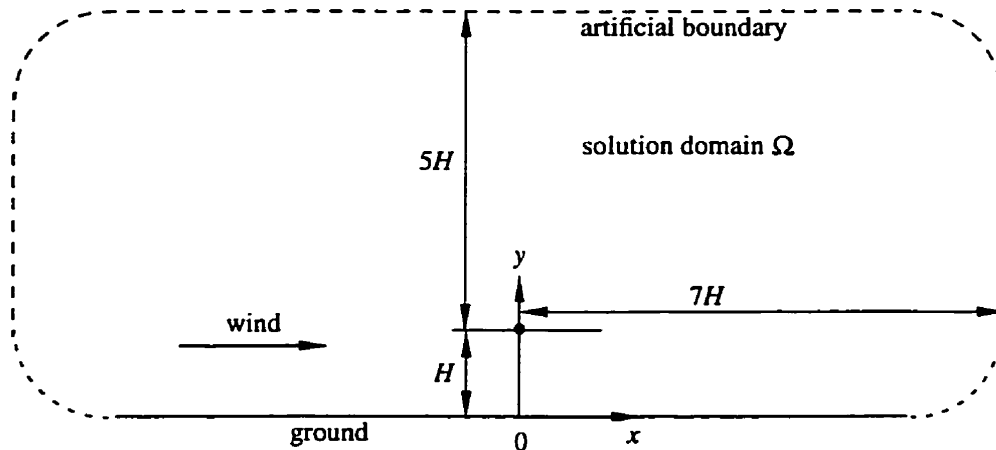


Figure 3.14. Line-plane model.

conductor height $H = 2$ m. The onset electric field strength is $E_c = 48.06$ kV/cm as obtained by application of Peek's law. The potential at the artificial boundary is determined from the charge-free field [22]. There is no analytical solution for this geometry,

but measurement data [23] are available at several voltage levels ($V_0 = 120, 200, 300$ kV) for the chosen geometry.

The triangular mesh of the solution domain, as shown in Fig. 3.15, is generated using an automatic mesh generation program [45]. In this mesh $n_p = 1291$ and $n_e = 2476$.

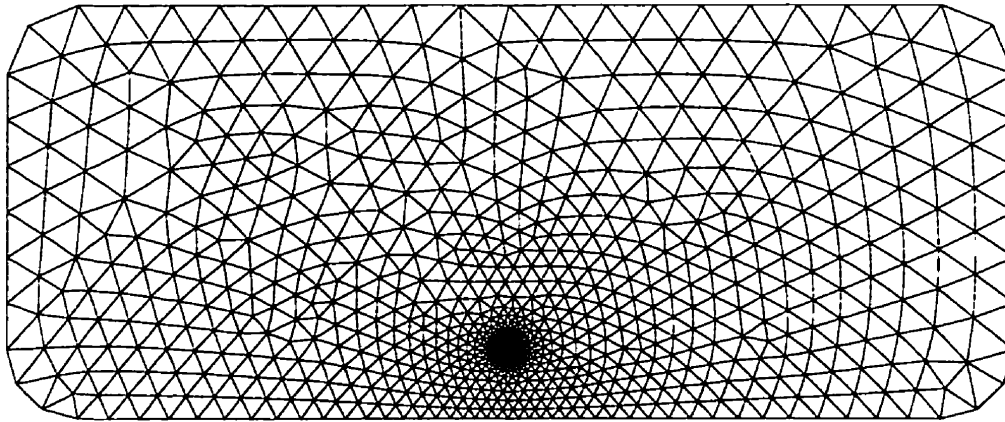


Figure 3.15. FE mesh for the line-plane model; $n_p = 1291$.

As discussed in [55], the initial values for the problem in still air can be chosen using Eq. (3.18), but it is not quite satisfactory in the case of Scheme I when the applied voltage is over 150 kV. Therefore, the ionized field of a coaxial cylindrical geometry with $R_{eq} = 2H$ is used to specify the initial values as follows. Denoting the distribution of q for the coaxial cylindrical model at a distance r from the axis by $\tilde{q}(r)$, the initial values

$$\{q\}^{(0)} = \{q_1^{(0)}, q_2^{(0)}, \dots, q_{n_p}^{(0)}\}^T \text{ are given by}$$

$$q_i^{(0)} = \tilde{q}(r_i), \quad i = 1, 2, \dots, n_p$$

where r_i is the distance of the point (x_i, y_i) (location of the node i) away from the axis of the conductor, i.e.

$$r_i = \sqrt{x_i^2 + (H - y_i)^2}$$

The initial values $\{u\}^{(0)} = \{u_1^{(0)}, u_2^{(0)}, \dots, u_{n_p}^{(0)}\}^T$ are then obtained by solving Poisson's equation based on the initial values $\{q_1^{(0)}, q_2^{(0)}, \dots, q_{n_p}^{(0)}\}$.

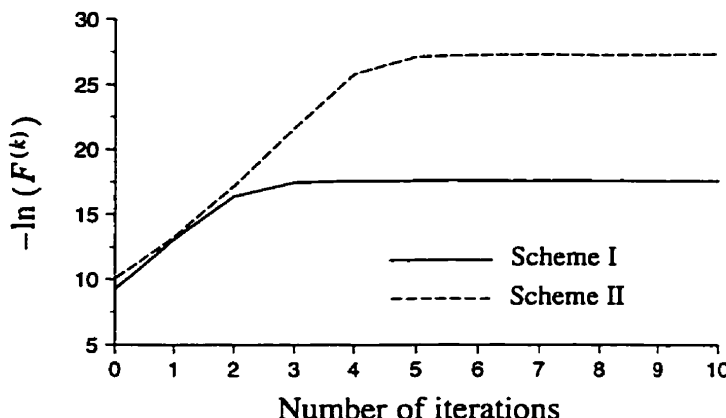


Figure 3.16. Iterative behaviour of Schemes I and II; $V_0 = 200$ kV; $R_{eq} = 4$ m.

Figure 3.16 shows the iterative behaviour of Schemes I and II at the voltage level $V_0 = 200$ kV. In the case of Scheme II, the boundary values of q are chosen to be equal to those of a coaxial cylindrical geometry with $R_{eq} = 2H$. It is seen that the iterative process of Schemes I and II is stable and converges fast. Less than 10 iterations are required for convergence. The same thing is also true for other voltage levels.

Figures 3.17 and 3.18 show the calculated profiles of electric field strength and charge density, respectively, at the voltage levels: $V_0 = 120, 200, 300$ kV. The results of Figs. 3.17 and 3.18 are obtained by application of Scheme I and III. Both Schemes employ the boundary condition BC2(a) which is determined from Kaptzov's assumption (see Chapter 2). The profiles obtained by the two schemes practically coincide with each other and agree satisfactorily with the available experimental results [23], as shown in Fig. 3.19.

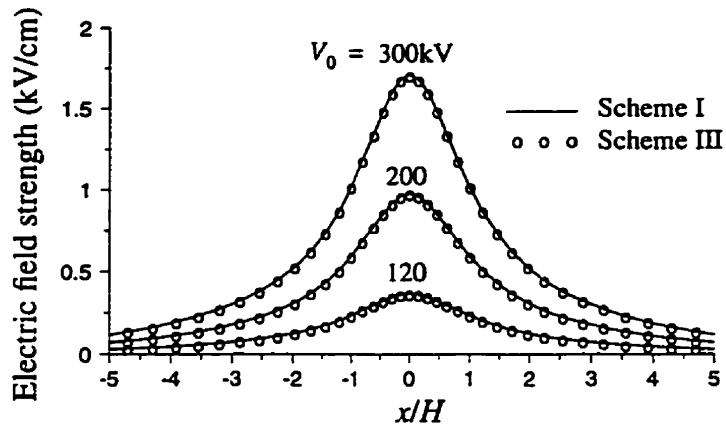


Figure 3.17. Ground profiles of electric field strength for different voltage levels.

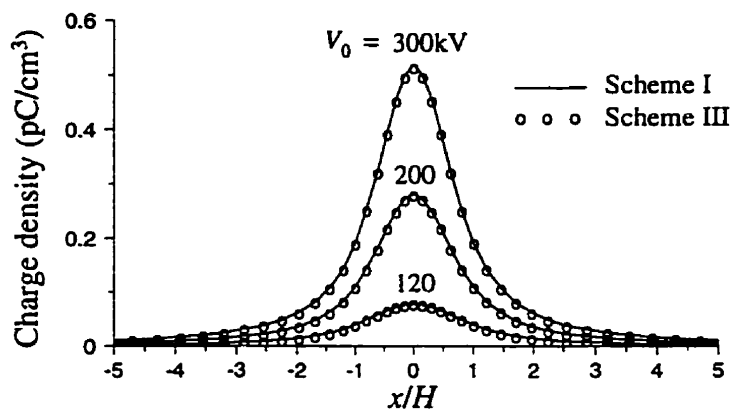


Figure 3.18. Ground profiles of space charge density for different voltage levels.

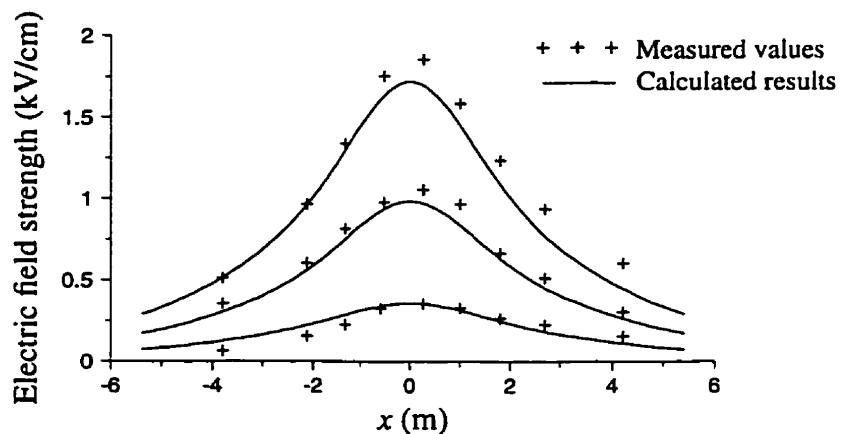


Figure 3.19. Comparison between the calculated ground profiles of electric field strength and the measured values [23] in still air ($w < 1 \text{ m/s}$).

Less than 10 iterations are required for convergence in all these cases. Each iteration requires 22.6 seconds of CPU time (SPARCstation 5, Fortran 77 coding), and the total CPU time for each application of Scheme I or II is less than 226 seconds. Each application of Scheme III needs to implement Scheme II four times and therefore requires 904 seconds

§3.7 Numerical Tests on a Line-Plane Model under Wind Conditions

Scheme I is applied to solve the ionized field, at a voltage level $V_0 = 300$ kV, in the presence of wind. The electric field strength at the conductor surface is specified to be the corona onset value $E_c = 48.06$ kV/cm, as before, and is assumed to remain unchanged in the presence of wind. Three different wind velocities: $w = 0, 4$, and 8 m/s are considered. The initial values are chosen as discussed in Section 3.6. Less than 10 iterations are required to obtain convergence even with the wind velocity $w = 8$ m/s. The CPU time for each iteration is almost the same as that required in the case of still air.

The ground level profiles of electric field strength and space charge density are shown in Figs. 3.20 and 3.21, respectively. Figure 3.22 shows a favourable comparison between the calculated ground level electric field profile and the experimental values [23] at a wind velocity 8 m/s. It is observed, from Figs. 3.20 and 3.21, that the amplitude of the electric field strength and the charge density increases only slightly with the wind velocity. The distortion of the profiles of charge density due to wind is more significant.

It should be mentioned that as the wind velocity increases, the ion flow in the low field region becomes more influenced by wind. As a result, a region without space charge is created on the upwind side of the line, while a region with more space charge is created on

the downwind side. Numerical tests show that the convergence of $\{u\}$ and $\{q\}$ to their solutions is easily achieved when the wind velocity lies in the range of 0-8 m/s for the geometry considered. If the wind velocity is larger than 8 m/s, the convergence is not quite as satisfactory. At a lower voltage level (e.g. $V_0 = 200$ kV), the maximum wind velocity which can be handled is less than 8 m/s.

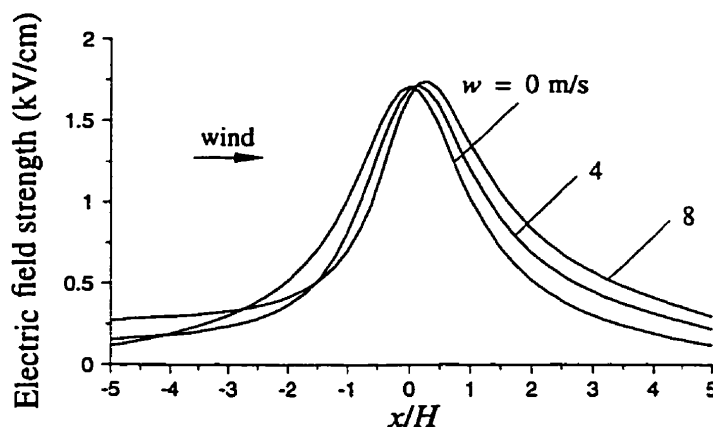


Figure 3.20. Ground profiles of electric field strength for different wind velocities.

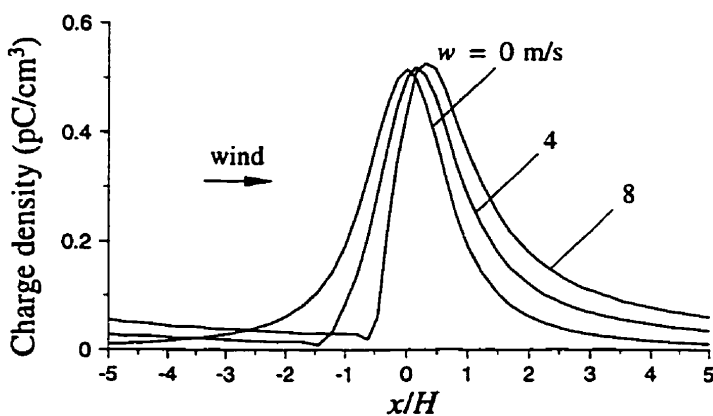


Figure 3.21. Ground profiles of space charge density for different wind velocities.

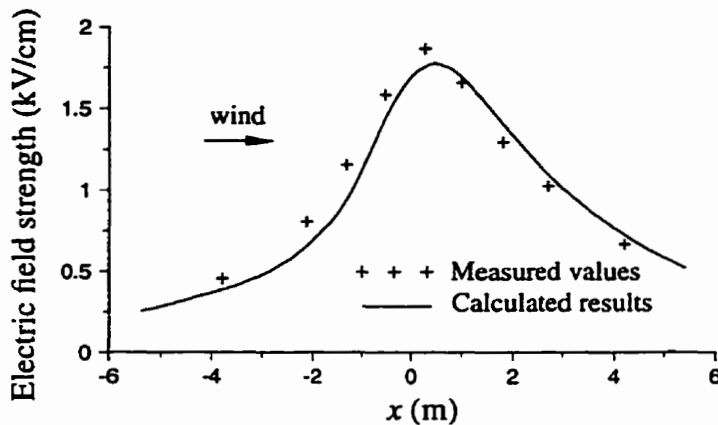


Figure 3.22. Comparison between the calculated ground level profile of electric field strength and the measured values [23] under wind condition ($w = 8 \text{ m/s}$).

§3.8 Summary

The techniques of applying the modified Gaussian algorithm have been presented. The sparse structure of the matrices involved is incorporated to economize the solution cost. Several alternative practical schemes of applying the modified Gaussian algorithm have been presented, which provide considerable convenience when treating the different boundary conditions at the conductor surface. The choice of the initial values for the iterative process has been discussed in detail.

It is shown that the computer memory requirements and CPU time are mainly due to forming and solving Eq. (3.4) in order to find the direction of correction. When the *LU* factorization method is employed to solve this equation, the storage required is of order $O(2m_T n_p)$ and the number of arithmetic operations required is of order $O(m_T^2 n_p)$ or $O(16m_K^2 n_p)$ for each iteration.

Numerical tests have been carried out on a coaxial cylindrical model, for which an

analytical solution is available, to demonstrate the validity of the new method. The method has also been applied to a line-plane configuration in the absence and presence of wind. The following facts can be observed from the numerical results.

Practically coincident solutions are obtained by using different approaches such as Schemes I and III.

The presented algorithm is highly efficient in terms of the rate of convergence and the CPU time. For example, the number of iterations for an iterative process to converge in all the cases presented in this chapter is less than 10 and the total CPU time is of the order of minutes.

It is shown that a numerical solution with good accuracy can be achieved using a finite element mesh with sufficient elements or nodes. The ground level profiles of electric field strength calculated for different voltage levels agree satisfactorily with the experimental results available in the literature [23].

Under wind conditions, the choice of initial values may be critical. A method for specifying the initial values is suggested in Section 3.6. A different method is discussed in [55]. For the configuration considered, good convergence is obtained at a voltage level $V_0 = 300$ kV for a wind velocity up to 8 m/s.

CHAPTER 4

UPWIND FVM BASED RELAXATION ALGORITHM

This chapter presents a highly stable relaxation iterative algorithm for solving the ionized field associated with unipolar DC lines in still air and in the presence of wind. For implementing the iterative algorithm, two new upwind finite volume methods (FVM) are proposed for the solution of the current continuity equation. Depending on which FVM is employed, the iterative algorithm is called the node-centered FVM based relaxation algorithm or the triangular FVM based relaxation algorithm. Numerical results are carried out on the coaxial cylindrical model and the line-plane model with the electric field strength at the conductor surface being taken as a boundary condition for both models. The wind velocity considered is up to 45m/s.

This relaxation algorithm can also be used to solve the ionized field problem in which the space charge density at the conductor surface is taken as a boundary condition. Numerical results in this case, however, will not be presented since they are similar to those in the case when the former boundary condition is used.

§4.1 Equations and Boundary Conditions

Poisson's equation and the current continuity equation described in Chapter 2 are restated as follows:

$$\nabla^2 u = -\rho/\epsilon_0 \quad (4.1)$$

$$\nabla \cdot (\rho v) = 0 \quad (4.2)$$

with

$$v = -k\nabla u + w \quad (4.3)$$

where v is the space charge drift velocity, k the ionic mobility and w the wind velocity.

The boundary conditions used in this chapter include

$$u = \begin{cases} V_0, & (x, y) \in \Gamma_c \\ 0, & (x, y) \in \Gamma_g \\ \Phi(x, y), & (x, y) \in \Gamma_a \end{cases} \quad (4.4)$$

$$\partial u / \partial n = E_c, \quad (x, y) \in \Gamma_c \quad (4.5)$$

$$\rho = 0, \quad (x, y) \in \Gamma_{\rho} \quad (4.6)$$

The boundary conditions (4.4) and (4.5) are the same as Eqs. (2.11) and (2.12), respectively. The boundary condition (4.6) is required only in the presence of strong wind, with the boundary Γ_{ρ} being a portion of the artificial boundary which is defined such that

$v_n = (-k\nabla u + w) \cdot n < 0$ on Γ_{ρ} , where n is the outward normal on the boundary. The physical meaning of this condition is that the space charge flowing into the solution domain through the boundary Γ_{ρ} is negligible. It should be pointed out that this boundary can only be determined during the iterative process from the current calculated distributions of u and ρ .

§4.2 Iterative Algorithm

4.2.1 Preliminary Considerations

The algorithm proposed in this chapter is constructed by considering the electric potential

u to consist of two components. The first component, Φ , is due to the applied voltage when no space charge is present and is the solution of the following boundary value problem:

$$\begin{cases} \nabla^2 \Phi = 0 \\ \Phi|_{\Gamma_c} = V_0 \\ \Phi|_{\Gamma_s} = 0 \end{cases} \quad (4.7)$$

This problem can be solved either numerically or analytically in the case of a unipolar HVDC transmission line. The other component, φ , is caused by the space charge, and satisfies the Poisson equation with a homogeneous Dirichlet boundary condition,

$$\begin{cases} \nabla^2 \varphi = -\rho/\epsilon_0, & \text{in } \Omega \\ \varphi|_{\Gamma} = 0 \end{cases} \quad (4.8)$$

This boundary value problem can be uniquely solved if the charge distribution is known. Obviously, if φ^* is a solution for the problem corresponding to ρ^* , then $\alpha\varphi^*$ is a solution corresponding to $\alpha\rho^*$, where α is an arbitrary constant.

Thus the electric potential u corresponding to a space charge density

$$\rho = \alpha\rho^* \quad (4.9)$$

can be written as

$$u = \Phi + \alpha\varphi^* \quad (4.10)$$

u and ρ in Eqs. (4.9) and (4.10) satisfy Poisson's equation (4.1) and the boundary condition (4.4) for any constant α . To also satisfy the boundary condition (4.5), α is determined as

$$\alpha = (E_c - E_{\Phi c}) / E_{\varphi c} \quad (4.11)$$

where E_c is the corona onset field strength, $E_{\Phi c}$ the electric field strength at Γ_c due to Φ , and $E_{\varphi c}$ the electric field strength at Γ_c due to φ^* . The electric potential and the space charge density must also satisfy the current continuity equation (4.2). This is achieved by modifying iteratively the charge density and the potential. The process consists in calculating a new distribution of charge density from the current continuity equation using the potential given by Eq. (4.10). Subsequently a new distribution of potential is obtained from Eq. (4.8), which leads to a new potential in Eq. (4.10) with α from Eq. (4.11). This is repeated until convergence is reached.

4.2.2 Relaxation Iterative Algorithm

Based on the above discussion, the relaxation iterative algorithm takes the following form:

Step (1): Solve the boundary value problem (4.7) to obtain the potential Φ ; set $k = 1$,

$u^{(k)} = \Phi$ and $\rho_c^{(k)} = \rho_c^{(0)}$, where $\rho_c^{(k)}$ is the space charge density at Γ_c and $\rho_c^{(0)}$ an initial guess for the space charge density at Γ_c .

Step (2): Let $\rho^{(k)} = \rho_c^{(k)}$ at Γ_c and $\rho^{(k)} = 0$ at Γ_{up} ; obtain $\rho^{(k)}$ by solving the current continuity equation (4.2) based on the given distribution $u^{(k)}$.

Step (3): Solve the boundary value problem (4.8) for $\varphi^{(k)}$ using $\rho^{(k)}$; calculate $E_{\varphi c}^{(k)}$.

Step (4): Calculate $\alpha_k = (E_c - E_{\Phi c}) / E_{\varphi c}^{(k)}$; if $|1 - \alpha_k| < \delta$ where δ is a specified tolerance, terminate the iteration; otherwise proceed to step (5).

Step (5): Update the potential in the entire solution domain and the charge density at Γ_c , respectively, as:

$$u^{(k+1)} = \Phi + \alpha_k \varphi^{(k)} \quad (4.12)$$

$$\rho_c^{(k+1)} = \alpha_k \rho_c^{(k)} \quad (4.13)$$

Step (6): Perform the relaxation procedure:

$$u^{(k+1)} = u^{(k)} + \theta_1 (u^{(k+1)} - u^{(k)}) \quad (4.14)$$

$$\rho_c^{(k+1)} = \rho_c^{(k)} + \theta_2 (\rho_c^{(k+1)} - \rho_c^{(k)}) \quad (4.15)$$

In this chapter, we present results for $\theta_1 = \theta_2 = \theta$.

Step (7): Set $k \leftarrow k + 1$ and repeat the iterative process from step (2).

The parameter α_k is used to update the quantities in the k th iteration, and also serves as a measure of convergence. The relaxation factor θ is chosen in the range $0 < \theta < 1$. The solutions of Poisson's equation and the current continuity equation in steps (2) and (3) are described in the next two sections. The initial value $\rho_c^{(0)}$ for $\rho_c^{(k)}$ may be arbitrarily specified. In this chapter for example, $\rho_c^{(0)}$ is taken to be the space charge density at the conductor surface of the equivalent coaxial cylindrical model with radius $R_{eq} = 2H$ (see Section 2.6).

This algorithm can also be used to solve the ionized field problem in which the space charge density at the conductor surface is specified as a boundary condition (see Section 2.1) by simply setting $\rho_c^{(k)} = \rho_c$ and $\alpha_k = 1$ for $k = 1, 2, 3, \dots$ where ρ_c is a specified charge density at the conductor surface, and taking the change in u or ρ as a measure of convergence instead.

§4.3 FEM for Poisson's Equation

The general form of Eqs. (4.7) and (4.8) is

$$\begin{cases} \nabla^2 U = -q, & \text{in } \Omega \\ U|_{\Gamma} = f_0 \end{cases} \quad (4.16)$$

where the potential U is unknown, q a given function, and f_0 a specified distribution on Γ . Following the same procedure as in Section 2.2, we have

$$[K] \{U\} - [P] \{q\} - [Z] \{g\} = \{0\} \quad (4.17)$$

where the matrices $[K]$, $[P]$ and $[Z]$ are the same as defined by Eqs.(2.21)-(2.24),

$\{U\} = \{U_1, U_2, \dots, U_{n_p}\}^T$ is the vector of nodal values of U ,

$\{q\} = \{q_1, q_2, \dots, q_{n_p}\}^T$ the vector of nodal values of q , and the vector $\{g\}$ follows a

similar notation as in Section 2.2, i.e. its elements are defined such that $g_i = \partial U / \partial n|_i$ if $i \in I(\Gamma)$ and $g_i = 0$ if $i \notin I(\Gamma)$.

Considering that the space charge density distribution has been given at this point, the system of equations (4.17) can be written as

$$[K] \{U\} = \{b\} \quad (4.18)$$

where $\{b\}$ is a vector whose elements are determined as

$$b_i = \sum_j P_{ij} q_j + Z_i g_i \quad (4.19)$$

The system of equations (4.18) can be uniquely solved after the boundary condition (4.4) is imposed. The treatment of the boundary condition may be carried out by simply replacing the i th equation of the system of equations (4.18) with $U_i = f_0(x_i, y_i)$ for $i \in I(\Gamma)$ and by eliminating the unknowns U_i , $i \in I(\Gamma)$ from other equations. The mod-

ified system of equations is written as

$$[\tilde{K}] \{U\} = \{\tilde{b}\} \quad (4.20)$$

with the elements of $[\tilde{K}]$ and $\{\tilde{b}\}$ being given by

$$\tilde{K}_{ij} = \begin{cases} 1, & \text{if } i = j \in I(\Gamma) \\ 0, & \text{if } i \in I(\Gamma) \text{ or } j \in I(\Gamma), i \neq j \\ K_{ij}, & \text{otherwise} \end{cases} \quad (4.21)$$

$$\tilde{b}_i = \begin{cases} f_0(x_i, y_i), & \text{if } i \in I(\Gamma) \\ b_i - \sum_{j \in I(\Gamma)} K_{ij} f_0(x_j, y_j), & \text{otherwise} \end{cases} \quad (4.22)$$

where (x_j, y_j) is the location of the j th node. From Eq. (4.21), it is easily observed that no extra non-zero element is introduced into the matrix $[\tilde{K}]$ and therefore the matrix $[\tilde{K}]$ has a sparse structure similar to that of the matrix $[K]$. In addition, the matrix $[\tilde{K}]$ is a symmetric and positive definite matrix.

The system of equations (4.20) can be easily solved using the *LU* decomposition method, which requires about $0.5m_K^2n_p$ multiplications, where m_K is the average half bandwidth of the matrix $[K]$.

The electric field strength on the conductor surface and ground due to the potential U is obtained by calculating the vector $\{g\}$, which has been described in Section 2.7.

§4.4 FVM for the Current Continuity Equation

In this section, the solution of the current continuity equation (4.2) in step (2) of the iterative algorithm, using two finite volume methods, is discussed, assuming that the electric potential u is given.

4.4.1 Node-Centred Finite Volume Method

The finite volume method starts with a set of control volumes (or cells), which are constructed in the following manner. For an inner node i , the associated control volume C_i is defined by a polygon which is formed by connecting the centres of gravity of all adjacent elements, as shown in Fig. 1(a). At a boundary node i , the construction of the cell is illustrated in Fig. 1(b), where M_{ij} and M_{ik} are the midpoints of the sides \bar{ij} and \bar{ik} , respectively. Denote the common side of cells C_i and C_j by ∂C_{ij} , the set of cells sharing

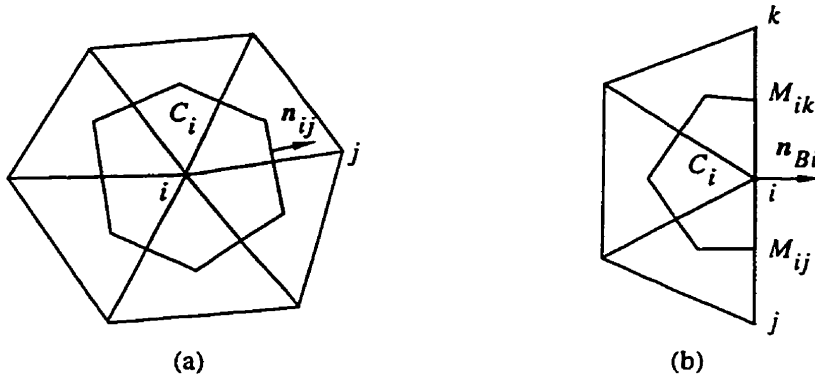


Figure 4.1. Construction of the control volume around an inner node i or a boundary node i .

common sides with the cell C_i by $I_{(i)}^C$, and the boundary of the cell C_i by ∂C_i . The space charge density in each cell C_i is assumed to be a constant which is denoted by ρ_i .

Applying Green's formula, the current continuity equation (4.2) becomes

$$\sum_{j \in I_{(i)}^C} \int_{\partial C_{ij}} \rho_{ij} v \cdot \mathbf{n} ds + \int_{\partial C_i \cap \Gamma} \rho_i v \cdot \mathbf{n} ds = 0, \quad i = 1, 2, \dots, n_p \quad (4.23)$$

Considering the space charge density ρ_{ij} to be constant along the side ∂C_{ij} , we have

$$\sum_{j \in I_{(i)}^C} \rho_{ij} v_{ij} + \rho_i v_{Bi} = 0, \quad i = 1, 2, \dots, n_p \quad (4.24)$$

with v_{ij} and v_{Bi} approximated by

$$\nu_{ij} = \int_{\partial C_{ij}} \mathbf{v} \cdot \mathbf{n} ds = [k(\mathbf{E}_{ij}^{(1)} + \mathbf{E}_{ij}^{(2)})/2 + w] \cdot \int_{\partial C_{ij}} \mathbf{n} ds \quad (4.25)$$

$$\nu_{Bi} = \int_{\partial C_i \cap \Gamma} \mathbf{v} \cdot \mathbf{n} ds = -kL_{Bi}g_i + w \cdot \int_{\partial C_i \cap \Gamma} \mathbf{n} ds \quad (4.26)$$

where $\mathbf{E}_{ij}^{(1)}$ and $\mathbf{E}_{ij}^{(2)}$ are the calculated electric field strengths at the centres of gravity

$G_{ij}^{(1)}$ and $G_{ij}^{(2)}$ of the two elements sharing the side \bar{ij} (see Fig. 4.2), k is the ionic mobil-

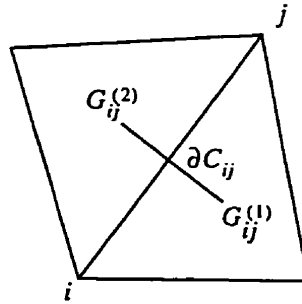


Figure 4.2. Side ∂C_{ij} associated with the centres of gravity of two triangular elements.

ity, L_{Bi} the length of $\partial C_i \cap \Gamma$, and g_i the i th nodal value of $\partial u / \partial n$ which is calculated using the method as indicated in Section 4.3. Here, the density of space charge flowing through the common side ∂C_{ij} is approximated by

$$\rho_{ij} = [\frac{\rho_i + \rho_j}{2} + \gamma_{upw} \frac{\rho_i - \rho_j}{2} sign(\nu_{ij})] \quad (4.27)$$

where $sign(\nu_{ij}) = -1$ if $\nu_{ij} < 0$ and $sign(\nu_{ij}) = 1$ if $\nu_{ij} \geq 0$, and γ_{upw} is an upwind parameter, which determines how the space charge density ρ_{ij} is influenced by the two adjacent cells. The value of γ_{upw} is chosen in the range from 0 to 1. When $\gamma_{upw} = 0$, ρ_{ij} takes the average value of the space charge densities of cells C_i and C_j . If $0 < \gamma_{upw} < 1$, it implies that ρ_{ij} is more influenced by the space charge density on the upwind side. If $\gamma_{upw} = 1$, ρ_{ij} on the side ∂C_{ij} takes the value of the space charge density on its upwind

side, which physically means that the space charge density of the cell C_i is only influenced by the space charge densities on its upwind side. Substitution of Eq. (4.27) in (4.24) yields the system of equations

$$[A] \{ \rho \} = \{ 0 \} \quad (4.28)$$

where $[A]$ is an $n_p \times n_p$ matrix with its elements defined as

$$A_{ij} = \begin{cases} \sum_{s \in I_{(i)}^C} \frac{1}{2} [1 + \gamma_{upw} \text{sign}(v_{is})] v_{is} + v_{Bi}, & \text{for the diagonal entries} \\ \frac{1}{2} [1 - \gamma_{upw} \text{sign}(v_{ij})] v_{ij}, & \text{for } j \in I_{(i)}^C \\ 0, & \text{otherwise} \end{cases} \quad (4.29)$$

The above system of equations is solved using the Gaussian elimination method after the space charge densities of cells adjacent to $\Gamma_c \cup \Gamma_{up}$ are specified as indicated in step (6) of the iterative algorithm in Section 4.2. The non-symmetric sparse matrix $[A]$ is stored in a two dimensional array of dimensions $n_p \times 2m_{Am}$, where m_{Am} is the maximum half bandwidth of the matrix $[A]$. Since a control volume is uniquely associated with a node, m_{Am} is identically equal to the maximum half bandwidth of the matrix $[K]$. The number of multiplications required for the solution is about $m_{Am}^2 n_p$. This number is about twice that for the solution of Eq. (4.20) if the finite element mesh for the unipolar line model is properly numbered. Therefore, the total computational effort required for each iteration in the associated iterative algorithm is about three times that for the solution of the discretized Poisson's equation.

4.4.2 Triangular Finite Volume Method

In the triangular FVM, each triangular element is taken as a cell. In addition, each boundary segment is defined as a special type of cell, called “segment cell”, which serves as the source or sink of stream lines. The segment cells are numbered with $n_e + 1, n_e + 2, \dots, n_{cell}$, where n_e is the number of elements. Following a similar discretization procedure as in the previous section, we obtain a linear system of equations

$$[A] \{ \rho \} = \{ 0 \} \quad (4.30)$$

where $[A]$ is an $n_e \times n_{cell}$ matrix and its elements are defined as

$$A_{ij} = \begin{cases} \sum_{s \in I_{(i)}^C} \frac{1}{2} [1 + \gamma_{upw} sign(v_{is})] v_{is}, & \text{for the diagonal entries} \\ \frac{1}{2} [1 - \gamma_{upw} sign(v_{ij})] v_{ij}, & \text{for } j \in I_{(i)}^C \\ 0, & \text{otherwise} \end{cases} \quad (4.31)$$

with

$$v_{ij} = \begin{cases} \left[k \left(\frac{S_{ij} - \bar{s}_{ij}}{S_{ij}} E_{oi} + \frac{\bar{s}_{ij}}{S_{ij}} E_{oj} \right) + w \right] \cdot \int_{\partial C_{ij}} \mathbf{n} ds, & \text{for } j \leq n_e \\ -k L_{ij} (g_l + g_m) + w \cdot \int_{\partial C_{ij}} \mathbf{n} ds, & \text{for } j > n_e \end{cases} \quad (4.32)$$

where E_{oi} and E_{oj} are the calculated field strengths at the centres of gravity O_i and O_j of the two cells C_i and C_j sharing the side ∂C_{ij} (see Fig. 4.3), S_{ij} the length of the segment $\overline{O_i O_j}$, \bar{s}_{ij} the length of the segment $\overline{O_i Q}$, and g_l, g_m are the values of $\partial u / \partial n$ at the two terminal points l and m of the side ∂C_{ij} on the boundary which are calculated using the method presented in Section 2.7.

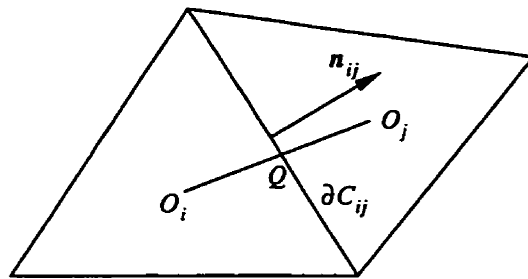


Figure 4.3. Side ∂C_{ij} shared by two cells.

The resulting system of equations, when $\gamma_{upw} = 1$, can be solved in a simple way. As shown in Fig. 4.4, the space charge density ρ_i in the cell C_i is only influenced by one or two cells. If the space charge densities on the upwind side of the cell C_i have been eval-

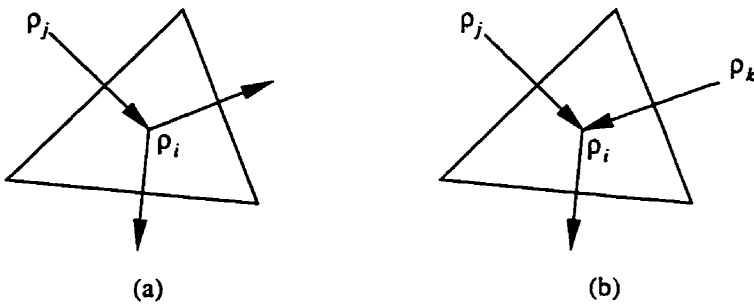


Figure 4.4. Space charge density ρ_i of the cell C_i influenced by cells on its upwind side. (a) ρ_i influenced by one cell; (b) ρ_i influenced by two cells.

ated, the space charge density ρ_i can be easily determined as

$$\rho_i = -\frac{1}{A_{ii}} \sum_{j \in I_{(i)}^{C_{upw}}} A_{ij} \rho_j \quad (4.33)$$

where $I_{(i)}^{C_{upw}} \subset I_{(i)}^C$ is the set of triangular cells on the upwind side of the cell C_i . It is possible to obtain all the cell space charge densities by using Eq. (4.33), starting from the cells whose sides are on $\Gamma_c \cup \Gamma_{up}$ to the cells on the downwind side once the charge densities

of the segment cells on $\Gamma_c \cup \Gamma_{up}$ are evaluated. To do this, first we define a vector $\{n^{uw}\}$ such that $n_i^{uw} + 1$ represents the number of variables to be determined in the i th equation of the system of equations (4.30). The values of the components in $\{n^{uw}\}$ will vary as the solution process proceeds. The initial value of n_i^{uw} is the number of triangular cells in the set $I_{(i)}^{Cupw}$. If the value of n_i^{uw} becomes zero, it indicates that only the quantity p_i in the i th equation is undetermined. The calculation scheme is described as follows:

Step (1): Generate the vector $\{n^{uw}\}$ and set $m = 0$.

Step (2): For $i = 1, 2, \dots, n_e$, if $n_i^{uw} = 0$, carry out the following procedure:

$$p_i = -\frac{1}{A_{ii}} \sum_{j \in I_{(i)}^{Cupw}} A_{ij} p_j$$

$$n_i^{uw} \leftarrow n_i^{uw} - 1$$

$$n_j^{uw} \leftarrow n_j^{uw} - 1 \text{ for all } j \in I_{(i)}^{Cupw}$$

$$m \leftarrow m + 1$$

Step (3): If $m = n_e$, stop; otherwise go to step (2).

Since the average number of cells in the set $I_{(i)}^{Cupw}$ is about 1.5, the total number of multiplications and divisions required in the above scheme is about $2.5n_e$ or $5n_p$ since $n_e \approx 2n_p$ for a triangular element mesh. This number is negligibly small compared to that required by the *LU* decomposition method or the Gaussian elimination method. Thus, the solution of Poisson's equation is responsible for most of the computational work for each iteration in the iterative algorithm.

§4.5 Numerical Tests on the Coaxial Cylindrical Model

The coaxial cylindrical model described in Chapter 3 is employed, but the applied voltage considered for the following tests is $V_0 = 200$ kV. In the corresponding finite element mesh (see Fig. 3.4), the number of nodes is $n_p = 792$ and the number of elements is $n_e = 1536$.

In the following numerical tests, the convergence criterion is taken to be $|1 - \alpha_k| < 1\%$.

Figure 4.5 illustrates the behaviour of the relaxation iterative algorithm when the node-centered FVM is employed. It is seen that the proposed iterative algorithm is stable for different relaxation factors. The iterative behaviour due to the application of the triangular FVM is similar.

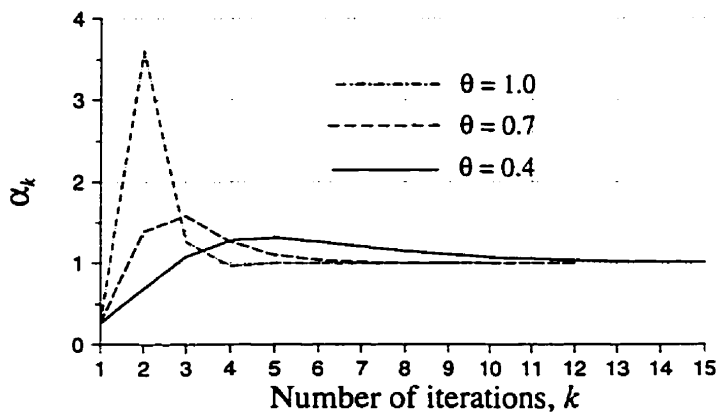


Figure 4.5. Behavior of the iterative algorithm.

The calculated distributions of u and ρ are shown in Fig. 4.6 and compared with the exact solutions for the normalized u and ρ along a radial direction. The errors in u and ρ obtained by using the present algorithm and the FEM based optimization algorithm presented in Chapters 2 and 3 are compared in Figs. 4.7 and 4.8, respectively. It is seen that the error in u generated by the FVM based algorithm is smaller than that by the FEM

based algorithm, but they are of the same order. The error in ρ close to the boundary obtained by using the FEM based algorithm is smaller than that by using the FVM based algorithm; at other locations, the errors due to the FEM based algorithm and the triangular FVM based algorithm are close and larger than the error due to the node-centered FVM based algorithm.

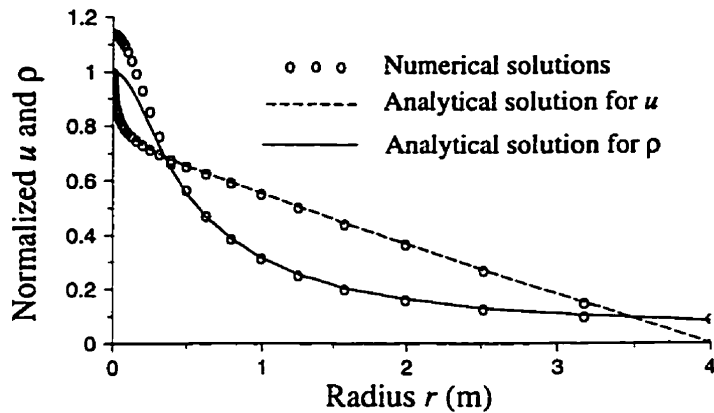


Figure 4.6. Calculated distributions of u and ρ along the radial direction.

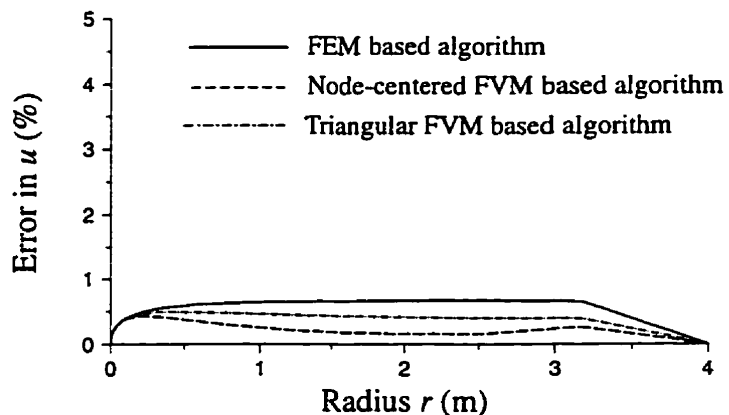


Figure 4.7. Percent error in u obtained by using different algorithms.

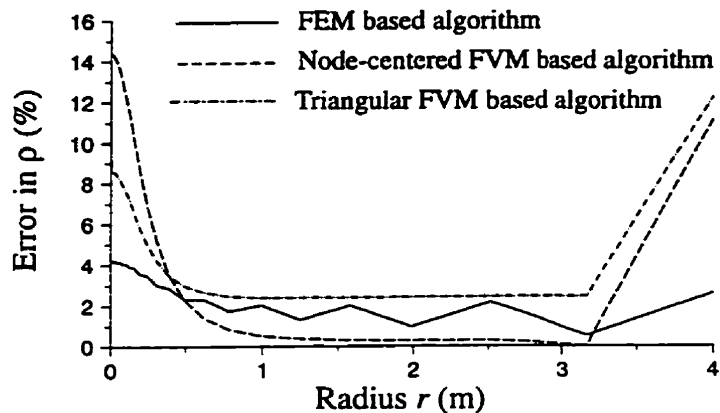


Figure 4.8. Percent error in p obtained by using different algorithms.

The errors in E at the grounded conductor due to different algorithms are very close and are all of the order of 1%. The CPU time (SPARCstation 5, Unix, Fortran 77) required in each iteration of the node-centered FVM based algorithm is 2 seconds, while that of the triangular FVM based algorithm is only 0.8 second. The FEM based optimization algorithm needs more CUP time than the FVM based algorithm, i.e. 11 seconds per iteration.

§4.6 Numerical Tests on the Line-Plane Model

4.6.1 Test Models

The line-plane model described in Chapter 3 (see Fig. 3.14) is employed. The effect of the geometric parameters on the iterative behaviour is examined in two ways. First, the conductor radius r_0 is changed thus enabling examination of the effect of the ratio H/r_0 within a practical range. The effect of the conductor height H on the iterative behaviour is examined by increasing the height H while keeping the ratio H/r_0 constant.

4.6.2 Iterative Behaviour

In this section, numerical tests are carried out on the line-plane model to examine the iter-

ative behaviour of the present algorithm as influenced by several factors. In this case, convergence is also considered to have been obtained when $|1 - \alpha_k| < 1\%$. The number of iterations required for convergence, n_{iter} , is used to characterize the behaviour of the iterative algorithm (i.e. stability and rate of convergence). The results shown in Figs. 4.9–4.18 were obtained by using the node-centered FVM to solve the current continuity equation. It may be remarked that the iterative behaviour remains almost the same when the upwind triangular FVM is applied.

Effect of Relaxation

The effect of relaxation is shown in Fig. 4.9. When relaxation is not employed, the value of α_k oscillates and converges slowly. On the other hand, if relaxation is applied, the iterative performance is drastically improved. In what follows, the behaviour of the iterative process as affected by different factors is discussed.

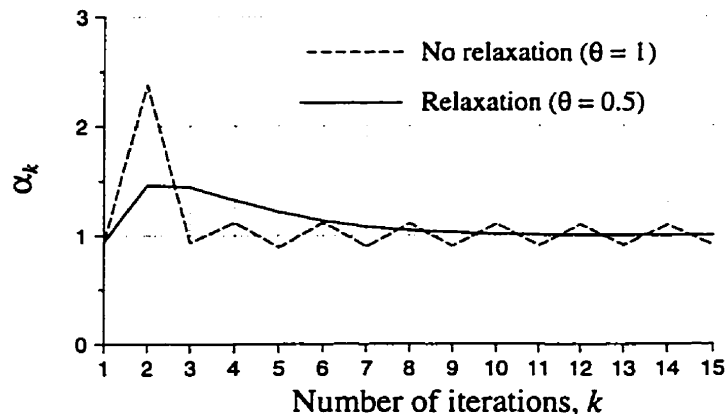


Figure 4.9. Effect of relaxation on the iterative behaviour; $\gamma_{upw} = 1$, $w = 10$ m/s, $r_0 = 0.0025$ m, $H = 2$ m, $V_0/V_c = 2$.

Preliminary numerical investigations showed that when the relaxation factor θ is small, i.e. $\theta < 0.2$, the iterative process converges for any wind velocity, but convergence is slow. Therefore, only values of θ in the range from 0.2 to 1 are considered.

Figure 4.10 shows the dependence of the number of iterations, n_{iter} , required on the relaxation factor θ for different wind velocities. It is seen that for each curve, θ has an optimum value at which n_{iter} reaches its minimum. This optimum point shifts to the right for a larger wind velocity and the corresponding minimum of n_{iter} becomes smaller. To the left of the optimum point, n_{iter} increases slowly as θ is decreased, but on the right, n_{iter} increases drastically with increase in θ . In the case of still air, when $\theta > 0.6$, convergence can not be obtained. The usable range of θ becomes larger as the wind velocity increases. For very strong wind, the iterative process is convergent for any θ between 0.2 and 1.0. It is interesting to note that for $\theta = 1$, convergence can only be obtained for very strong wind.

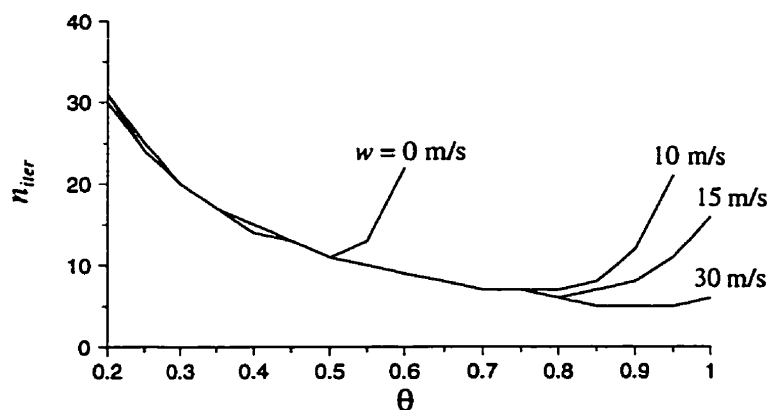


Figure 4.10. Effect of the relaxation factor θ on the number of iterations required for convergence for different wind velocities; $\gamma_{upw} = 1$, $r_0 = 0.0025$ m, $H = 2$ m, $V_0/V_c = 2$.

Since the performance of the present iterative algorithm is better in wind conditions than in still air, further numerical investigations in this section are carried out only under no wind conditions. Figure 4.11 illustrates the influence of the voltage ratio V_0/V_c on n_{iter} . As the voltage ratio V_0/V_c is increased, the optimum value of θ decreases and the usable range of θ becomes smaller.

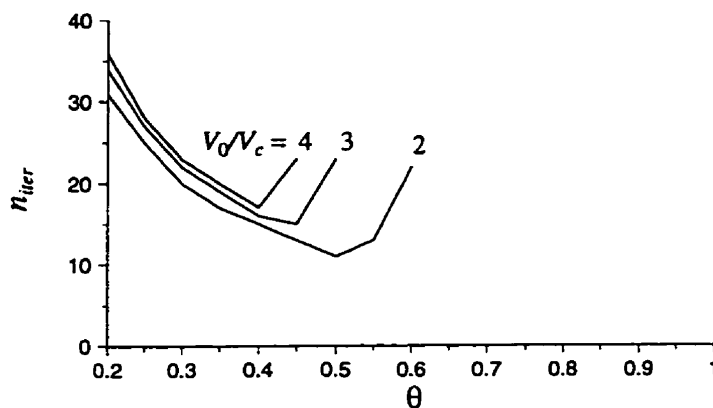


Figure 4.11. Effect of the relaxation factor θ on the number of iterations required for convergence for different values of V_0/V_c ; $\gamma_{upw} = 1$, $w = 0$ m/s, $r_0 = 0.0025$ m, $H = 2$ m.

Figure 4.12 shows that the number of iterations for convergence is almost unaffected by the ratio H/r_0 , and Fig. 4.13 indicates that the conductor height H practically has no effect on the iterative behaviour for a constant value of the ratio H/r_0 .

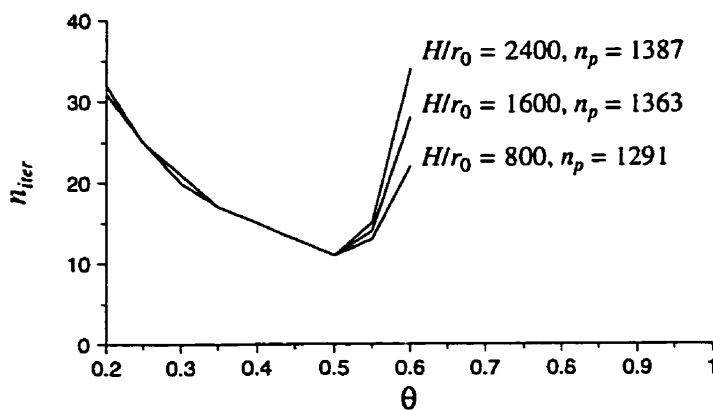


Figure 4.12. Effect of the relaxation factor θ on the number of iterations required for convergence for different values of H/r_0 ; $\gamma_{upw} = 1$, $H = 2$ m, $w = 0$ m/s, $V_0/V_c = 2$.

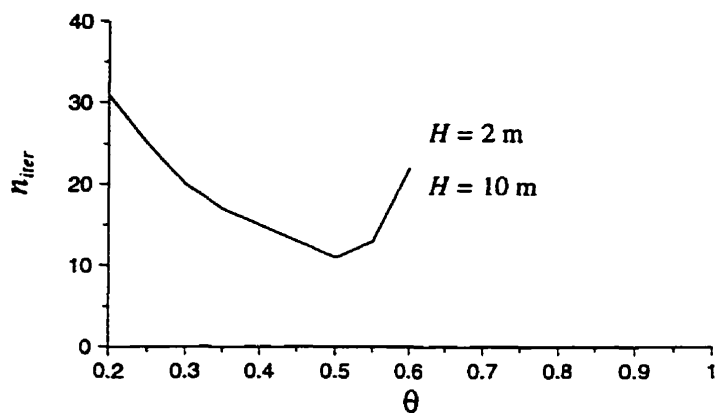


Figure 4.13. Effect of the relaxation factor θ on the number of iterations required for convergence for different values of H ; $\gamma_{upw} = 1$, $H/r_0 = 800$, $w = 0$ m/s, $V_0/V_c = 2$, $n_p = 1291$.

From the above numerical results, it can be concluded that θ should be chosen in the range of 0.2 to 0.5 for light wind, and larger than 0.5 for strong wind. In the case of a very large ratio V_0/V_c (e.g. > 4) and light wind, θ should be chosen in the range of 0.2 to 0.4.

Upwind Effect

Figure 4.14 clearly shows the effectiveness of the upwind algorithm in the presence of

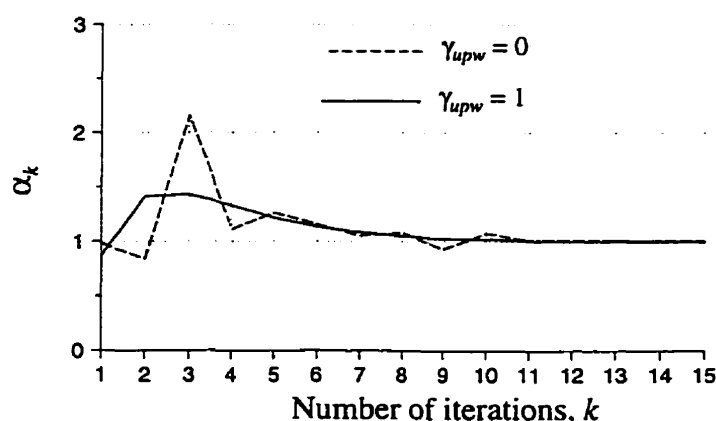


Figure 4.14. Effect of using the upwind algorithm on the iterative behaviour; $w = 9$ m/s, $\theta = 0.5$, $r_0 = 0.0025$ m, $H = 2$ m, $V_0/V_c = 2$.

wind. The necessity of using the upwind algorithm under strong wind conditions can be seen by comparing the results in Fig. 4.15 with those in Fig. 4.10. When $\gamma_{upw} = 0$, as shown in Fig. 4.15, as the wind velocity increases, the usable range of θ becomes smaller and eventually relaxation can not be used to make the iterative process converge; but the opposite is true for the upwind algorithm (see Fig. 4.10).

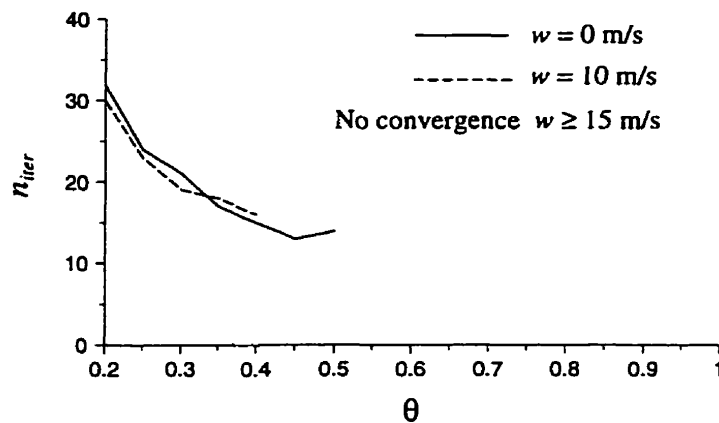


Figure 4.15. Effect of wind velocity on the n_{iter} — θ curve when $\gamma_{upw} = 0$; $r_0 = 0.0025$ m, $H = 2$ m, $V_0/V_c = 2$.

Figure 4.16 illustrates the influence of γ_{upw} in the range from 0 to 1.0 on the required number of iterations at different wind velocities. An interesting fact is observed from this

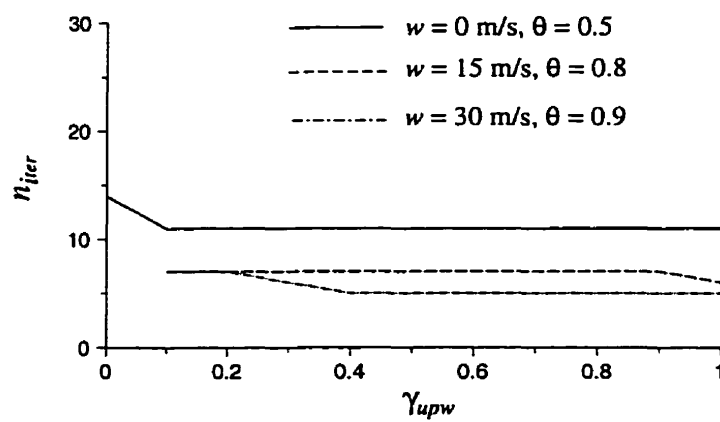


Figure 4.16. Effect of the upwind parameter γ_{upw} on the number of iterations required for convergence for different wind velocities; $r_0 = 0.0025$ m, $H = 2$ m, $V_0/V_c = 2$.

figure, i.e. the variation of γ_{upw} in the range indicated has almost no effect on the convergence rate both in still air and in wind conditions. Also, the effect of γ_{upw} on the calculated results is very small, as shown in Figs. 4.17 and 4.18.

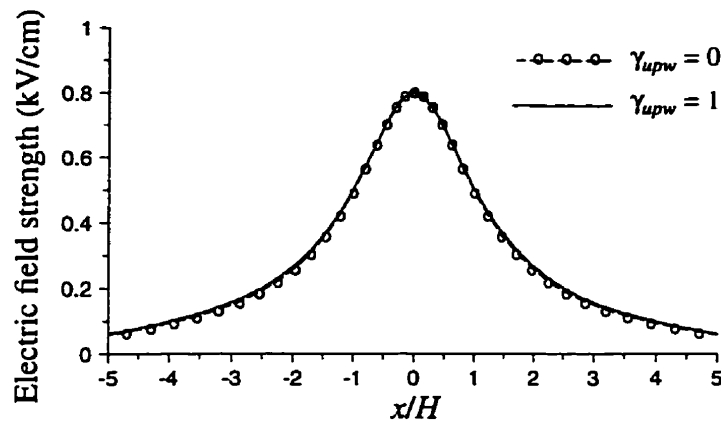


Figure 4.17. Calculated ground profiles of electric field strength in the absence of wind considering the effect of γ_{upw} ; $r_0 = 0.0025$ m, $H = 2$ m, $V_0/V_c = 2$.

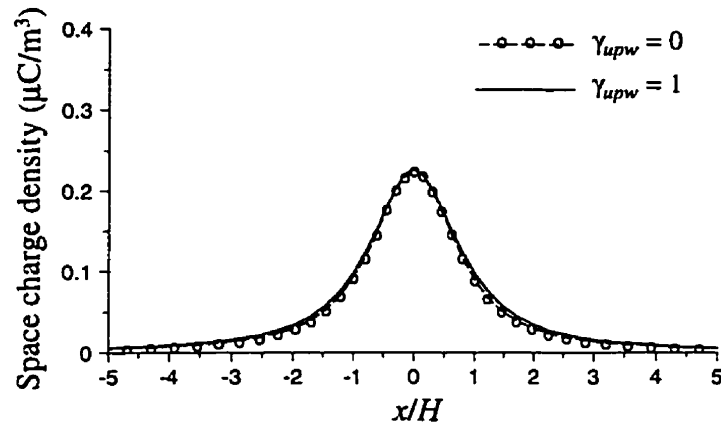


Figure 4.18. Calculated ground profiles of space charge density in the absence of wind considering the effect of γ_{upw} ; $r_0 = 0.0025$ m, $H = 2$ m, $V_0/V_c = 2$.

4.6.3 Ground Profiles of the Field Quantities in Still Air

Figures 4.19 and 4.20 compare the ground profiles of electric field strength and space charge density, respectively, in the absence of wind, obtained by the present algorithm and

the FEM based algorithm presented in Chapters 2 and 3 using the same finite element mesh. The results calculated using the presented algorithm show excellent agreement with those obtained using the FEM based algorithm.

Also, the ground profiles of electric field strength determined by the presented FVM based algorithm show good agreement with those obtained by the BEM [46], and compare favourably with the measured values [23], as shown in Fig. 4.21.

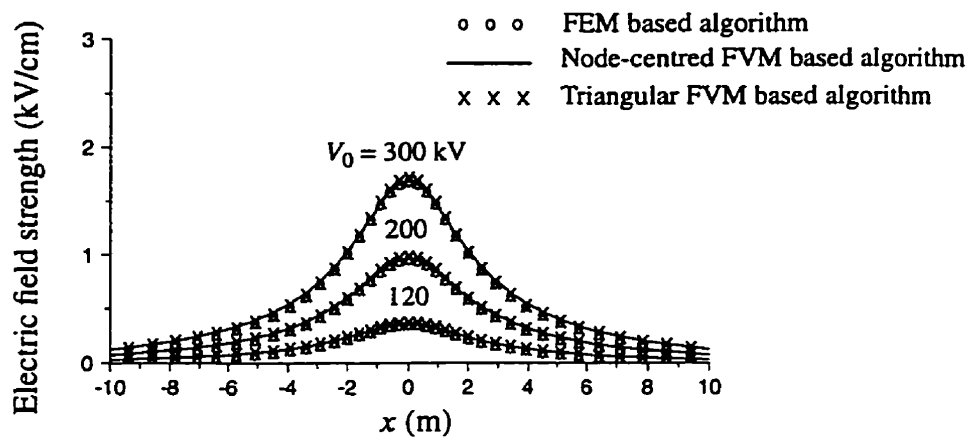


Figure 4.19. Comparison of the ground profiles of electric field strength obtained by different algorithms in the absence of wind; $r_0 = 0.0025 \text{ m}$, $H = 2 \text{ m}$.

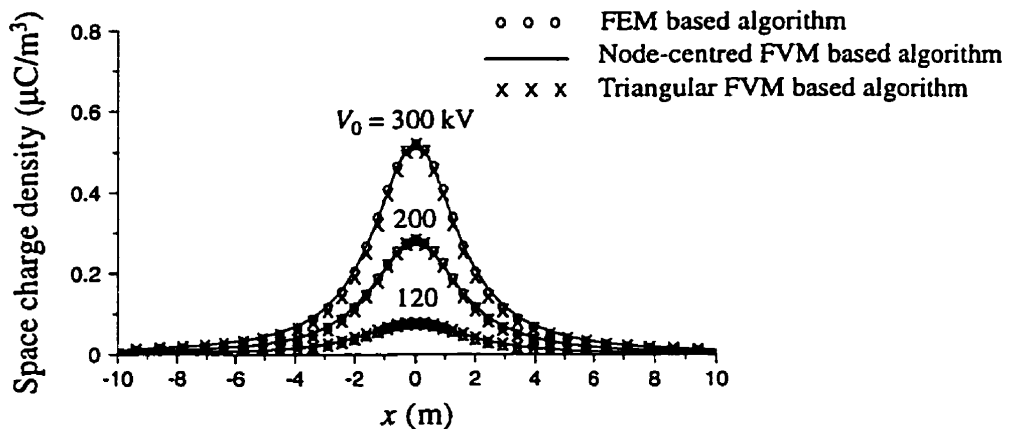


Figure 4.20. Comparison of the ground profiles of space charge density obtained by different algorithms in the absence of wind; $r_0 = 0.0025 \text{ m}$, $H = 2 \text{ m}$.

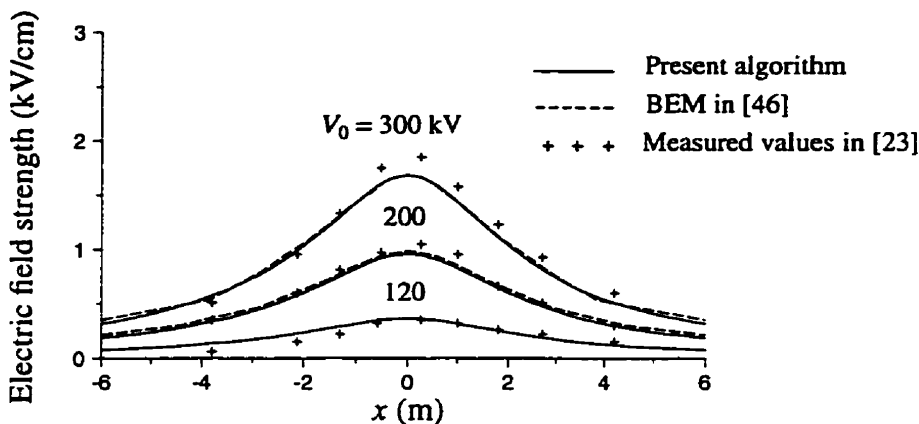


Figure 4.21. Comparison of the ground profiles of electric field strength obtained by the present algorithm with results in [46] and measured values in [23] ($w < 1 \text{ m/s}$); $r_0 = 0.0025 \text{ m}$, $H = 2 \text{ m}$.

4.6.4 Ground Profiles of the Field Quantities in the Presence of Wind

Figures 4.22 and 4.23 compare the ground level profiles of electric field strength and space charge density generated by the node-centered FVM based algorithm and the FEM based algorithm. From Figs. 4.22 and 4.23, it is seen that significant errors in ρ and u obtained by using the FEM based algorithm occur on the upwind side of the line where the space charge is almost cleared by wind. At other locations, however, the results generated by the two algorithms show good agreement. The errors affect the accuracy in calculating the corona losses, but do not affect the evaluation of the environmental effects of the ionized field at ground level.

Figures 4.24 and 4.25 show the ground profiles of the field quantities generated by the FVM based algorithm under strong wind conditions. It is observed the ground profiles of the field quantities are significantly distorted by wind and shifted in the direction of wind. The peak value of the profile increases with increase in the wind velocity, but it is not significant even with extremely strong wind. Also, the results obtained at a wind velocity of

30 m/s by using the two FVMs are compared in Figs. 4.24 and 4.25. Good agreement is observed. It should be mentioned that for this group of results, no published data are available for comparison.

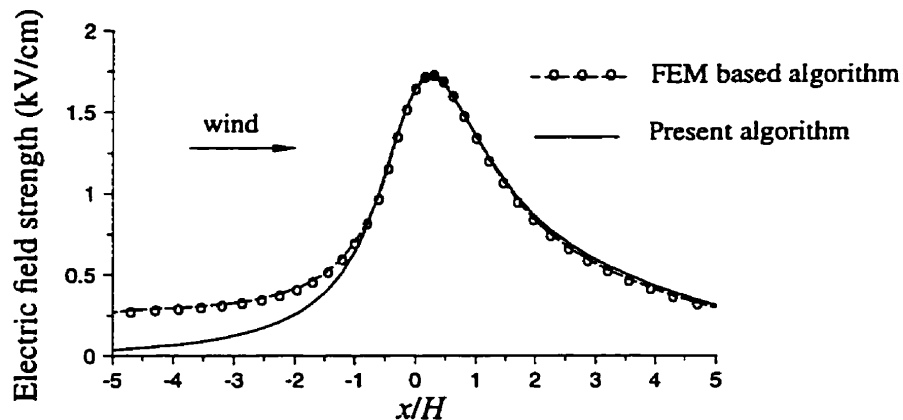


Figure 4.22. Comparison of the ground profiles of electric field strength obtained by different algorithms for a wind velocity $w = 8$ m/s; $r_0 = 0.0025$ m, $H = 2$ m, $V_0 = 300$ kV.

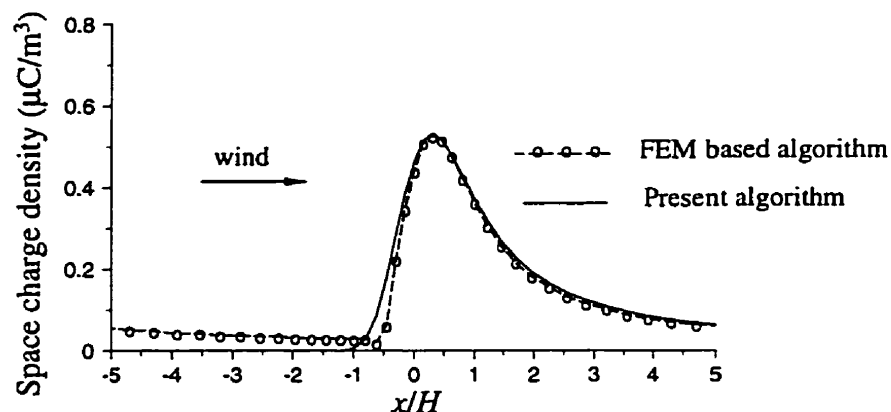


Figure 4.23. Comparison of the ground profiles of space charge density obtained by different algorithms for a wind velocity $w = 8$ m/s; $r_0 = 0.0025$ m, $H = 2$ m, $V_0 = 300$ kV.

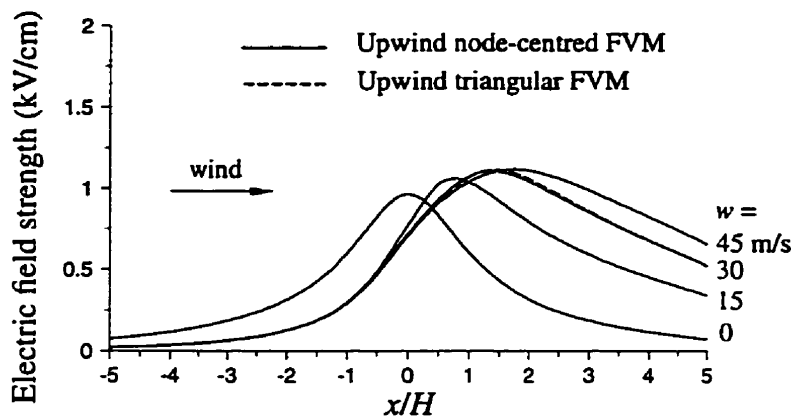


Figure 4.24. Ground profiles of electric field strength generated by the FVM based relaxation algorithm under strong wind conditions; $r_0 = 0.0025$ m, $H = 2$ m, $V_0 = 200$ kV.

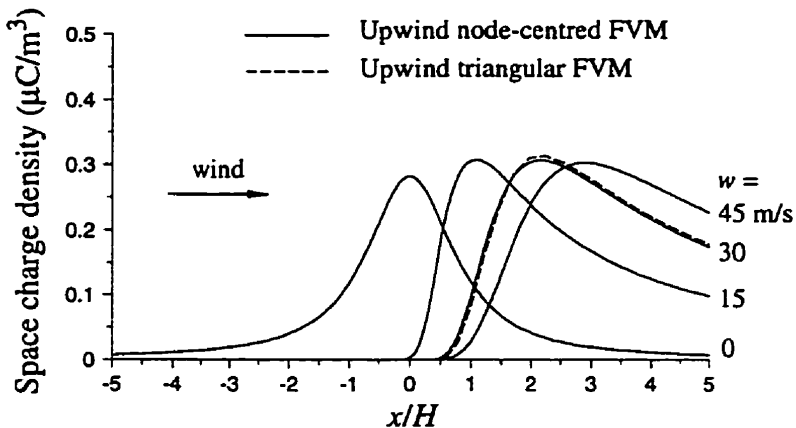


Figure 4.25. Ground profiles of space charge density generated by the FVM based relaxation algorithm under strong wind conditions; $r_0 = 0.0025$ m, $H = 2$ m, $V_0 = 200$ kV.

§4.7 Summary

A highly stable iterative algorithm has been proposed for the numerical solution of the ionized field of HVDC transmission lines. The framework for the construction of the iterative algorithm is constituted by alternative and repeated solution of the two governing equations for the potential and the space charge density, respectively. Introduction of a

relaxation technique into the iterative algorithm distinguishes it from other methods in the literature in the area of ionized field analyses and makes it possible to extend the validity of the iterative algorithm to cover a wide range of wind velocities, geometric parameters and ratios of the applied voltage to the corona onset value. To implement the iterative algorithm, the FEM is used to solve Poisson's equation for the electric potential, and two new FVMs are proposed to solve the current continuity equation for the space charge density. The presented iterative algorithm allows to take either the electric field strength or the space charge density at the conductor surface as a boundary condition. Besides, the ionic mobility is not necessarily required to be a constant over the solution domain.

Application of the triangular FVM allows to solve the resulting system of equations by using a simple method which needs negligible computational work. As a result, the computational effort for the corresponding iterative algorithm is about one-third of that when the node-centred FVM is used.

From numerical tests, the following conclusions may be drawn.

(1) The geometric parameters, i.e. the ratio H/r_0 and the conductor height H , have almost no effect on the iterative behaviour for a fixed voltage ratio V_0/V_c . This implies that the numerical results presented in this chapter are quite general in a practical sense.

(2) In strong wind conditions, the upwind scheme is necessarily required. Even in the case of light wind, the upwind algorithm performs better than in the case when $\gamma_{upw} = 0$. The iterative behaviour is almost unaffected by γ_{upw} , as long as it is larger than a small number (e.g. >0.1). In addition, γ_{upw} has a negligible effect on the calculated ground profiles of the field quantities.

(3) The upwind scheme yields excellent results in the presence of strong wind. In fact, the stronger the wind, the faster and more stable the associated iterative process. Such an interesting feature has not been observed in either the FEM based optimization algorithm presented in Chapters 2 and 3 or any other existing methods.

(4) Introduction of the relaxation technique into the iterative algorithm is crucial to ensure its stability and fast convergence in all situations. As for the choice of the relaxation factor θ , it is recommended that θ be chosen in the range $0.2 < \theta \leq 0.5$ for light wind, and $0.5 < \theta \leq 0.1$ for strong wind. For a very high ratio V_0/V_c (e.g. > 4) with light wind, θ should be between 0.2 and 0.4.

(5) The ground profiles of the field quantities, in the case of still air, obtained by the presented FVMs agree well with those obtained by other numerical methods [46,54,55] and also show satisfactory agreement with the available measured values [23].

(6) The ground profiles calculated using the two presented FVMs compare favourably for a wind velocity up to 45 m/s. It should be mentioned that the iterative algorithms presented remain stable at higher wind velocities.

(7) The FVM based algorithm generates practically the same ground profiles of the field quantities in the absence of wind as the FEM based optimization algorithm, but needs much less computational work.

CHAPTER 5

ANALYSIS OF BIPOLAR IONIZED FIELDS

In this chapter, the triangular FVM based relaxation algorithm presented in Chapter 4 is extended to analyze the ionized field associated with a bipolar DC transmission line. The effect of ion recombination on the field quantities at ground level is studied and a simplified model suggested for the bipolar ionized field in the absence of wind.

§5.1 Equations and Boundary Conditions

From Section 1.3, the ionized field of a bipolar HVDC transmission line is described by

$$\nabla^2 u = -(\rho^+ + \rho^-) / \epsilon_0 \quad (5.1)$$

$$\nabla \cdot (\rho^+ v^+) = \Theta \rho^+ \rho^- \quad (5.2)$$

$$\nabla \cdot (\rho^- v^-) = -\Theta \rho^+ \rho^- \quad (5.3)$$

with

$$v^+ = -k^+ \nabla u + w \quad (5.4)$$

$$v^- = k^- \nabla u + w \quad (5.5)$$

$$\Theta = R_{ion} / e \quad (5.6)$$

where u is the electric potential, ρ the space charge density, w the wind velocity, v the drift velocity of space charge, k the ionic mobility, R_{ion} the recombination coefficient, and e the absolute value of an electron charge. Quantities with superscripts "+" and "-" are

associated with positive and negative polarities, respectively.

The boundary conditions are

$$u = \begin{cases} V_0, & (x, y) \in \Gamma_c^+ \\ -V_0, & (x, y) \in \Gamma_c^- \\ 0, & (x, y) \in \Gamma_g \\ \Phi(x, y), & (x, y) \in \Gamma_a \end{cases} \quad (5.7)$$

$$\partial u / \partial n = E_c^+, \quad (x, y) \in \Gamma_c^+ \quad (5.8)$$

$$\partial u / \partial n = E_c^-, \quad (x, y) \in \Gamma_c^- \quad (5.9)$$

$$\rho^+ = 0, \quad (x, y) \in \Gamma_{up}^+ \quad (5.10)$$

$$\rho^- = 0, \quad (x, y) \in \Gamma_{up}^- \quad (5.11)$$

where V_0 is the applied voltage, $\Phi(x, y)$ the potential of the corresponding charge free field, and E_c the corona onset field strength. The boundaries Γ_c , Γ_g and Γ_a represent the conductor surface, ground and artificial boundary, respectively. The boundary conditions (5.8) and (5.9) are based on Kaptzov's assumption. If we assume that the magnitudes of the corona onset field strengths for both polarities are the same, then $E_c^- = -E_c^+$. The boundary Γ_{up}^+ in Eq. (5.10) is a portion of the boundary $\Gamma_a \cup \Gamma_g$ which is defined such that $v_n^+ = (-k^+ \nabla u + w) \cdot n < 0$ on Γ_{up}^+ , where n is the outward normal on the boundary, while Γ_{up}^- in Eq. (5.11) is defined as a portion of $\Gamma_a \cup \Gamma_g$ where $v_n^- = (k^- \nabla u + w) \cdot n < 0$. Physically, Eqs. (5.10) and (5.11) mean that the space charge flowing into the solution domain through the boundary $\Gamma_a \cup \Gamma_g$ is neglected. It should be noted that the boundaries Γ_{up}^+ and Γ_{up}^- can only be determined in the iterative process from the wind velocity and the electric field.

§5.2 Iterative Algorithm

5.2.1 Preliminary Considerations

Following a similar idea as in Section 4.2, we consider the electric potential u to consist of three components Φ , φ^+ , and φ^- . The first component, Φ , is due to the applied voltage in the absence of wind, and satisfies the following boundary value problem:

$$\begin{cases} \nabla^2 \Phi = 0 \\ \Phi|_{\Gamma_1} = V_0 \\ \Phi|_{\Gamma_2} = -V_0 \\ \Phi|_{\Gamma_3} = 0 \end{cases} \quad (5.12)$$

Equation (5.12) can be solved either numerically or analytically in the case of the bipolar DC line. The other two components, φ^+ and φ^- , are due to the positive and negative space charges respectively which can be obtained by solving the boundary value problems:

$$\begin{cases} \nabla^2 \varphi^+ = -\rho^+/\epsilon_0, & \text{in } \Omega \\ \varphi^+|_{\Gamma} = 0 \end{cases} \quad (5.13)$$

and

$$\begin{cases} \nabla^2 \varphi^- = -\rho^-/\epsilon_0, & \text{in } \Omega \\ \varphi^-|_{\Gamma} = 0 \end{cases} \quad (5.14)$$

where Ω and Γ are the solution domain and its boundary, respectively. It is obvious that the electric potential and the space charge densities, which satisfy Poisson's equation (5.1) and the boundary condition (5.7), can be expressed as

$$u = \Phi + \alpha^+ \varphi^{+*} + \alpha^- \varphi^{-*} \quad (5.15)$$

$$\rho^+ = \alpha^+ \rho^{+*} \quad (5.16)$$

$$\rho^- = \alpha^- \rho^{-*} \quad (5.17)$$

where α^+ and α^- are arbitrary constants, ϕ^{+*} , a potential distribution due to ρ^{+*} , is obtained by the solution of Eq. (5.13), and ϕ^{-*} due to ρ^{-*} is obtained by solving Eq.(5.14). In order for u , ρ^+ and ρ^- to satisfy the boundary conditions (5.8) and (5.9) as well, the constants α^+ and α^- are determined by

$$E_c^+ = E_{\Phi c^+} + \alpha^+ E_{\phi^+ c^+} + \alpha^- E_{\phi^- c^+} \quad (5.18a)$$

$$E_c^- = E_{\Phi c^-} + \alpha^+ E_{\phi^+ c^-} + \alpha^- E_{\phi^- c^-} \quad (5.18b)$$

where “ c^+ ” and “ c^- ” indicate the electric field strengths on the positive and negative conductor surfaces respectively, while “ Φ ”, “ ϕ^+ ” and “ ϕ^- ” indicate the source of the field. The field quantities u , ρ^+ and ρ^- thus determined must also satisfy the current continuity equations and conditions (5.10) and (5.11) in order to be the solution for the ionized field. Modification in the space charge densities is therefore required, which is accomplished by solving the current continuity equations (5.2) and (5.3), respectively, based on the electric potential given by Eq. (5.15). The solution for the ionized field can be reached by iteration as summarized in the next section.

5.2.2 Relaxation Iterative Algorithm

Based on the above discussion, a general iterative algorithm for the solution of a bipolar ionized field is now given as follows:

Step (1): Solve the boundary value problem (5.12) to obtain the potential Φ ; calculate $E_{\Phi c^+}$ and $E_{\Phi c^-}$; set $k = 1$, $u^{(k)} = \Phi$, $\rho_c^{+(k)} = \rho_c^{(0)}$, and $\rho_c^{-(k)} = -\rho_c^{(0)}$, where $\rho_c^{+(k)}$ and $\rho_c^{-(k)}$ are the positive and negative charge densities at Γ_c^+ and

Γ_c^+ , respectively; $\rho_c^{(0)}$ is an initial guess for the positive charge density at the positive conductor surface.

Step (2): Let $\rho^{+(k)} = \rho_{c^+}^{+(k)}$ at Γ_c^+ , $\rho^{-(k)} = \rho_{c^-}^{-(k)}$ at Γ_c^- , $\rho^{+(k)} = 0$ at Γ_{up}^+ and $\rho^{-(k)} = 0$ at Γ_{up}^- ; obtain $\rho^{+(k)}$ and $\rho^{-(k)}$ by solving the current continuity equations (5.2) and (5.3), respectively, based on the given distribution $u^{(k)}$.

Step (3): Solve the boundary value problems (5.13) and (5.14) for $\varphi^{+(k)}$ and $\varphi^{-(k)}$, respectively, based on the obtained $\rho^{+(k)}$ and $\rho^{-(k)}$; calculate $E_{\varphi^{+c^+}}^{(k)}$, $E_{\varphi^{+c^-}}^{(k)}$, $E_{\varphi^{-c^+}}^{(k)}$, and $E_{\varphi^{-c^-}}^{(k)}$.

Step (4): Calculate α_k^+ and α_k^- by solving the system of equations

$$E_c^+ = E_{\Phi c^+} + \alpha_k^+ E_{\varphi^{+c^+}}^{(k)} + \alpha_k^- E_{\varphi^{-c^+}}^{(k)} \quad (5.19a)$$

$$E_c^- = E_{\Phi c^-} + \alpha_k^+ E_{\varphi^{+c^-}}^{(k)} + \alpha_k^- E_{\varphi^{-c^-}}^{(k)}; \quad (5.19b)$$

if $|1 - \alpha_k^+| < \delta$ and $|1 - \alpha_k^-| < \delta$ where δ is a specified tolerance, terminate the iteration; otherwise proceed to step (5).

Step (5): Update the potential in the entire solution domain and the charge densities at Γ_c^+ and Γ_c^- , respectively, as:

$$u^{(k+1)} = \Phi + \alpha_k^+ \varphi^{+(k)} + \alpha_k^- \varphi^{-(k)} \quad (5.20)$$

$$\rho_{c^+}^{(k+1)} = \alpha_k^+ \rho_{c^+}^{(k)} \quad (5.21)$$

$$\rho_{c^-}^{(k+1)} = \alpha_k^- \rho_{c^-}^{(k)} \quad (5.22)$$

Step (6): Perform the relaxation procedure:

$$u^{(k+1)} = u^{(k)} + \theta (u^{(k+1)} - u^{(k)}) \quad (5.23)$$

$$\rho_{c^+}^{+(k+1)} = \rho_{c^+}^{+(k)} + \theta (\rho_{c^+}^{+(k+1)} - \rho_{c^+}^{+(k)}) \quad (5.24)$$

$$\rho_{c^-}^{-(k+1)} = \rho_{c^-}^{-(k)} + \theta (\rho_{c^-}^{-(k+1)} - \rho_{c^-}^{-(k)}) \quad (5.25)$$

Step (7): Set $k \leftarrow k + 1$ and repeat the iterative process from step (2).

In this algorithm, the parameters α_k^+ and α_k^- are used to update the involved quantities in the k th iteration, and also serve as a measure of convergence. The parameter θ is a relaxation factor, which is chosen in the range $0 < \theta < 1$. The solution of the boundary value problems in steps (1) and (3) is performed using the FEM as discussed in Chapters 2 and 4; the solution of the current continuity equations in step (2) is presented in the next section.

§5.3 Solution of the Current Continuity Equation

5.3.1 Discretization of the Current Continuity Equations

Integrating the current continuity equations over each triangular cell (see Section 4.4.2) leads to the following two systems of equations:

$$\int_{\partial C_i} \rho^+ v^+ \cdot \mathbf{n} ds = \Theta \Delta_i \rho_i^+ \rho_i^-, i = 1, 2, \dots, n_e \quad (5.26)$$

$$\int_{\partial C_i} \rho^- v^- \cdot \mathbf{n} ds = -\Theta \Delta_i \rho_i^+ \rho_i^-, i = 1, 2, \dots, n_e \quad (5.27)$$

where Δ_i is the area of the triangular cell C_i . The integrals along the boundary ∂C_i of C_i are evaluated by splitting them into portions, i.e.

$$\int_{\partial C_i} \rho^+ v^+ \cdot \mathbf{n} ds = \sum_{j \in I_{i0}^e} \int_{\partial C_{ij}} \rho^+ v^+ \cdot \mathbf{n} ds \quad (5.28)$$

$$\int_{\partial C_i} \rho^- v^- \cdot \mathbf{n} ds = \sum_{j \in I_{(i)}^c} \int_{\partial C_{ij}} \rho^- v^- \cdot \mathbf{n} ds \quad (5.29)$$

Considering the charge density to be a constant along each side of a cell, we have

$$\int_{\partial C_i} \rho^+ v^+ \cdot \mathbf{n} ds = \sum_{j \in I_{(i)}^c} \rho_{ij}^+ v_{ij}^+ \quad (5.30)$$

$$\int_{\partial C_i} \rho^- v^- \cdot \mathbf{n} ds = \sum_{j \in I_{(i)}^c} \rho_{ij}^- v_{ij}^- \quad (5.31)$$

where ρ_{ij}^+ and ρ_{ij}^- are the positive and negative charge densities on the side ∂C_{ij} , respectively, and

$$v_{ij}^+ = \int_{\partial C_{ij}} v^+ \cdot \mathbf{n} ds \quad (5.32)$$

$$v_{ij}^- = \int_{\partial C_{ij}} v^- \cdot \mathbf{n} ds \quad (5.33)$$

where v_{ij}^+ and v_{ij}^- are evaluated in the same manner as in Section 4.4.2. Substituting Eqs. (5.30) and (5.31) into (5.26) and (5.27), respectively, yields

$$\sum_{j \in I_{(i)}^c} \rho_{ij}^+ v_{ij}^+ - \Theta \Delta_i \rho_i^+ \rho_i^- = 0, \quad i = 1, 2, \dots, n_e \quad (5.34)$$

$$\sum_{j \in I_{(i)}^c} \rho_{ij}^- v_{ij}^- + \Theta \Delta_i \rho_i^+ \rho_i^- = 0, \quad i = 1, 2, \dots, n_e \quad (5.35)$$

On the side ∂C_{ij} , the positive and negative charge densities are taken to be

$$\rho_{ij}^+ = \frac{\rho_i^+ + \rho_j^+}{2} + \frac{\rho_i^+ - \rho_j^+}{2} \text{sign}(v_{ij}^+) \quad (5.36)$$

$$\rho_{ij}^- = \frac{\rho_i^- + \rho_j^-}{2} + \frac{\rho_i^- - \rho_j^-}{2} \text{sign}(v_{ij}^-) \quad (5.37)$$

Thus, Eqs.(5.34) and (5.35) become

$$A_{ii}^+ \rho_i^+ + \sum_{j \in I_{(i)}^C} A_{ij}^+ \rho_j^+ - \Theta \Delta_i \rho_i^+ \rho_i^- = 0, \quad i = 1, 2, \dots, n_e \quad (5.38)$$

$$A_{ii}^- \rho_i^- + \sum_{j \in I_{(i)}^C} A_{ij}^- \rho_j^- + \Theta \Delta_i \rho_i^+ \rho_i^- = 0, \quad i = 1, 2, \dots, n_e \quad (5.39)$$

where

$$A_{ij}^+ = \begin{cases} \sum_{s \in I_{(i)}^C} \frac{1}{2} [1 + sign(v_{is}^+)] v_{is}^+, & j = i \\ \frac{1}{2} [1 - sign(v_{ij}^+)] v_{ij}^+, & \text{for } j \in I_{(i)}^C \\ 0, & \text{otherwise} \end{cases} \quad (5.40)$$

$$A_{ij}^- = \begin{cases} \sum_{s \in I_{(i)}^C} \frac{1}{2} [1 + sign(v_{is}^-)] v_{is}^-, & j = i \\ \frac{1}{2} [1 - sign(v_{ij}^-)] v_{ij}^-, & \text{for } j \in I_{(i)}^C \\ 0, & \text{otherwise} \end{cases} \quad (5.41)$$

5.3.2 Solution of the Discretized Current Continuity Equations

After the space charge densities of the segment cells on Γ_c^+ , Γ_c^- , Γ_{up}^+ and Γ_{up}^- are specified as indicated in step (2) of Section 5.2.2, the discretized current continuity equations (5.38) and (5.39) can be easily solved using a scheme similar to that employed in Section 4.4.2.

Denote the subset of the associated cells on the upwind side of C_i for the positive space charge by $I_{(i)}^{Cupw+}$ and that for the negative space charge by $I_{(i)}^{Cupw-}$. If the positive space charge density of each cell in the set $I_{(i)}^{Cupw+}$ is known, the space charge density ρ_i^+ on C_i can be immediately obtained from the i th equation of the system of equations (5.38), i.e.

$$\rho_i^+ = \max \left\{ -\frac{1}{A_{ii}^+} \left[\sum_{j \in I_{(i)}^{cupw}} A_{ij}^+ \rho_j^+ - \Theta \Delta_i \tilde{\rho}_i^+ \tilde{\rho}_i^- \right], 0 \right\} \quad (5.42)$$

where $\tilde{\rho}_i^+$ and $\tilde{\rho}_i^-$ are the calculated values of the space charge densities of the cell C_i in the previous iteration. The space charge densities $\rho_1^+, \rho_2^+, \dots, \rho_{n_e}^+$ can be calculated starting from the triangular cells adjacent to the boundary $\Gamma_c^+ \cup \Gamma_{up}^+$ on which the space charge densities of the segment cells are specified. This process is summarized as follows:

(1) Generate the vector $\{n^{uw+}\}$ which is defined such that its element n_i^{uw+} represents the number of cells in the subset $I_{(i)}^{cupw+}$, and set $m = 0$.

(2) For $i = 1, 2, \dots, n_e$, if $n_i^{uw+} = 0$, calculate ρ_i^+ from Eq. (5.42) and then carry out

$$n_i^{uw+} \leftarrow n_i^{uw+} - 1$$

$$n_j^{uw+} \leftarrow n_j^{uw+} - 1, \text{ for all } j \in I_{(i)}^{cupw+}$$

$$m \leftarrow m + 1$$

(3) If $m = n_e$, stop; otherwise go to step (2).

Similarly, the solution scheme for the negative space charge density is given as follows:

(1) Generate the vector $\{n^{uw-}\}$ which is defined such that its element n_i^{uw-} represents the number of cells in the subset $I_{(i)}^{cupw-}$, and set $m = 0$.

(2) For $i = 1, 2, \dots, n_e$, if $n_i^{uw-} = 0$, carry out the following procedure:

$$\rho_i^- = \min \left\{ -\frac{1}{A_{ii}^-} \left[\sum_{j \in I_{(i)}^{cupw-}} A_{ij}^- \rho_j^- + \Theta \Delta_i \tilde{\rho}_i^+ \tilde{\rho}_i^- \right], 0 \right\}$$

$$n_i^{uw} \leftarrow n_i^{uw} - 1$$

$$n_j^{uw} \leftarrow n_j^{uw} - 1, \text{ for all } j \in I_{(i)}^{Cupw}$$

$$m \leftarrow m + 1$$

(3) If $m = n_e$, stop; otherwise go to step (2).

§5.4 Numerical Examples

5.4.1 Bipolar Test Model

The test model consists of two smooth cylindrical conductors of radius $r_0 = 0.0025$ m above ground with spacing $s = 3$ m and height $H = 2$ m, as shown in Fig. 5.1. The con-

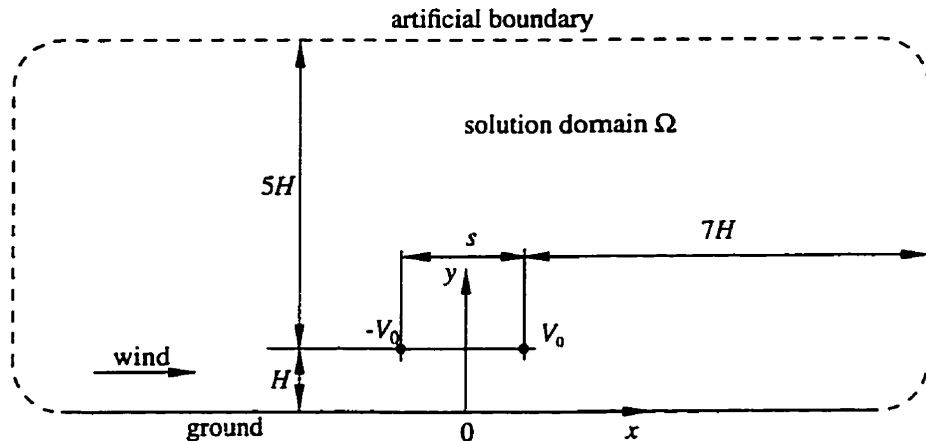


Figure 5.1. Bipolar DC line model.

ductor on the left is energized at a voltage $-V_0$ and the one on the right at a voltage V_0 , where $V_0 = 120, 200, 300$ kV. The wind is assumed to be uniform in a direction normal to the line parallel to the ground. The artificial boundary indicated by a dashed line (see Fig. 5.1) is located at a height $5H$ and lateral distance $7H$ from the line. The ionic mobilities of the positive and negative space charges are assumed to be equal [22], i.e.

$k^+ = k^- = 1.4 \times 10^{-4} \text{ m}^2/\text{V.s}$. Also, the corona onset field strengths of the two polarities are assumed to be the same in magnitude, i.e. $E_c^+ = -E_c^- = 48.06 \text{ kV/cm}$, which is obtained from Peek's law. The recombination coefficient is $R_{ion} = 2.2 \times 10^{-12} \text{ m}^3/\text{s}$.

The finite element mesh for this model is shown in Fig. 5.2, which is generated using the program in [45]. In the mesh, the number of nodes, $n_p = 2037$ and the number of elements, $n_e = 3934$.

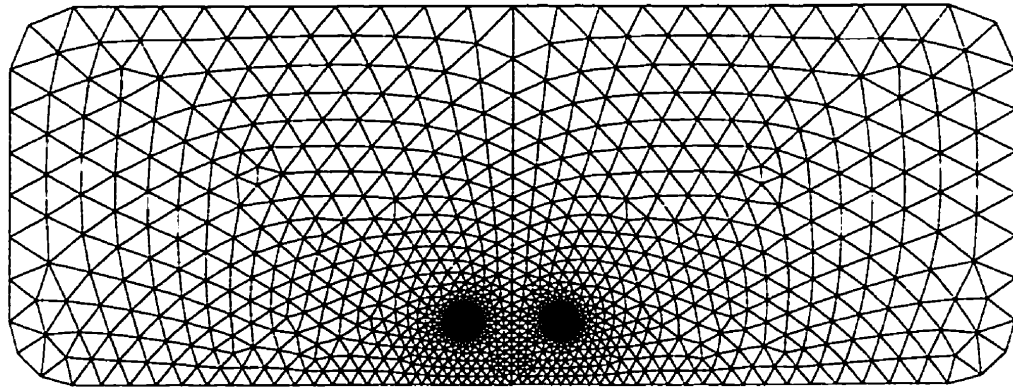


Figure 5.2. FE mesh for the bipolar DC line model.

5.4.2 *Ground Profiles of the Field Quantities*

The ground profiles of electric field strength and space charge density for three different voltage levels, obtained by using the proposed algorithm, are shown in Figs. 5.3 and 5.4, respectively. Also, the algorithm has been applied to show the effect of wind on the calculated ground profiles at an applied voltage of 200 kV.

In the implementation of the iterative algorithm, the relaxation factor was chosen in the range $0.05 < \theta < 0.2$ and convergence considered to be achieved when both $|1 - \alpha_k^+|$ and $|1 - \alpha_k^-|$ are less than 1%. The iterative process is stable and takes about 30 iterations to converge.

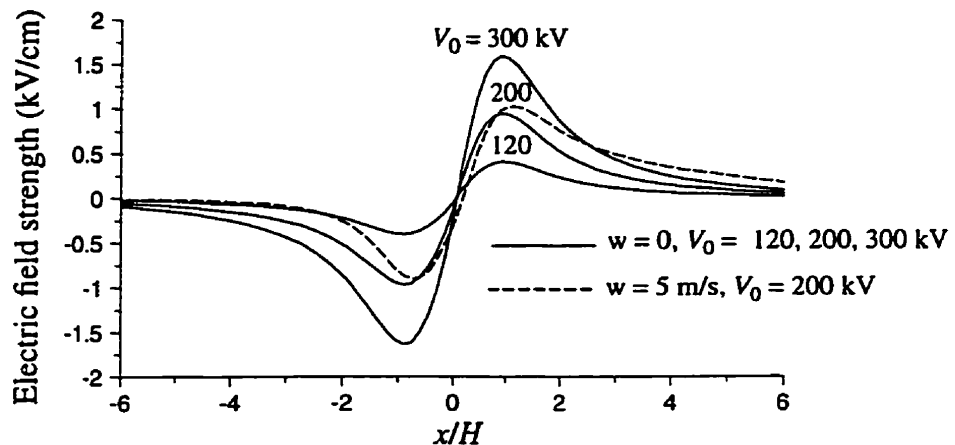


Figure 5.3. Calculated ground profiles of electric field strength.

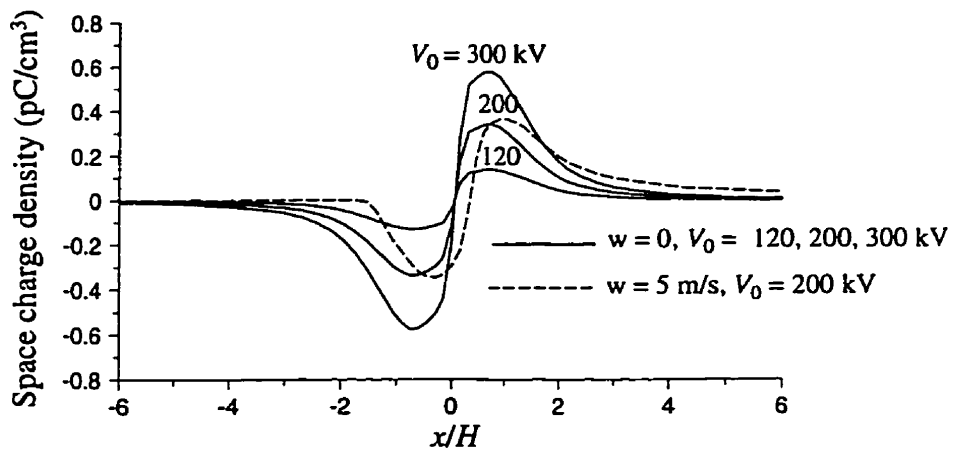


Figure 5.4. Calculated ground profiles of space charge density, ($\rho^+ + \rho^-$).

5.4.3 Effect of Recombination

Figures 5.5 and 5.6 show the calculated ground profiles of electric field strength and space charge density at a voltage level of 200 kV when the recombination coefficient is neglected. It is seen that the recombination coefficient has a negligible effect on the ground profiles of the field quantities. The same thing is true for other voltage levels.

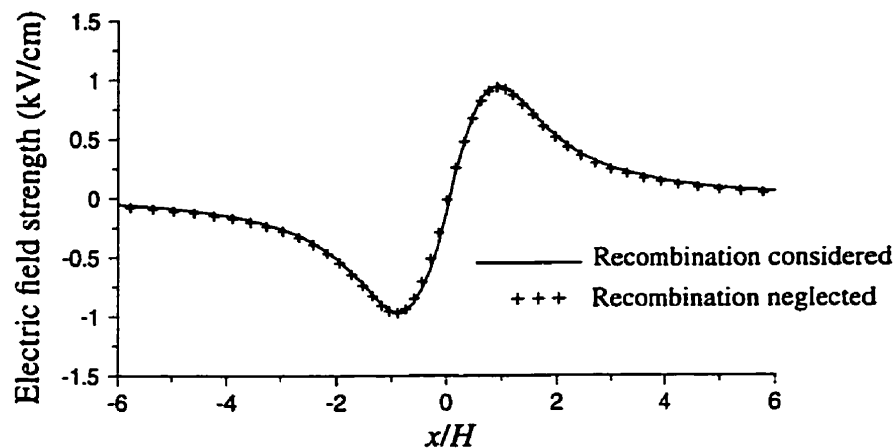


Figure 5.5. Effect of recombination on the ground profile of electric field strength; $V_0 = 200$ kV.

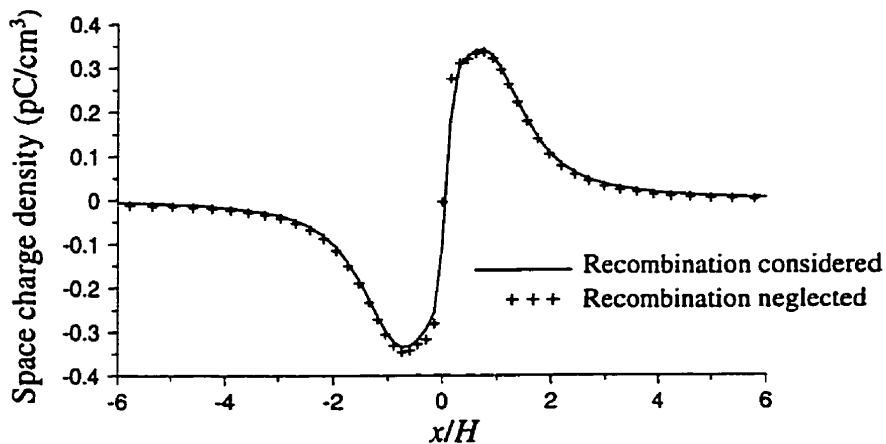


Figure 5.6. Effect of recombination on the ground profile of space charge density; $V_0 = 200$ kV.

§5.5 A Simplified Model for Bipolar Ionized Field

5.5.1 Calculation Model

In the absence of wind, the potential at all points on the symmetrically situated line $x = 0$ (see Fig. 5.1) is zero when the parameters for the two polarities, such as the corona onset field strength and the ionic mobility, are considered to be the same in magnitude, respectively. If we further assume that the positive space charge in the region $x < 0$ and the neg-

ative one in the region $x > 0$ are negligible, the bipolar ionized field region can be separated into two sub-regions in each of which only a unipolar ionized field exists. For instance, the positive unipolar ionized field is defined in the region $x > 0$ and is described by Eqs. (4.1)-(4.3) subject to the following boundary conditions:

$$u = \begin{cases} V_0, & (x, y) \in \Gamma_c \\ 0, & (x, y) \in \Gamma_g \\ 0, & x = 0 \\ \Phi(x, y), & (x, y) \in \Gamma_a \end{cases} \quad (5.43)$$

$$\partial u / \partial n = E_c, \quad (x, y) \in \Gamma_c \quad (5.44)$$

$$\rho = 0, \quad (x, y) \in \Gamma_{\rho} \quad (5.45)$$

where the superscript “+” has been dropped for simplicity. In the boundary condition (5.43), $\Phi(x, y)$ is the electric potential of the corresponding charge free field.

5.5.2 Numerical Results

The upwind FVM based relaxation algorithm for the unipolar ionized field in Chapter 4 is used to solve the above simplified bipolar ionized field model in the regions $x < 0$ and $x > 0$ for the negative and positive polarities, respectively. The calculated ground profiles of the field quantities at different voltage levels in the absence of wind are shown in Figs. 5.7 and 5.8. Comparison of these results with those obtained by use of the triangular FVM based algorithm for the bipolar ionized field described in Section 5.2.2 indicates that the above simplified model is acceptable, from an engineering point of view, for the evaluation of the ground profiles of the field quantities in the absence of wind. The simplified model results in significant reduction in the computational work since the solution over

half of the domain needs fewer nodes and each node has only two unknowns. In addition, a number of well developed techniques are available for solving the unipolar ionized field.

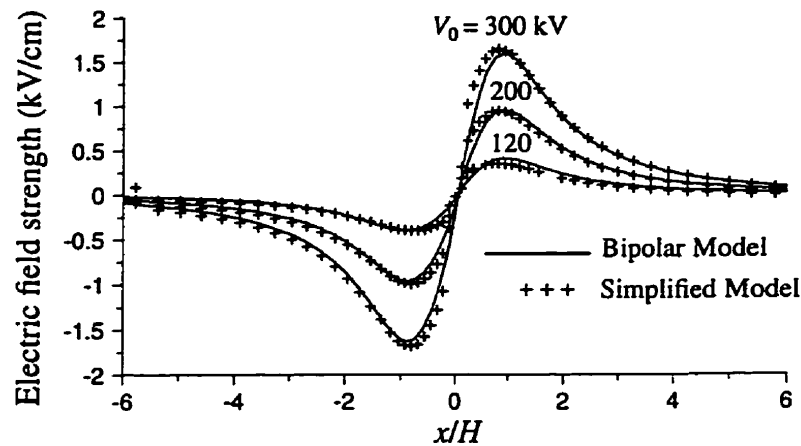


Figure 5.7. Ground profiles of electric field strength obtained by use of the simplified model at different voltage levels in the absence of wind.

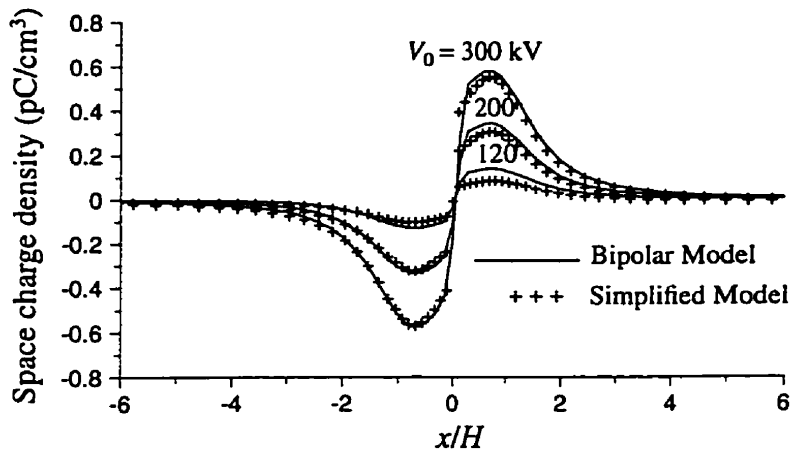


Figure 5.8. Ground profiles of space charge density, $(\rho^+ + \rho^-)$, obtained by use of the simplified model at different voltage levels in the absence of wind.

§5.6 Summary

A numerical algorithm has been presented for the solution of bipolar ionized fields based on the upwind triangular FVM and the relaxation technique in Chapter 4. Numerical tests on a bipolar line model show that the presented iterative algorithm is stable in the case of

still air and light wind. The relaxation factor in the case of the bipolar DC line model under consideration was chosen in the range $0.05 < \theta < 0.2$ and about 30 iterations are required for convergence.

Recombination of positive and negative space charges may be neglected for the evaluation of the ground profiles of the field quantities. Whether the recombination process is considered or not actually does not have an appreciable effect on the behaviour of the iterative process.

In the absence of wind, the bipolar ionized field may be modelled as the combination of two unipolar fields for computing the field quantities at ground level. Use of this simplified approach results in solutions with comparable accuracy with the computational work being substantially reduced.

It should be mentioned that the presented algorithm does not succeed in solving the bipolar ionized field as effected by strong wind (i.e. $w > 5$ m/s) due to a solution failure of the current continuity equation in the process of iteration.

CHAPTER 6

INVESTIGATION OF UNIPOLAR BUNDLED DC LINE IONIZED FIELDS

In this chapter, the upwind FVM based relaxation algorithm is applied to investigate the ionized field of unipolar bundled DC lines. The geometries considered are typical of practical DC lines and the effect of wind is included. The validity of the equivalent single conductor approach is verified. The convergence criterion used is $|1 - \alpha_k| < 1\%$.

§6.1 Introduction

Although a number of numerical algorithms which do not employ Deutsch's assumption have been proposed for the analysis of ionized fields associated with HVDC transmission lines since the 1960's, none of them have ever been applied to solve the ionized field of a bundled line without replacing its bundled conductor with an equivalent single cylindrical conductor. A review of the existing literature, however, indicates that there is a lack of information on the validity of employing an equivalent single conductor in the ionized field analysis of a bundled DC line. In the analyses carried out without resorting to the equivalent single conductor approach [26,29,35], the ratio of the conductor height to sub-conductor spacing considered is much smaller than practical values [29,35]. Besides, the numerical methods employed [26,29] are based on Deutsch's assumption, which is not valid in the presence of wind.

Therefore, it is of practical significance to study the ionized field of a bundled DC line and verify the validity of the equivalent single conductor approach.

§6.2 Effect of Conductor Bundling on Ionized Fields

In this section, a unipolar DC line with a 2-subconductor bundle is considered to examine the effect of the conductor bundling on the corona current and the behaviour of its associated ionized field at ground level in the absence of wind.

6.2.1 Line Model

The 2-bundle model has an average conductor height $H = 15.24$ m, as shown in Fig. 6.1.

Three subconductor radii are considered, $r_0 = 0.009525, 0.01905$ and 0.0381 m, with corresponding applied voltages of $V_0 = 314, 538$, and 926 kV, respectively. For each value

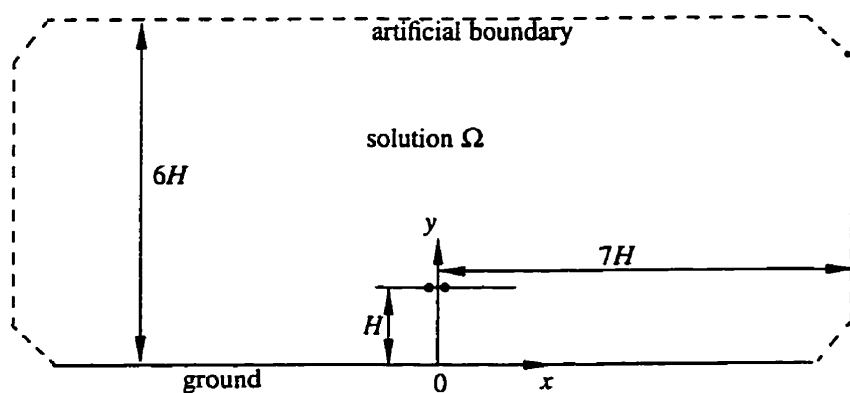


Figure 6.1. Two-bundle unipolar DC line.

of r_0 , the subconductor spacing s is varied such that $H/s = 0.5, 1, 2, 4, 8, 16$, and 32 .

These values cover the range of line parameters encountered in practice.

The surface factor of each subconductor is assumed to be $m = 0.4$. The corona onset field strength is evaluated by applying Peek's law to each subconductor, i.e.

$$E_c = 30m (1 + 0.301/\sqrt{r_0}) \text{ (kV/cm)} \quad (6.1)$$

Since the subconductor radius is much smaller than the subconductor spacing, the space charge density may be assumed to be uniformly distributed on each subconductor surface.

The finite element mesh for the 2-bundle model for the case when $r_0 = 0.01905$ m, $H = 15.24$ m and $H/s = 32$ is shown in Fig. 6.2; the local mesh near the bundled conductor is shown in Fig. 6.3

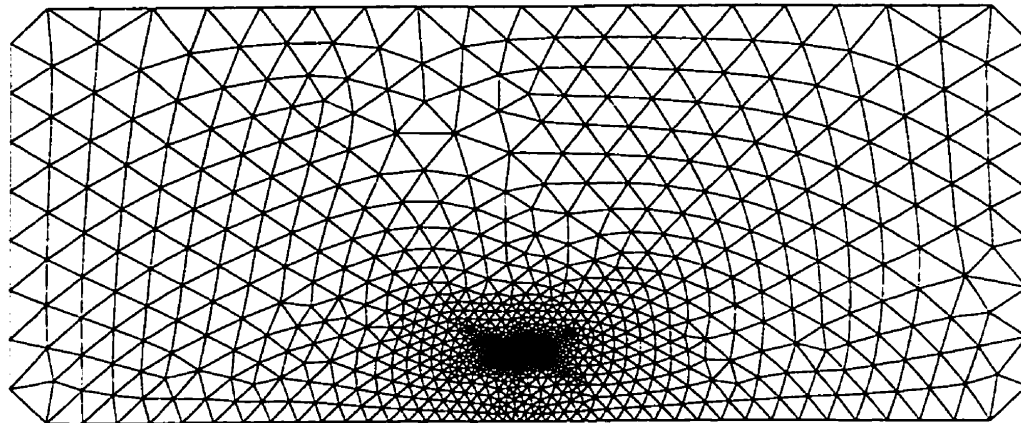


Figure 6.2. Finite element mesh for the 2-bundle model with $r_0 = 0.01905$ m, $H = 15.24$ m, $H/s = 32$, $n_p = 1769$ and $n_e = 3412$.

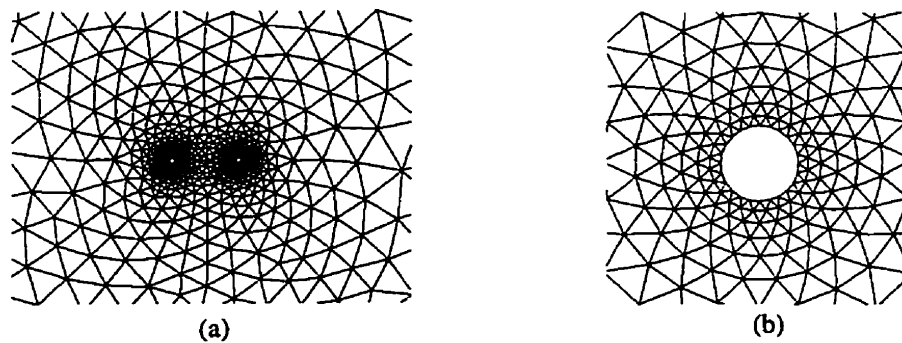


Figure 6.3. Local finite element mesh near the bundled conductor. (a) Local mesh near the 2-bundle. (b) Local mesh near each subconductor.

The node-centred upwind FVM based algorithm in Chapter 4 was employed, in which the electric field strengths E_{Φ_c} and $E_{\varphi_c}^{(k)}$ are taken to be their average values at the bundled conductor surface.

6.2.2 Numerical Results

The calculated ground profiles of electric field strength and space charge density for different sets of geometric parameters are shown in Figs. 6.4-6.9. The following facts emerge from examination of these figures. When the subconductor spacing is large (i.e. $H/s < 4$), two peaks occur in the ground profiles of electric field strength and space charge density, with the peaks located directly below the subconductors. As the subconductor spacing decreases, the locations of the peaks move closer to each other and the peak value of the space charge density decreases. However, the peak value of the electric field strength remains almost unchanged. When the subconductor spacing is such that $H/s \geq 4$, the peaks of the ground profile of field quantities merge and decrease as the subconductor spacing is further reduced.

For a practical bundled DC line, the ratio H/s is much larger than 4, and hence it is not possible to observe two peaks in the ground profile of field quantities.

Figure 6.10 shows the effect of subconductor spacing on the corona current. As expected, over a large range of s , the corona current decreases as the subconductor spacing is reduced. This confirms that in order to take advantage of bundling, the two subconductors should not be placed too far from each other.

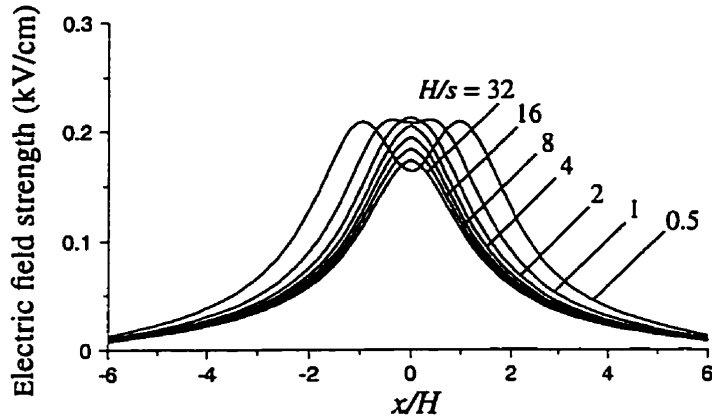


Figure 6.4. Ground profiles of electric field strength of the 2-bundle line for different H/s ; $H/r_0 = 1600$, $H = 15.24$ m, $V_0 = 314$ kV.

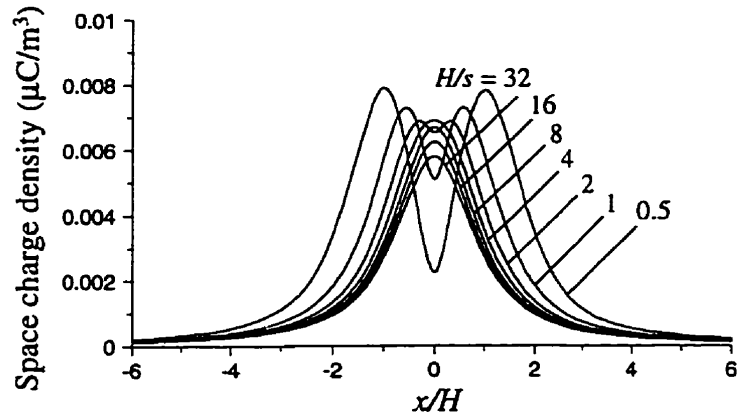


Figure 6.5. Ground profiles of space charge density of the 2-bundle line for different H/s ; $H/r_0 = 1600$, $H = 15.24$ m, $V_0 = 314$ kV.

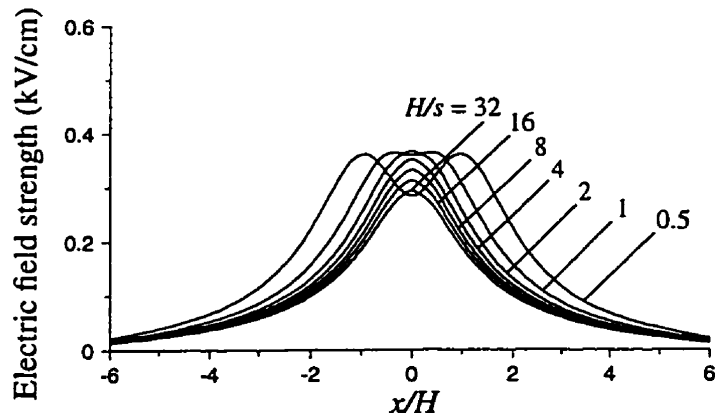


Figure 6.6. Ground profiles of electric field strength of the 2-bundle line for different H/s ; $H/r_0 = 800$, $H = 15.24$ m, $V_0 = 538$ kV.

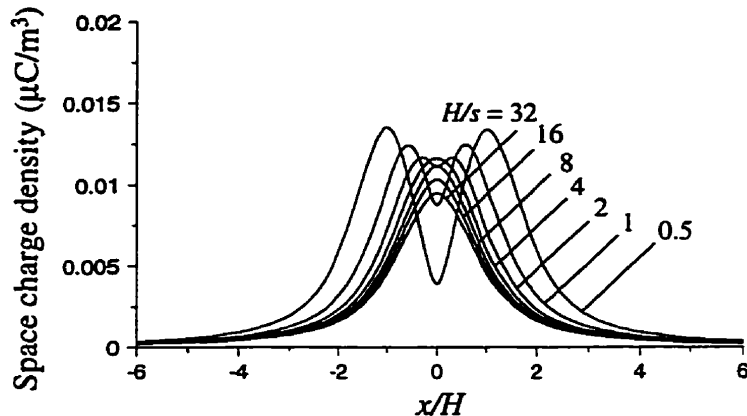


Figure 6.7. Ground profiles of space charge density of the 2-bundle line for different H/s ; $H/r_0 = 800$, $H = 15.24$ m, $V_0 = 538$ kV.

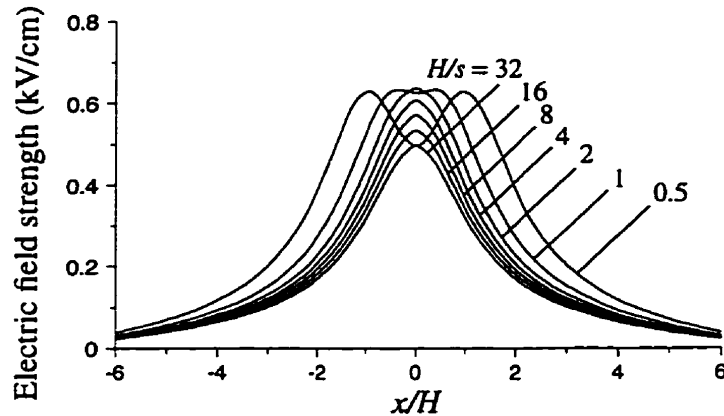


Figure 6.8. Ground profiles of electric field strength of the 2-bundle line for different H/s ; $H/r_0 = 400$, $H = 15.24$ m, $V_0 = 926$ kV.

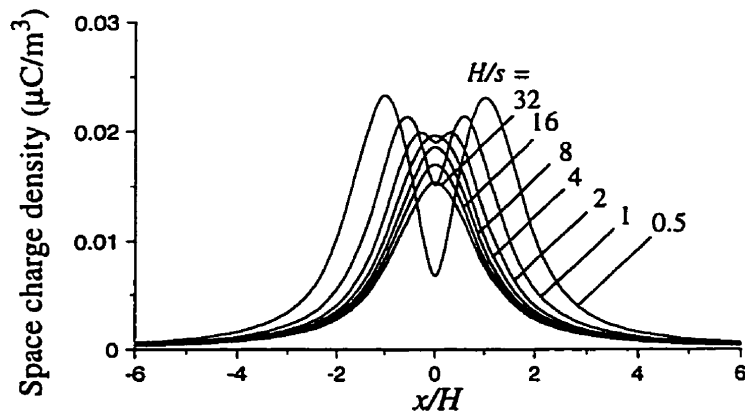


Figure 6.9. Ground profiles of space charge density of the 2-bundle line for different H/s ; $H/r_0 = 400$, $H = 15.24$ m, $V_0 = 926$ kV.

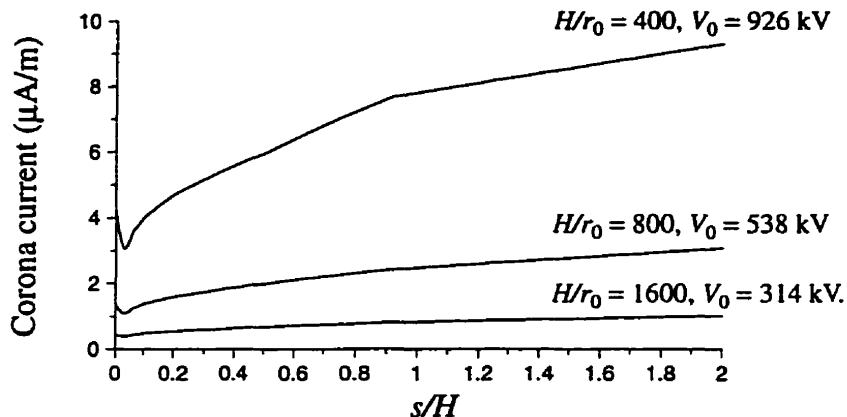


Figure 6.10. Effect of the ratio s/H on the corona current; $H = 15.24$ m.

§6.3 Comparison between 2- and 4-subconductor Bundle Unipolar Lines

A 600 kV line with 2- and 4-subconductor bundles is considered [7]. The corona current and the associated ground profiles of electric field strength and space charge density are compared in the presence of wind.

6.3.1 Line Models

In the 600 kV 2-bundle model (Fig. 6.1), the subconductor radius and spacing are taken to be $r_0 = 0.023$ m and $s = 0.457$ m, respectively. The total cross sectional area of the bundled conductor is 33.24 cm^2 . The corona onset field strength as calculated from Peek's law with a surface factor of 0.4 is $E_c = 14.38 \text{ kV/cm}$. In the corresponding finite element mesh, the number of nodes is $n_p = 1674$ and the number of elements is $n_e = 3222$.

In the 600 kV 4-bundle line (Fig. 6.11), the subconductor radius and spacing are $r_0 = 0.01525$ m and $s = 0.457$ m, respectively. The total area of section of the bundled conductor is 29.22 cm^2 . The average conductor height is the same as that in the 2-bundle

model, i.e. $H = 15.24$ m. From Peek's law, the corona onset field strength is $E_c = 14.92$ kV/cm for a surface factor of 0.4. The global finite element mesh for the 4-bundle line, which consists of 2429 nodes and 4688 elements, is similar to that for the 2-bundle line (see Fig. 6.2). The local mesh near the bundle is shown in Fig. 6.12. The local finite element mesh close to each subconductor is similar to that shown in Fig. 6.3(b).

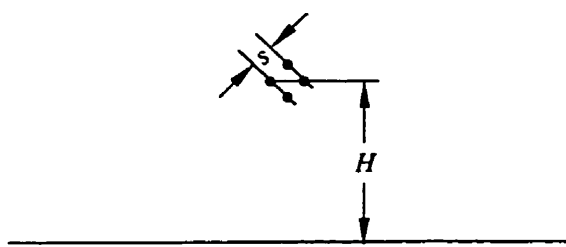


Figure 6.11. Four-subconductor bundled line.

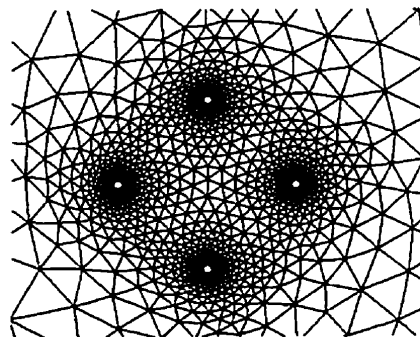


Figure 6.12. Local mesh near the bundled conductor.

6.3.2 Numerical Results

Figures 6.13 and 6.14 show the ground profiles of electric field strength and space charge density, respectively. It is seen that although the 4-bundle line uses less amount of material than the 2-bundle line, it is more efficient in reducing the magnitudes of electric field strength and space charge density at ground level both in the absence and in the presence of wind.

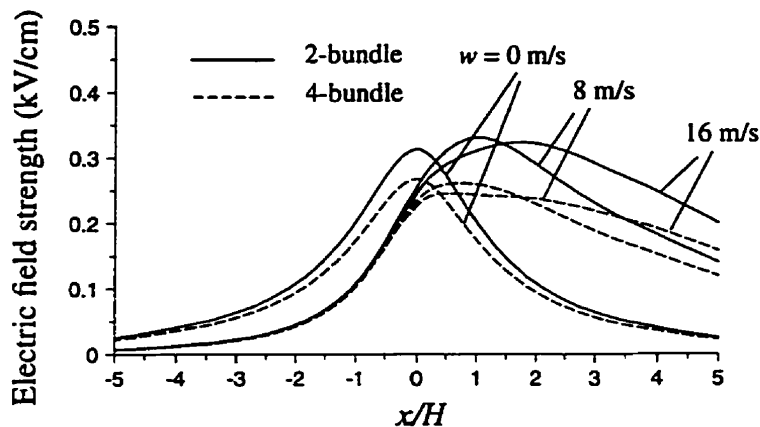


Figure 6.13. Ground profiles of electric field strength of the 2- and 4-bundle lines at different wind velocities.

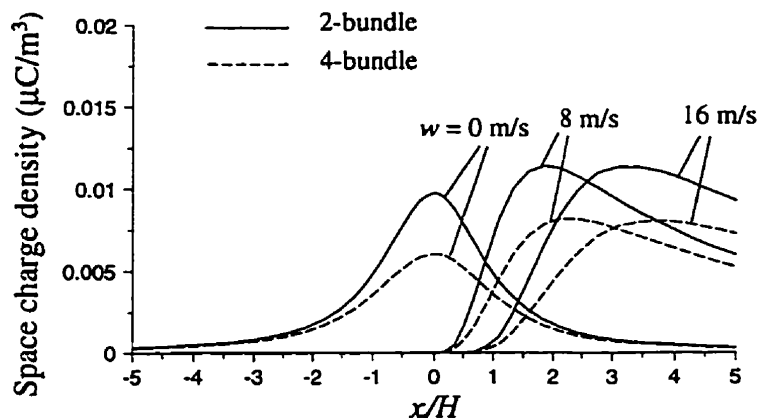


Figure 6.14. Ground profiles of space charge density of the 2- and 4-bundle lines at different wind velocities.

Since the ionized field in the case of the 4-bundle line is weaker, it is more easily influenced by wind. When the wind velocity attains a certain value, the crest of the ground profile of electric field strength flattens. With further increase in the wind velocity, two peaks appear (Fig. 6.13, 4-bundle case, $w = 16 \text{ m/s}$), one of which (on the left) is due to the applied voltage and the other is caused by the shifted space charge. As in the case of the 2-bundle line, the 4-bundle itself does not cause more than one peak in the ground profile of field quantities.

The corona currents of the bundled lines as influenced by wind is shown in Fig. 6.19. It is seen that the corona currents and hence the losses increase significantly with wind velocity. The corona loss due to the 4-bundle line is less than that due to the 2-bundle line by about 30~40% over the range of wind velocities considered.

The iterative algorithm performs well in the absence and in the presence of wind in terms of the stability and convergence rate. Only 10~20 iterations are needed for convergence when the tolerance δ (Section 4.2.2) is specified to be 1%.

§6.4 Equivalent Single Conductor Model

The ionized field of a unipolar DC line with a bundled conductor is conventionally modelled as the ionized field of a single cylindrical conductor DC line. In this section, the validity of this approach is verified.

6.4.1 *Equivalent Single Conductor*

In the absence of space charge, the bundled conductor can be replaced with an equivalent single cylindrical conductor in terms of the electric field strength at the conductor surface. For the ionized field, in addition to this condition, it is also required that the single conductor should have the same corona onset field strength as the bundled conductor. This requirement can actually be met by changing the surface factor m in Eq. (6.1).

The average electric field strength at the conductor surface of the twin subconductor bundle in Section 6.3, obtained by using the FEM, is 23.23 kV/cm, and that of the 4-subconductor bundle is 20.1 kV/cm. From these data and the above conditions, the equivalent single conductor which replaces the twin subconductor bundle should have a radius of

0.03873 m and a surface factor of 0.416. For the 4-subconductor bundle, the equivalent single conductor should have a radius of 0.04593 m and a surface factor of 0.436.

The ionized field was solved by employing a finite element mesh with 1219 nodes and 2332 elements for the former equivalent single conductor line. The performance of the latter equivalent single conductor line was evaluated by using 1195 nodes and 2284 elements.

6.4.2 Numerical Results

Figures 6.15 and 6.16 compare the ground profiles of electric field strength and space charge density of the 2-subconductor bundle line with those of its equivalent single conductor line for different wind velocities. Very good agreement is observed. The results for the 4-subconductor bundle line and its equivalent single conductor model are shown in Figs. 6.17 and 6.18. The application of the equivalent single conductor approach also yields satisfactory ground profiles of electric field strength and space charge density.

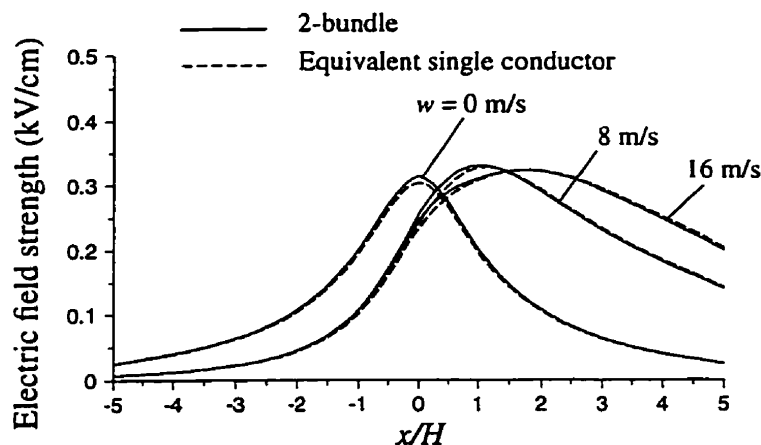


Figure 6.15. Ground profiles of electric field strength of the single conductor line equivalent to the 2-bundle line.

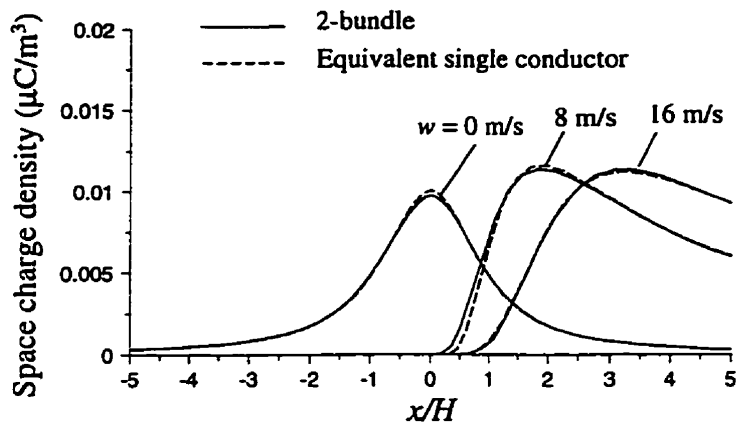


Figure 6.16. Ground profiles of space charge density of the single conductor line equivalent to the 2-bundle line.

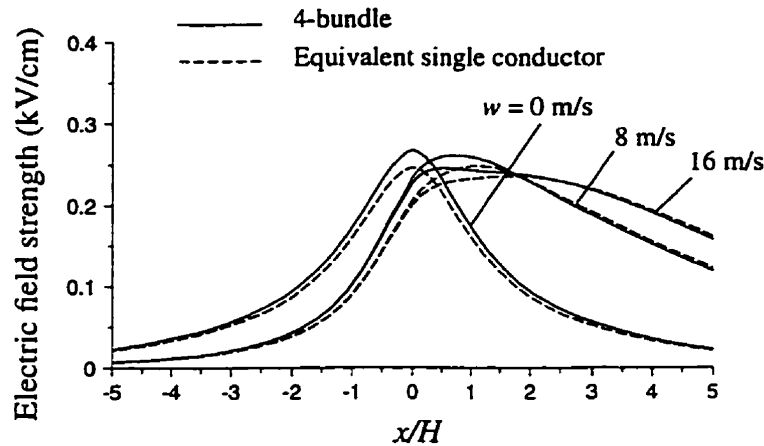


Figure 6.17. Ground profiles of electric field strength of the single conductor line equivalent to the 4-bundle line.

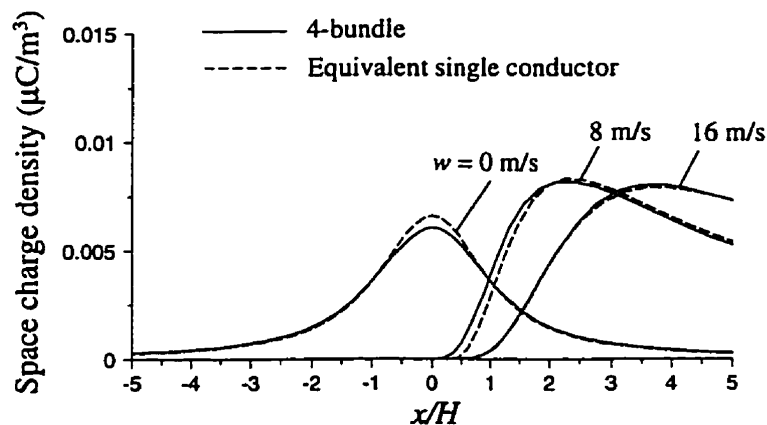


Figure 6.18. Ground profiles of space charge density of the single conductor line equivalent to the 4-bundle line.

Figure 6.19 shows the dependence of corona currents of the bundled lines on wind velocity as obtained by using their equivalent single conductor approach. It may be seen that the differences caused by the use of the equivalent single conductor is about 1% or less, which is negligibly small.

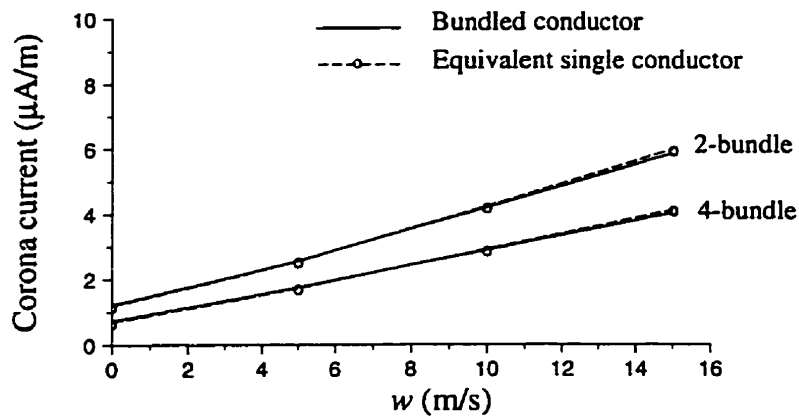


Figure 6.19. Corona currents of the equivalent single conductor lines as influenced by wind.

§6.5 Summary

As in the case of single conductor lines, the upwind node-centred FVM based relaxation algorithm may be used to efficiently obtain the solution of the ionized field associated with bundled unipolar DC lines. The iterative behaviour exhibited in the case of bundled lines is similar to that in Chapter 4. The same remark is true for the upwind triangular FVM based algorithm.

The subconductors of a bundled unipolar DC line with practical subconductor spacing do not give rise to twin peaks in the ground profiles of field quantities. A secondary peak can be obtained only in the profile of electric field strength under extremely strong wind conditions due to the effect of the shifted space charge.

A bundled conductor may be analysed by replacement of the subconductors with an

equivalent single cylindrical conductor provided the average electric field strength at the conductor surface and the corona onset field strength remain unchanged. Such an analysis yields satisfactory ground profiles of electric field strength and space charge density and practically the same corona current within the range of wind velocities encountered in practice.

CHAPTER 7

CONCLUSIONS

In this thesis, two new iterative algorithms, the FEM based optimization algorithm and the upwind FVM based relaxation algorithm, have been presented for solving the ionized field of unipolar HVDC transmission lines in the presence of wind. Numerical tests are carried out on a coaxial cylindrical geometry whose ionized field can be analytically solved as well as on a unipolar DC line model for which measured values of the field at ground level are available in the literature.

The FEM based optimization algorithm is shown to be highly efficient in terms of its stability, convergence rate and accuracy in the presence of moderate wind. Besides, it offers a theoretical advantage over existing methods by introducing a new solution methodology, i.e. to solve the ionized field problem by transforming it into an optimization problem for which the mathematical basis has been well established.

The upwind FVM based relaxation algorithm is constructed by resorting to a popular solution philosophy, i.e. to solve alternatively the two governing equations. However, the introduction of a relaxation technique into the iterative algorithm and the use of two new upwind FVMs distinguish it from other methods in the literature and make it possible to extend its applicability to cover a wide range of wind velocities, geometric parameters, and ratios of the applied voltage to the corona onset value.

The presented algorithms are compared, in terms of their performance, in Table 7.1. It is seen that the upwind node-centered FVM based relaxation algorithm performs better than the FEM based optimization algorithm in a general sense, and the upwind triangular FVM based algorithm is the most efficient from a computational point of view.

Table 7.1. Comparison of the presented algorithms.

Algorithm	FEM Based	Upwind Node-centered FVM Based	Upwind Triangular FVM Based
Number of Multiplications needed in Each Iteration	$O(16m_K^2n_p)$	$O(1.5m_K^2n_p)$	$O(0.5m_K^2n_p)$
Number of Iterations needed for Convergence	<10	10–20	10–20
Wind Velocity Limit	Moderate wind (e.g. $w \leq 8$ m/s)	No limit	No limit
Stability for Single Conductor Line in Light Wind	Excellent	Excellent	Excellent
Stability for Single Conductor Line in Strong Wind	Less than ideal	Excellent	Excellent
Stability for Bundled Line	Less than ideal	Excellent	Excellent

The upwind triangular FVM based relaxation algorithm has also been extended to solve the bipolar ionized field. Numerical results show that its performance is satisfactory in the presence of light wind. By using this algorithm, the effect of ion recombination is shown to be negligible for evaluating the field quantities at ground level. Also, a simplified model is suggested, which makes it possible to obtain the ground level field quantities of the bipolar ionized field in the absence of wind by solving two unipolar ionized fields.

As an application of the upwind node-centered FVM based relaxation algorithm, the ionized field associated with practical unipolar bundled DC lines including the effect of

wind has been investigated in detail. It is found that the bundled conductors of practical DC lines do not give rise to more than one peak in the ground profiles of the field quantities. In addition, it is shown that the ionized field of bundled DC lines may be evaluated by replacing the bundled conductor with an equivalent single cylindrical conductor both in the absence and in the presence of wind.

The main contributions of the thesis are now summarized as follows:

(1) A new solution methodology has been proposed, i.e. to solve the ionized field problem by transforming it into an optimization problem.

(2) For the first time, a relaxation technique has been introduced into the iterative algorithm for solution of the ionized field.

(3) Two new upwind FVMs for solving the current continuity equation have been proposed.

(4) A significant breakthrough has been achieved in the solution of ionized fields as affected by strong wind as well as conductor bundling.

(5) A simplified model has been suggested for evaluating the ground level field quantities of the bipolar ionized field in the absence of wind.

(6) For the first time, a numerical investigation has been carried out of the ionized field associated with practical unipolar bundled DC lines in still air and in the presence of wind.

It may therefore be concluded that the ionized field problem associated with unipolar DC lines (including bundled lines) in the presence of both light and strong wind has been well solved in the thesis.

There is, however, some scope for further work in this area using the methods sug-

gested in this thesis. The FEM based optimization algorithm does not perform as satisfactorily as expected in the presence of strong wind or when the line is equipped with a bundled conductor. Also, efforts should be made to improve the presented upwind triangular FVM based algorithm for solving the bipolar ionized field in order to handle the problem as affected by strong wind.

REFERENCES

(In chronological order)

Books

- [1] L.B.Loeb, *Electrical Coronas — Their Basic Physical Mechanisms*, University of California Press, 1965.
- [2] J.Kowalik and M.R.Osborne, *Methods for Unconstrained Optimization Problem*, American Elsevier Publishing Company, Inc., 1968.
- [3] S.L.S.Jacoby, J.S.Kowalik and J.T.Pizzo, *Iterative Methods for Nonlinear Optimization Problems*, Prentice-Hall, Inc., 1972.
- [4] J.E.Dennis and R.B.Schnabel, *Numerical Methods for Unconstrained Optimization and Nonlinear Equations*, Apprentice-Hall, Inc., 1983.
- [5] O.C.Zienkiewicz and K.Morgan, *Finite Elements and Approximation*, John Wiley & Sons, Inc., 1983.
- [6] E.Kuffel and W.S.Zaengl, *High Voltage Engineering — Fundamentals*, Pergamon Press, 1984.
- [7] H.L.Hill, A.S.Capon, O.Ratz, P.E.Renner, W.D.Schmidt and V.L.Miles, *Transmission Line Reference Book — HVDC to ± 600 kV*, Electric Power Research Institute, 3412 Hillview Avenue, Palo Alto, CA 94304.

Papers

- [8] J.S.Townsend, 'The Potentials Required to Maintain Currents between Coaxial Cylinders', *Phil. Mag.*, Vol. 28, 1914, pp. 83-90.
- [9] W.Deutsch, 'Über Die Dichtverteilung Unipolarer Ionenströme', *Annalen der Physik*, Vol. 5, 1933, pp. 589-613.
- [10] V.I.Popkov, 'On the Theory of Unipolar DC Corona', Elektrichestvo, No.1, 1949, pp. 33-48, *Technical Translation 1093, National Research Council of Canada*.
- [11] J.H.Simpson, 'Theoretical and Experimental Studies of Corona Loss from D.C. Lines', *Corona Research Meeting*, Montreal, P.Q., Canada, March 17-18, 1966.

- [12] T.N.Giao and J.B.Jordan, 'Modes of Corona Discharges in Air', *IEEE Trans. PAS*, Vol. 87, 1968, pp. 1207-1215.
- [13] Q.Vuhuu and R.P.Comsa, 'Influence of Gap Length on Wire-Plane Corona', *IEEE Trans. PAS*, Vol. 88, 1969, pp. 1462-1475.
- [14] P.S.Maruvada and W.Janischewskyj, 'DC Corona on Smooth Conductors in Air — Steady-state Analysis of the Ionization Layer', *Proc. IEEE*, Vol. 116, 1969, pp. 161-165.
- [15] M.P.Sarma and W.Janischewskyj, 'Analysis of Corona Losses on DC Transmission Lines: I — Unipolar Lines', *IEEE Trans. PAS*, Vol. 88, 1969, pp. 718-731.
- [16] M.P.Sarma and W.Janischewskyj, 'Analysis of Corona Losses on DC Transmission Lines: II — Bipolar Lines', *IEEE Trans. PAS*, Vol. 88, 1969, pp. 1476-1491.
- [17] M.Khalifa and M.Abdel-Salam, 'Improved Method for Calculating DC Corona Losses', *IEEE Trans. PAS*, Vol. 93, 1974, pp. 720-726.
- [18] J.R.McDonald, W.B.Smith, H.W.Spencer III and L. E.Sparks, 'A Mathematical Model for Calculating Electrical Conditions in Wire-duct Electrostatic Precipitation Devices', *J. Appl. Phys.*, Vol. 48, 1977, pp. 2231-2243.
- [19] W.Janischewskyj and G.Gela, 'Finite Element Solution for Electric Fields of Corona-nating DC Transmission Lines', *IEEE Trans. PAS*, Vol. 98, 1979, pp. 1000-1012.
- [20] P.A.Lawless and L.E.Sparks, 'A Mathematical Model for Calculating Effects of Back Corona in Wire-duct Electrostatic Precipitators', *J. Appl. Phys.*, Vol. 51, 1980, pp. 242-256.
- [21] H.Parekh, Y.L.Chow and K.D.Srivastava, 'A Simple Method of Calculating Corona Loss on Unipolar DC Transmission Lines', *IEEE Trans. EI*, Vol. 51, 1980, pp. 455-460.
- [22] T.Takuma, T.Ikeda and T.Kawamoto, 'Calculations of Ion Flow Fields of HVDC Transmission Lines by the Finite Element Method', *IEEE Trans. PAS*, Vol. 100, 1981, pp. 4802-4810.
- [23] M.Hara, N.hayashi, K.Shiotsuki and M.Akazaki, 'Influence of Wind and Conductor Potential on Distributions of Electric Field and Ion Current Density at Ground Level in DC High Voltage Line to Plane Geometry', *IEEE Trans. PAS*, Vol. 101, 1982, pp. 803-814.

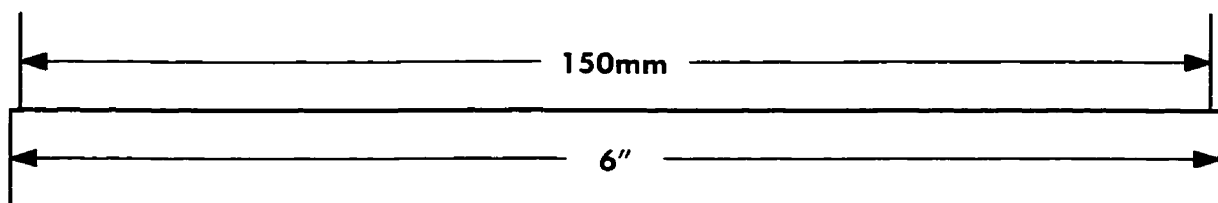
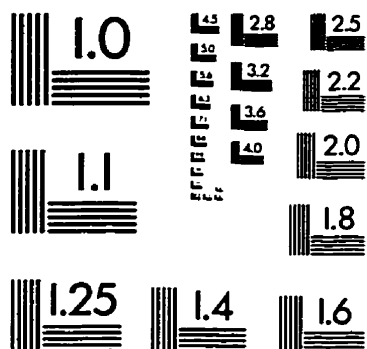
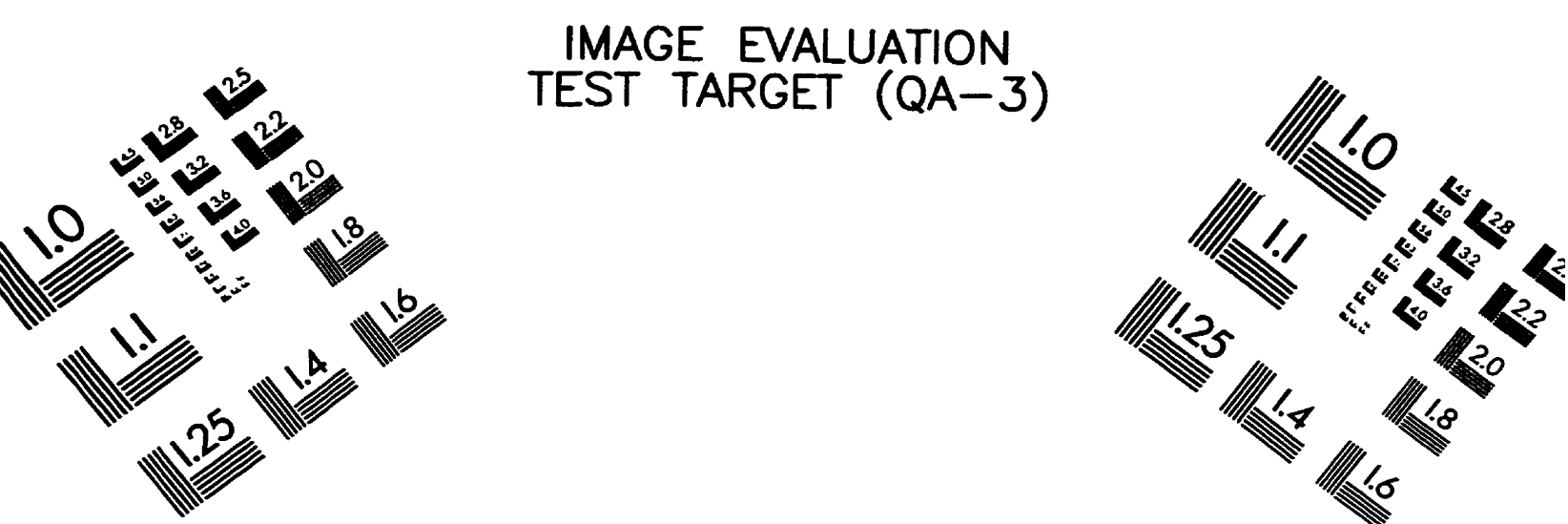
- [24] P.S.Maruvada, 'Corona-Generated Space Charge Environment in the Vicinity of HVDC Transmission Lines', *IEEE Trans. PAS*, Vol. 17, 1982, pp. 125-130.
- [25] I.R.Ciric and E.Kuffel, 'New Analytical Expressions for Calculating Unipolar DC Corona Losses', *IEEE Trans. PAS*, Vol. 101, 1982, pp. 2988-2994.
- [26] M.Abdel-Salam, M.Farghally and S.Abdel-Sattar, 'Monopolar Corona on Bundle Conductors', *IEEE Trans. PAS*, Vol. 101, 1982, pp. 4079-4089.
- [27] M.Abdel-Salam, M.Farghally and S.Abdel-Sattar, 'Finite Element Solution of Monopolar Corona Equation', *IEEE Trans. EI*, Vol. 19, 1983, pp. 110-119.
- [28] I.R.Ciric and E.Kuffel, 'On the Boundary Conditions for Unipolar DC Corona Field Calculation', *4th International Symposium on High Voltage Engineering*, Athens, Greece, Sept.5-9, 1983.
- [29] S.Abdel-Sattar, 'Numerical Method to Calculate Corona Profiles at Ground Level and Underneath Monopolar Lines as Influenced by Wind', *IEEE Trans. EI*, Vol. 21, 1986, pp. 205-211.
- [30] A.A.Elmoursi and G.S.P.Castle, 'Modelling of Corona Characteristics in a Wire-Duct Precipitator Using the Charge Simulation Technique', *IEEE Trans. IA*, Vol. 23, 1987, pp. 95-102.
- [31] T.Takuma and T.Kawamoto, 'A Very Stable Calculation Method for Ion Flow Field of HVDC Transmission Lines', *IEEE Trans. PWRD*, Vol. 2, 1987, pp. 189-198.
- [32] E.Kuffel, A.Dzierzynski and J.Poltz, *Final Report on: Development of Numerical Method for Analysis of Bipolar Corona on an HVdc System*, The University of Manitoba, January 28, 1987.
- [33] N.Fujioka, K.Arai, Y.Tsunoda *et al.*, 'Calculation of Electric Potential and Charge Density for Bipolar Ion-flow Field', *5th International Symposium on High Voltage Engineering*, Braunschweig, Germany, Aug.24-28, 1987.
- [34] I.R.Ciric and M.R.Raghubeer, 'Calculation of Coronating Conductor Surface Fields from Ground Level Experimental Data', *5th International Symposium on High Voltage Engineering*, Braunschweig, Germany, Aug.24-28, 1987.
- [35] S.Abdel-Sattar, 'Monopolar Corona on Bundle Wires as Influenced by Wind', *IEEE Trans. IA*, Vol. 23, 1987, pp. 984-989.
- [36] B.L.Qin, J.N.Sheng, Z.Yan and G.Gela, 'Accurate Calculation of Ion Flow Field

- under HVDC Bipolar Transmission Lines', *IEEE Trans. PWRD*, Vol. 3, 1988, pp. 368-376.
- [37] A.J.Butler, Z.J.Cendes and J.F.Hoburg, 'Interfacing the Finite-Element Method with the Method of Characteristics in Self-Consistent Electrostatic Field Models', *IEEE Trans. IA*, Vol. 25, 1989, pp. 533-538.
- [38] V.L.Chartier, R.D.Stearns and A.L.Burns, 'Electrical Environment of the Uprated Pacific NW/SW HVDC Intertie', *IEEE Trans. PWRD*, Vol. 4, 1989, pp. 1305-1317.
- [39] M.Abdel-Salam and S.Abdel-Sattar, 'Calculation of Corona V-I Characteristics of Monopolar Bundles Using the Charge Simulation Method', *IEEE Trans. EI*, Vol. 24, 1989, pp. 669-679.
- [40] J.Poltz and E.Kuffel, 'A New Method for the Two-Dimensional Bipolar Ion Flow Calculation', *6th International Symposium on High Voltage Engineering*, New Orleans, LA, USA, Aug.28-Sept.1, 1989.
- [41] Cui Xiang, Xie Xi, Fei Zengyao, Zhang Jintang and Yuan Jiansheng, 'Some Advances in High Voltage Electrostatic Field Computation and Their Applications', *6th International Symposium on High Voltage Engineering*, New Orleans, USA, Aug.28-Sept.1, 1989.
- [42] Y.Sunaga, Y.Amano and T.Suda, 'Method for Calculating Ion Flow Field around an HVDC Line in the Presence of Wind', *6th International Symposium on High Voltage Engineering*, New Orleans, LA, USA, Aug.28-Sept.1, 1989.
- [43] G.Ghione and R.D. Graglia, 'Two-Dimensional Finite-Boxes Analysis of Monopolar Corona Fields Including Ion Diffusion', *IEEE Trans. on Magnetics*, Vol. 26, 1990, pp. 567-570.
- [44] P.L.Levin and J.F.Hoburg, 'Donor Cell-Finite Element Descriptions of Wire-Duct Precipitator Fields, Charges, and Efficiencies', *IEEE Trans. IA*, Vol. 26, 1990, pp. 662-670.
- [45] Xin Li, 'An Automatic Triangular Mesh Generation Scheme for Arbitrary Planar Domains', *Trans. of Chinese Electrotechnical Society*, No.4, 1991, pp. 41-45.
- [46] Ming Yu, *The Study of Ionized Fields Associated with HVDC Transmission Lines in the Presence of Wind*, Ph.D Dissertation, Dept. of Electrical & Computer Engineering, University of Manitoba, 1993.

- [47] K.Adamak, 'Simulation of Corona in Wire-Duct Electrostatic Precipitator by Means of the Boundary Element Method', *IEEE Trans. IA*, Vol. 30, 1994, pp. 381-386.
- [48] K.Adamak, 'Adaptive Approach to Finite Element Modelling of Corona Fields', *IEEE Trans. IA*, Vol. 30, 1994, pp. 387-393.
- [49] M.Abdel-Salam and Z.Al-Hamouz, 'A Finite-ELEMENT Analysis of Bipolar Ionized Field', *IEEE Trans. IA*, Vol. 31, 1995, pp. 477-483.
- [50] M.Abdel-Salam and Z.Al-Hamouz, 'Analysis of Monopolar Ionized Field as Influenced by Ion Diffusion', *IEEE Trans. IA*, Vol. 31, 1995, pp. 484-493.
- [51] Xin Li, M.R.Raghubeer and I.M.R.Circic, 'A New Method for Solving Ionized Fields Associated with HVDC Transmission Lines', *Conference on Electrical Insulation and Dielectric Phenomena (CEIDP)*, Virginia Beach, Virginia, USA, Oct. 22-25, 1995.
- [52] V.Selman and L.Formaggia, 'Unified Construction of Finite Element and Finite Volume Discretizations for Compressible Flows', *Int. J. Numer. Methods eng.*, Vol. 39, 1996, pp. 33-50.
- [53] Xin Li, M.R.Raghubeer and I.R.Circic, 'On the Corona Voltage-Current Characteristic of Unipolar HVDC Transmission Lines', *Conference on Electrical Insulation and Dielectric Phenomena (CEIDP)*, Millbrae, California, USA, Oct. 20-23, 1996.
- [54] Xin Li, I.R.Circic and M.R.Raghubeer, 'A New Method for Solving Ionized Fields of Unipolar HVDC Lines Including Effect of Wind. Part I: FEM Formulation', *Int. J. Numer. Model., Electron. Netw. Devices Fields*, Vol. 10, 1997, pp. 47-56.
- [55] Xin Li, M.R.Raghubeer and I.R.Circic, 'A New Method for Solving Ionized Fields of Unipolar HVDC Lines Including Effect of Wind. Part II: Iterative Techniques and Numerical Tests', *Int. J. Numer. Model., Electron. Netw. Devices Fields*, Vol. 10, 1997, pp. 57-69.
- [56] Xin Li, M.R.Raghubeer and Circic, "Recent Advances in Numerical Solution of Ionized Fields Associated with Unipolar HVDC Transmission Lines in the Presence of Wind", *10th International Symposium on High Voltage Engineering*, Montreal, Quebec, Canada, Aug.25-29, 1997.
- [57] Xin Li ,M. R. Raghubeer and I. R. Circic 'Analysis of the Ionized Field Associated

- with a Bundled DC Line Including Effect of Wind', *Conference on Electrical Insulation and Dielectric Phenomena (CEIDP)*, Minneapolis, Minnesota, USA, Oct. 19-22, 1997.
- [58] Xin Li, I.R.Ciric and M.R.Raghubeer, 'Highly Stable Finite Element Volume Based Relaxation Iterative Algorithm for Solution of DC Line Ionized Fields in the Presence of Wind', Accepted for publication by *Int. J. Numer. Model., Electron. Netw. Devices Fields*.

IMAGE EVALUATION TEST TARGET (QA-3)



APPLIED IMAGE, Inc.
1653 East Main Street
Rochester, NY 14609 USA
Phone: 716/482-0300
Fax: 716/288-5989

© 1993, Applied Image, Inc., All Rights Reserved